

# We are IntechOpen, the world's leading publisher of Open Access books Built by scientists, for scientists

6,900

Open access books available

186,000

International authors and editors

200M

Downloads

Our authors are among the

154

Countries delivered to

TOP 1%

most cited scientists

12.2%

Contributors from top 500 universities



WEB OF SCIENCE™

Selection of our books indexed in the Book Citation Index  
in Web of Science™ Core Collection (BKCI)

Interested in publishing with us?  
Contact [book.department@intechopen.com](mailto:book.department@intechopen.com)

Numbers displayed above are based on latest data collected.  
For more information visit [www.intechopen.com](http://www.intechopen.com)



---

# High-Base Optical Signal Processing

---

Jian Wang and Alan E. Willner

Additional information is available at the end of the chapter

<http://dx.doi.org/10.5772/61504>

---

## Abstract

Optical signal processing is a promising technique to enable fast data information processing in the optical domain. Traditional optical signal processing functions pay more attention to binary modulation formats (i.e., binary numbers) with single-bit information contained in one symbol. The ever-growing data traffic has propelled great success in high-speed optical signal transmission by using advanced multilevel modulation formats (i.e., high-base numbers), which encode multiple-bit information in one symbol with resultant enhanced transmission capacity and efficient spectrum usage. A valuable challenge would be to perform various optical signal processing functions for multilevel modulation formats, i.e., high-base optical signal processing. In this chapter, we review recent research works on high-base optical signal processing for multilevel modulation formats by exploiting degenerate and nondegenerate four-wave mixing in highly nonlinear fibers or silicon photonic devices. Grooming high-base optical signal processing functions including high-base wavelength conversion, high-base data exchange, high-base optical computing, and high-base optical coding/decoding are demonstrated. High-base optical signal processing may facilitate advanced data management and superior network performance.

**Keywords:** High-base optical signal processing, multilevel modulation format, four-wave mixing, wavelength conversion, data exchange, optical computing, coding/decoding

---

## 1. Introduction

The arrival of the era of big data has fuelled the increasing demand on both high-speed signal transmission and fast signal processing, which are known as two themes of great importance for optical communications. The advances in fiber-optic technologies have resulted in great success in delivering high-speed data signals in optical fiber transmission links [1-5]. The rapid development of photonics technologies has also promoted increasing interest for optical signal processing, which is regarded as a promising solution to facilitate high-speed signal processing

in the optical domain and to eliminate complicated, inefficient, low-latency, and power-consuming optical-to-electrical-to-optical (O-E-O) conversions [6]. At network nodes of advanced photonic networks, different optical signal processing functions might be required to enable increased network flexibility and efficiency. Remarkably, nonlinear optics has offered great potential to develop optical signal processing in high-speed photonic networks using various optical nonlinearities [6-20]. Miscellaneous optical signal processing functions have been demonstrated, such as wavelength conversion, wavelength (de)multiplexing, wavelength multicasting, data exchange, add/drop, optical addressing, optical switching, optical logic gate, optical computing, optical format conversion, optical correlation, optical equalization, optical regeneration, tunable optical delay, optical coding/decoding, etc. [21-53]. These optical signal processing operations are enabled by exploiting different nonlinear effects in different nonlinear optical devices. The typical nonlinear effects include cross-gain modulation (XGM), self-phase modulation (SPM), cross-phase modulation (XPM), two-photon absorption (TPA), degenerate and nondegenerate four-wave mixing (FWM), second-harmonic generation (SHG), sum-frequency generation (SFG), difference-frequency generation (DFG), cascaded second-harmonic generation and difference-frequency generation (cSHG/DFG), and cascaded sum- and difference-frequency generation (cSFG/DFG). Typical nonlinear optical devices based on different platforms include semiconductor optical amplifiers (SOAs), highly nonlinear fibers (HNLFs), periodically poled lithium niobate (PPLN) waveguides, chalcogenide ( $\text{As}_2\text{S}_3$ ) waveguides, silicon waveguides, and photonic crystal waveguides. It is noted that most of previous research efforts are dedicated to optical signal processing for binary modulation formats such as on-off keying (OOK), differential phase-shift keying (DPSK), and binary phase-shift keying (BPSK). Despite favorable operation performance achieved for binary optical signal processing, it suffers limited bitrate and low spectral efficiency since only single-bit information is carried by each symbol for binary modulation formats.

With the rapid growth of global broadband and mobile data traffic, high transmission capacity and high spectral efficiency are highly desirable. Fortunately, recent advances in multilevel modulation formats, coherent detection, and digital signal processing have led to tremendous increase in transmission capacity and spectral efficiency [54-63]. Beyond great progress in high-speed signal transmission, processing multilevel modulation formats in the optical domain could be another interesting topic compatible with superior network performance and advanced data management. Typically, multilevel modulation formats contain multiple bits in one symbol, e.g., 2, 3, and 4 bits in one symbol for quadrature phase-shift keying (QPSK), 8-ary phase-shift keying (8PSK), star 8-ary quadrature amplitude modulation (Star-8QAM), 16-ary phase-shift keying (16PSK), star 16-ary quadrature amplitude modulation (Star-16QAM), and square 16-ary quadrature amplitude modulation (Square-16QAM) (Fig. 1). Moreover, multiple points in the constellation plane can be used to represent high-base numbers, e.g., quaternary number for QPSK, octal numbers for 8PSK and Star-8QAM, and hexadecimal numbers for 16PSK, Star-16QAM and Square-16QAM (Fig. 1). Despite great success in transmission links using multilevel modulation formats [64-69], there have been relatively limited research efforts dedicated to their manipulation in the optical domain (i.e., high-base optical signal processing). In this scenario, a laudable goal would be to develop miscellaneous high-base optical signal processing functions for multilevel modulation formats

(Square-16QAM) (Fig. 1). Moreover, multiple points in the constellation plane can be used to represent high-base numbers, e.g., quaternary number for QPSK, octal numbers for 8PSK and Star-8QAM, and hexadecimal numbers for 16PSK, Star-16QAM and Square-16QAM (Fig. 1). Despite great success in transmission links using multilevel modulation formats [64–69], there have been relatively limited research efforts dedicated to their manipulation in the [70–86]. The aforementioned optical nonlinearities in various nonlinear optical devices would be promising candidates to facilitate grooming high-base optical signal processing operations.

In this chapter, we provide a comprehensive report of our recent research works on data exchange using degenerate/nondegenerate FWM in HNLFs or silicon-organic hybrid slot waveguides [71, 73, 74, 86], optical computing using degenerate/nondegenerate FWM in HNLFs or silicon-organic hybrid slot waveguides [75, 77, 80, 85], and optical coding/decoding using degenerate FWM in HNLFs [79]. The demonstrated high-base optical signal processing functions include wavelength conversion using degenerate FWM in a silicon waveguide [85], data exchange using degenerate/nondegenerate FWM in HNLFs or silicon-organic hybrid slot waveguides [71, 73, 74, 86], optical computing using degenerate/nondegenerate FWM in HNLFs or silicon-organic hybrid slot waveguides [75, 77, 80, 85], and optical coding/decoding using degenerate FWM in HNLFs [79].

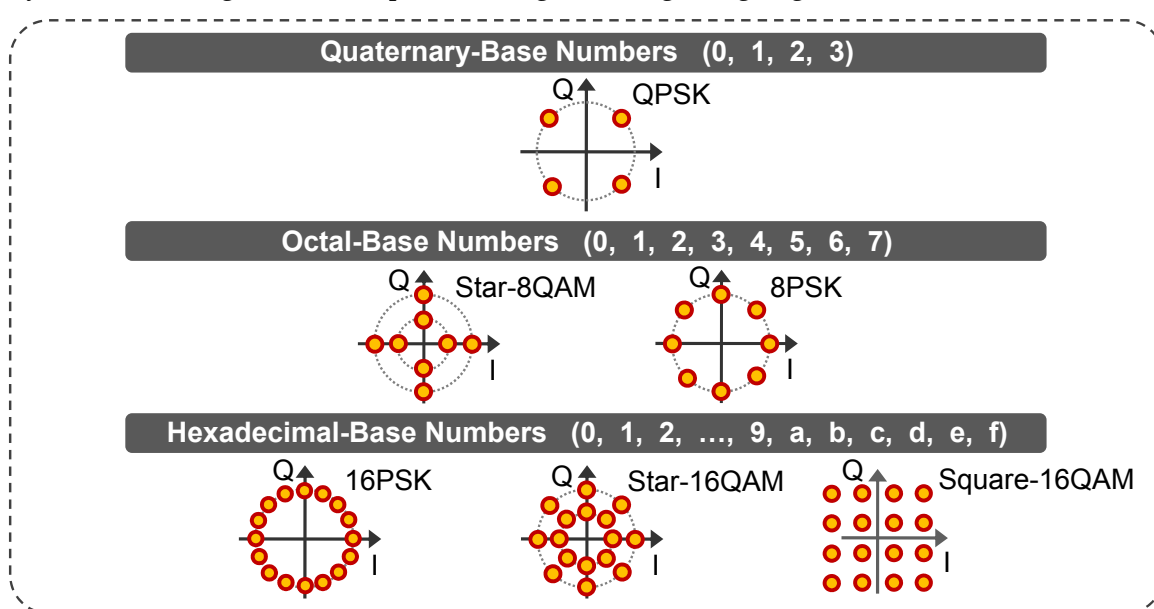


Fig. 1. Schematic constellations of advanced multilevel modulation formats representing high-base (quaternary, octal, hexadecimal) numbers (QPSK, Star-8QAM/8PSK, 16PSK/Star-16QAM/Square-16QAM).

## 2. High-Base Wavelength Conversion [83]

We demonstrate high-base all-optical wavelength conversions of multicarrier, multilevel modulation signals based on degenerate FWM in a silicon waveguide. Coherent multicarrier, multilevel modulations, i.e., orthogonal frequency-division multiplexing (OFDM) combined with advanced multilevel quadrature amplitude modulation (mQAM), are employed in the experiment.

Shown in Fig. 2(a) is the schematic cross section of a typical silicon waveguide. The calculated mode distribution using finite element method (FEM) is depicted in Fig. 2(b), from which one can see the tight light confinement in the top silicon region due to the high contrast index of the silicon waveguide. The measured scanning electron microscope (SEM) images of the

fabricated silicon waveguide and grating coupling region are shown in Fig. 2(c) and (d). We fabricate the silicon waveguide on a silicon-on-insulator (SOI) wafer, on the top of which the silicon thickness is 340 nm with a 2- $\mu\text{m}$ -thick buried oxide (BOX) layer. Using electron-beam lithography (EBL), followed by induced coupled plasma (ICP) etching, the desired silicon waveguide is formed for on-chip, high-base wavelength conversion.

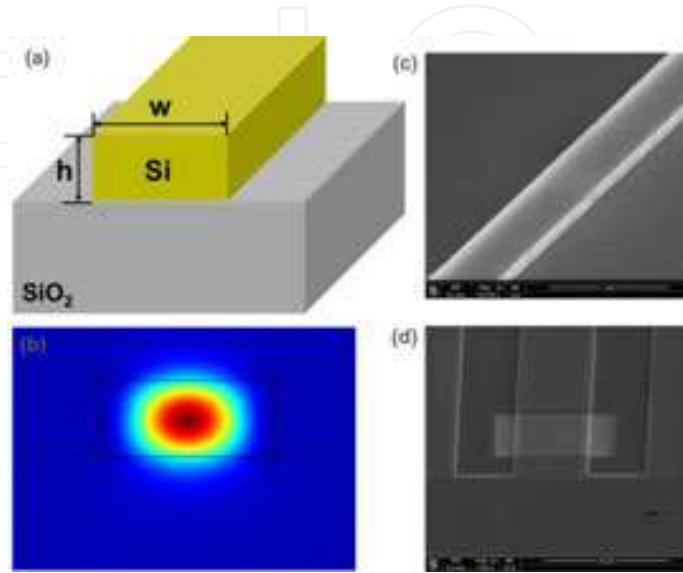


**Figure 2.** (a) Cross section and (b) calculated mode distribution of a typical silicon waveguide. (c)(d) Measured scanning electron microscope (SEM) images of the fabricated silicon waveguide and grating coupling region.

Figure 3 illustrates the wavelength conversion process based on degenerate FWM in a silicon waveguide. One OFDM m-QAM carrying data signal and one continuous-wave (CW) pump are launched into the silicon waveguide. When propagating along the silicon waveguide, pump photons are annihilated to create signal photons and newly converted idler photons through degenerate FWM process. At the output of the silicon waveguide, the converted idler takes the OFDM m-QAM data information carried by the input signal and the wavelength conversion from input signal to output idler is achieved. It is noted that the performance degradation of high-base wavelength conversion by degenerate FWM process can be ascribed to the accumulated phase noise transferred from the input pump and signal. Since the constellations of higher-order modulations (e.g., 16/32/64/128-QAM) inherently have a smaller phase noise tolerance due to the smaller spacing between adjacent constellation points, it is challengeable to realize high-base wavelength conversion of OFDM m-QAM signals, especially for higher-order modulations such as OFDM 16/32/64/128-QAM.

Shown in Fig. 4 is the experimental setup for high-base wavelength conversion of OFDM 16/32/64/128-QAM signals using a silicon waveguide. At the transmitter, an external cavity laser (ECL1) at 1563.849 nm is modulated by a single-polarization optical I/Q modulator. An arbitrary waveform generator (AWG) running at 10 GS/s sampling rate is used to produce the electrical OFDM m-QAM signal ( $m=16, 32, 64, 128$ ). The transmitted OFDM signal is generated off-line from a data sequence of  $2^{31}-1$  pseudo random binary sequences (PRBS) and then mapped onto m-QAM constellation. The OFDM m-QAM signal is constructed by 82 subcar-



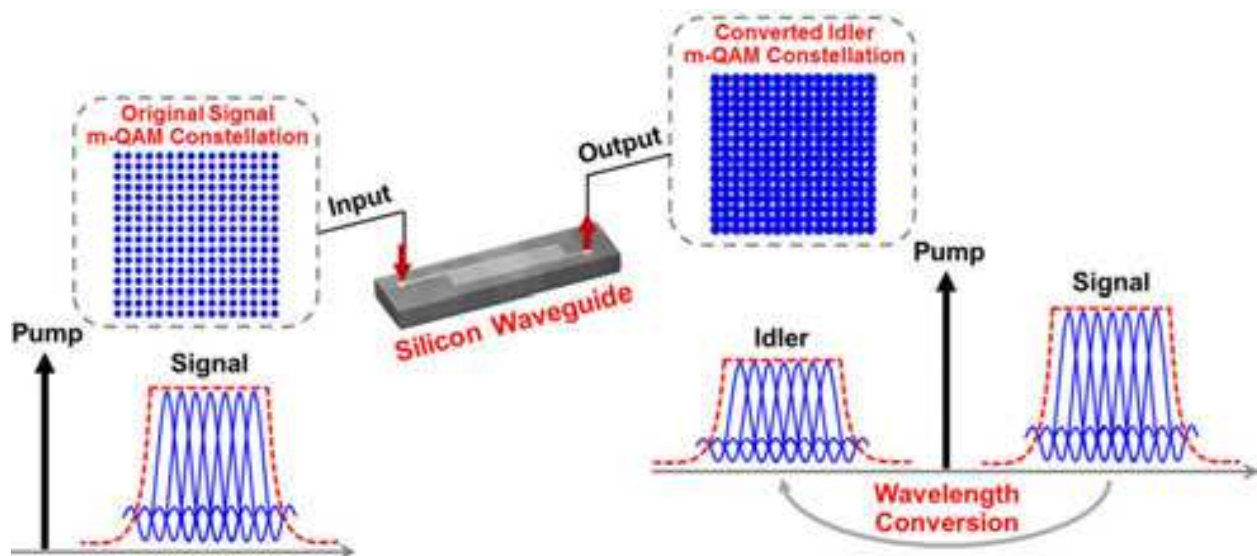


**Figure 3.** Illustration of high-base wavelength conversion of OFDM m-QAM signals based on degenerate FWM in a silicon waveguide.

riers, in which 78 subcarriers are used to carry the payloads with m-QAM signal, while 4 subcarriers are selected as the pilots with 4-QAM loading to estimate the phase noise. Another inverse fast Fourier transform (IFFT) with a size of 256 is used to convert the signal to time domain. No cyclic prefix (CP) is used as the signal passes through a system without dispersion-dominated devices. For the channel estimation, 10 training symbols are used for every 468 payload symbols in a manner of  $[A \ 0]$ , where “A” denotes one OFDM m-QAM symbol. Another ECL (ECL2) employed as the pump is set at 1560.61 nm with a 6-dBm output power. Two polarization controllers (PC1, PC2) are used to adjust the polarization states of signal and pump, respectively. After the signal amplification by an erbium-doped fiber amplifier (EDFA1) with a maximum output power of 27 dBm and pump amplification by a second EDFA (EDFA2) with a maximum output power of 30 dBm, the signal and pump are combined with a wavelength selective switch (WSS) and then vertically coupled into the silicon waveguide, in which degenerate FWM process takes place to enable the wavelength conversion from the signal to the converted idler. In the experiment, the signal is amplified to 25.5 dBm by EDFA1 and the pump is amplified to 27 dBm by EDFA2. The WSS not only combines the amplified signal and pump together but also suppresses the amplified spontaneous emission (ASE) noise from two EDFAs. After the wavelength conversion, the signal, pump, and newly converted idler are vertically coupled out from the silicon waveguide. After the amplification by a third EDFA (EDFA3), the converted idler is filtered using a tunable optical filter (TOF) with a bandwidth of 0.4 nm. A variable optical attenuator (VOA) and one more EDFA (EDFA4) are employed to adjust the received optical signal-to-noise ratio (OSNR) for proper detection by the coherent receiver. At the receiver, the optical signal is first mixed with a local oscillator (LO) by an optical hybrid and detected by a typical balanced coherent receiver. The line width of the employed laser sources including ECL1, ECL2, and LO in the experiment is around 100 kHz. The obtained two radio frequency (RF) signals for the IQ components are sent into a Tektronix real-time digital oscilloscope acquired at 50 GS/s and processed off-line with a

MATLAB program. The offline digital processing of the received signal includes: 1) carrier frequency offset estimation and OFDM window synchronization; 2) fast Fourier transform (FFT); 3) channel estimation; 4) phase noise estimation (crucial to m-QAM signal); 5) constellation decision and bit-error rate (BER) calculation.

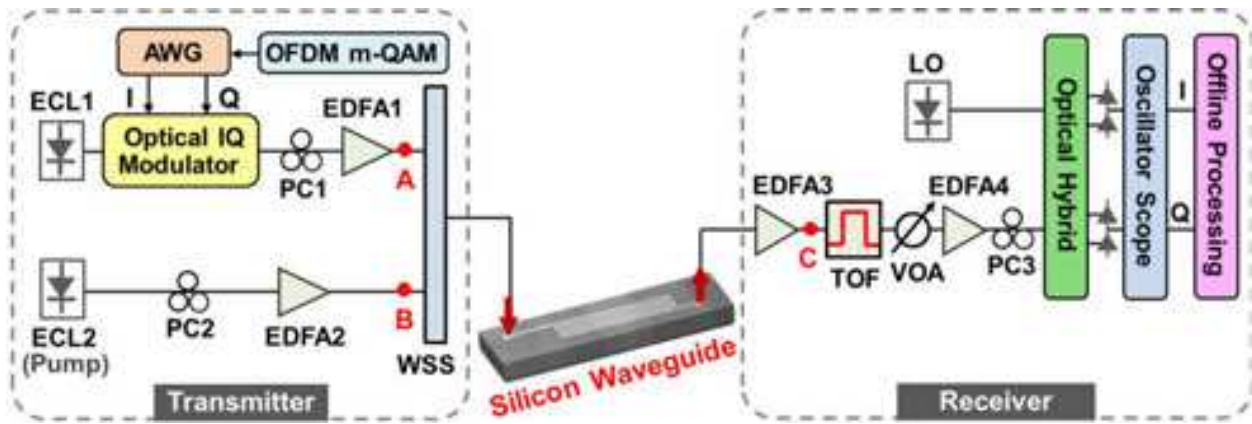


**Figure 4.** Experimental setup for high-base wavelength conversion of OFDM m-QAM signals using a silicon waveguide. ECL: external cavity laser; AWG: arbitrary waveform generator; PC: polarization controller; TOF: tunable optical filter; VOA: variable optical attenuator; LO: local oscillator; EDFA: erbium-doped fiber amplifier.

In order to characterize the performance of high-base wavelength conversion of OFDM m-QAM signals, we measure the BER curves as a function of received OSNR for back-to-back (B-to-B) and converted idler. Shown in Fig. 5(a)-(d) are measured BER performance for high-base wavelength conversions of OFDM 16-QAM, OFDM 32-QAM, OFDM 64-QAM, and OFDM 128-QAM, respectively. As shown in Fig. 5(a), for OFDM 16-QAM wavelength conversion the required OSNR at the 7% forward error correction (FEC) threshold ( $BER=1 \times 10^{-3}$ ) is 7.8 and 10.8 dB for the B-to-B signal and converted idler, respectively. The observed OSNR penalty is around 3 dB for OFDM 16-QAM wavelength conversion. Similarly, the received OSNR penalties of ~4 dB at 7% FEC threshold in Fig. 5(b), ~3.5 dB in Fig. 5(c) at 20% FEC threshold and ~4.5 dB in Fig. 5(d) at 20% FEC threshold are observed for high-base wavelength conversions of OFDM 32-QAM, OFDM 64-QAM, and OFDM 128-QAM, respectively. The right insets of Fig. 5(a)-(d) depict corresponding constellations of the B-to-B signals and converted idlers at the given OSNR values. One can see clear constellations of converted idlers, indicating favorable operation performance achieved for on-chip, high-base, all-optical wavelength conversions of multicarrier, multilevel modulation (OFDM 16/32/64/128-QAM) signals using a silicon waveguide.

### 3. High-base optical data exchange [71, 73, 74, 86]

We propose and demonstrate high-base all-optical data exchange of advanced multilevel modulation signals based on degenerate/nondegenerate FWM in HNLFs or silicon-organic hybrid slot waveguides.

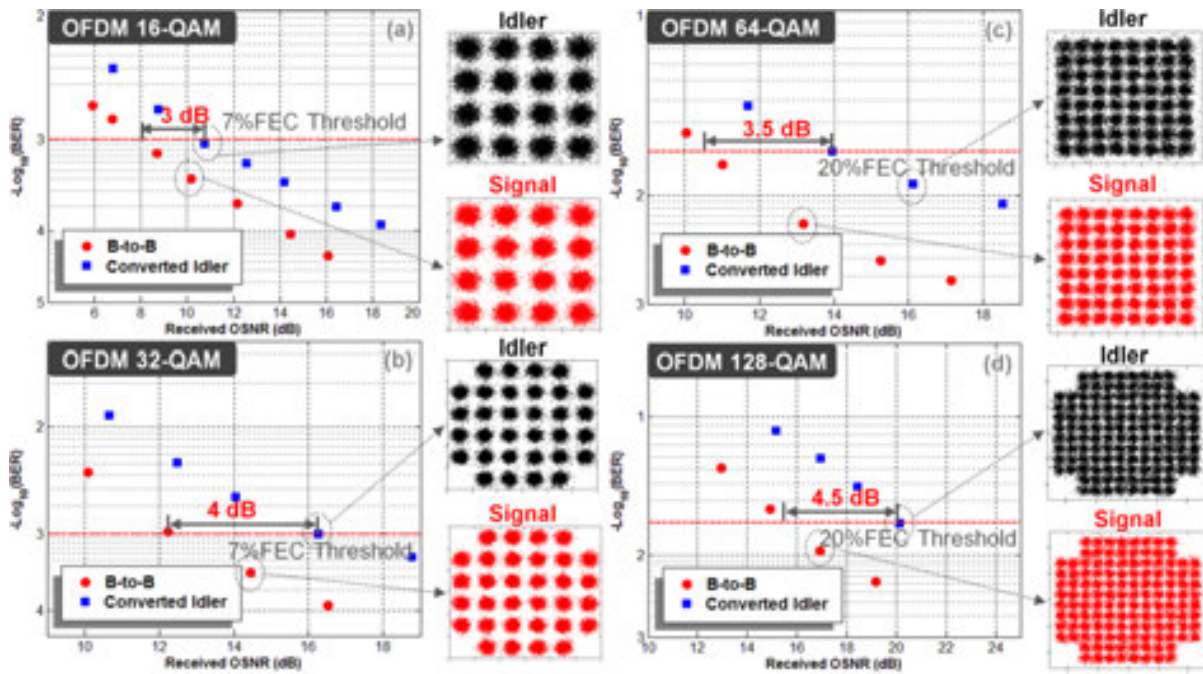


**Figure 5.** Measured BER versus received OSNR for high-base wavelength conversions of multicarrier, multilevel modulation signals. (a) OFDM 16-QAM. (b) OFDM 32-QAM. (c) OFDM 64-QAM. (d) OFDM 128-QAM.

We first demonstrate high-base optical data exchange of 100-Gbit/s return-to-zero differential QPSK (RZ-DQPSK) signals. The concept and principle for high-base optical data exchange of DQPSK modulation signals between two different wavelengths ( $S1:\lambda_{S1}$ ,  $S2:\lambda_{S2}$ ) are depicted in Fig. 6. The four-level phase information carried by two DQPSK signals at different wavelengths is swapped after the data exchange, as shown in Fig. 6(a). To perform high-base optical data exchange of DQPSK signals carrying phase information, the optical data exchange operation is expected to be phase transparent. Using the parametric depletion effect in a single HNLF, one may realize phase-transparent optical data exchange. Figure 6(b) depicts the principle of operation of parametric depletion. Two CW pumps ( $P1:\lambda_{P1}$ ,  $P2:\lambda_{P2}$ ) and signal 1 ( $S1:\lambda_{S1}$ ) are fed into the HNLF.  $P1$  and  $S1$  are symmetrical about the zero-dispersion wavelength (ZDM) of HNLF. When propagating along the HNLF, the photons of  $P1$  and  $S1$  are annihilated to create the photons of  $P2$  and  $S2$  ( $1/\lambda_{S2} + 1/\lambda_{P2} = 1/\lambda_{S1} + 1/\lambda_{P1}$ ) by the nondegenerate FWM process. Thus, the parametric depletion of  $S1$  is expected with its data information copied onto a newly generated  $S2$ . Similarly, the depletion of  $S2$  accompanied by the creation of  $S1$  is realized during the nondegenerate FWM process when sending two pumps and  $S2$  into the HNLF. Figure 6(c) shows the principle of operation of optical data exchange. Two pumps and two signals are simultaneously launched into the HNLF. When  $P1(P2)$  and  $S1(S2)$  are almost symmetrical about the ZDW of HNLF,  $S1(S2)$  can be consumed to produce  $S2(S1)$  by appropriately adjusting the power of two pumps. As a consequence, one can implement optical data exchange between two signals ( $S1$ ,  $S2$ ).

Remarkably, under the nondepletion approximation and proper control of pump powers, one can easily derive linear relationships ( $A_{S1}' \propto A_{S2} \cdot A_{P2} \cdot A_{P1}^*$ ,  $A_{S2}' \propto A_{S1} \cdot A_{P1} \cdot A_{P2}^*$ ) of complex



amplitudes between the output signals ( $A_{S1}'$ ,  $A_{S2}'$ ) and input signals and pumps ( $A_{S1}$ ,  $A_{S2}$ ,  $A_{P1}$ ,  $A_{P2}$ ). The linear complex amplitude relationships imply that nondegenerate FWM-based high-base data exchange has the characteristic of transparency to the modulation format including the phase transparency. We can further obtain the phase relationships of  $\varphi_{S1}' = \varphi_{S2} + \varphi_{P2} - \varphi_{P1}$  and  $\varphi_{S2}' = \varphi_{S1} + \varphi_{P1} - \varphi_{P2}$ . It is worth noting that phase modulation is always applied to the pumps ( $\varphi_{P1}$ ,  $\varphi_{P2}$ ) to effectively suppress the stimulated Brillouin scattering (SBS) effect in HNLF. As a result, the pump power is efficiently utilized in the nondegenerate FWM process, which benefits the effective parametric depletion and data exchange. Remarkably, the pump phase transfer to the exchanged signals might cause serious trouble for the DQPSK data exchange. Fortunately, according to the deduced phase relationships, it is possible to cancel the pump phase transfer by applying the precisely identical phase modulation to the two pumps (i.e.,  $\varphi_{P1} = \varphi_{P2}$ ), which makes it possible to implement the high-base data exchange of DQPSK or other multilevel modulation signals containing phase information.

### Updated Figures

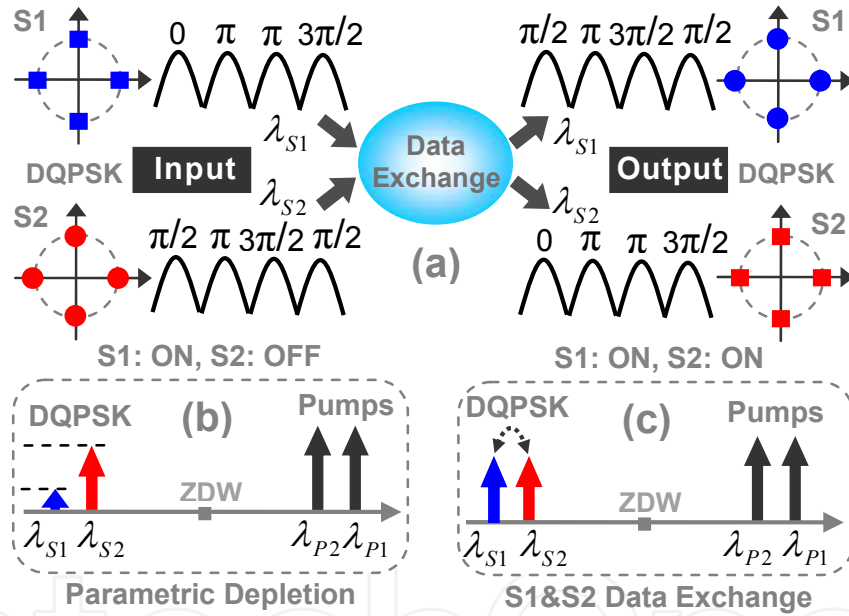


Figure 6. (a) Concept of high-base optical data exchange of DQPSK modulation signals. (b)(c) Principle of nondegenerate FWM-based parametric depletion and high-base optical data exchange.

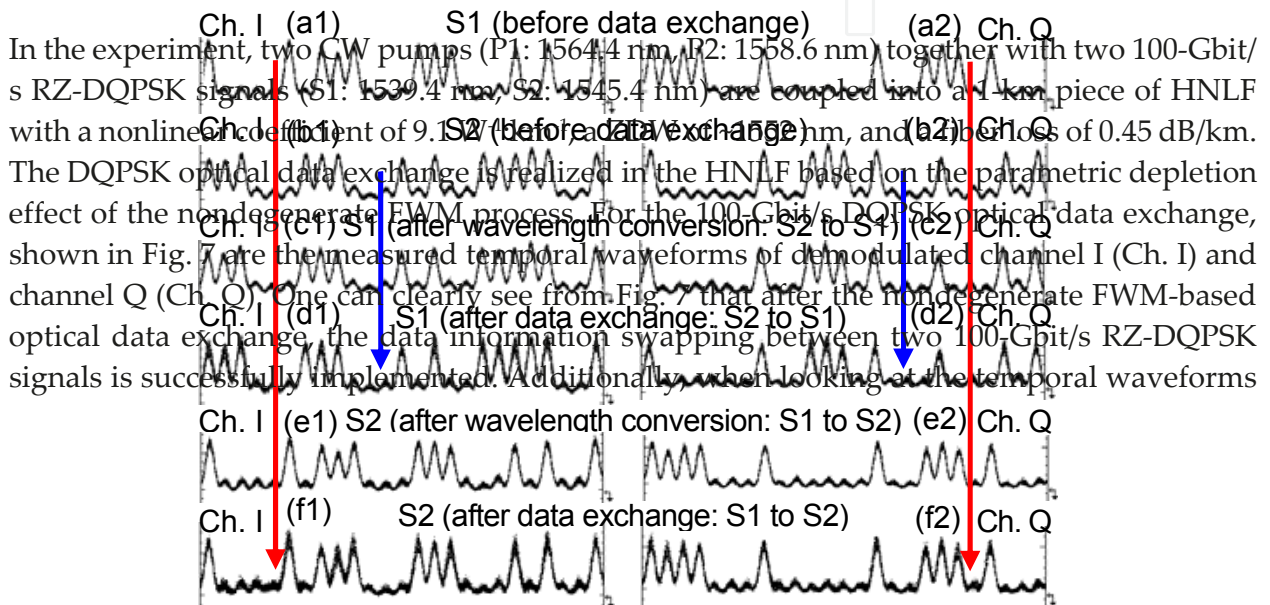


Figure 7. Measured temporal waveforms of demodulated channel I (Ch. I) and channel Q (Ch. Q) for high-base optical data exchange of 100-Gbit/s DQPSK signals. (1) (2) S1 is ON, P1 is OFF, and P2 is OFF. (1) (1) (2) S2 is ON, P1 is OFF, and P2 is OFF.

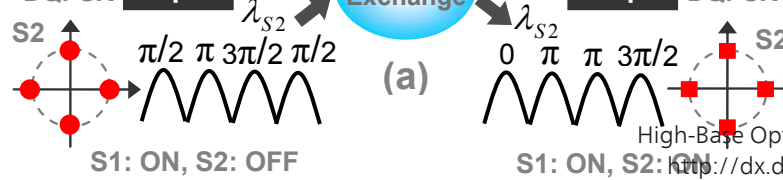


Figure 6. (a) Concept of high-base optical data exchange of DQPSK modulation signals. (b)(c) Principle of nondegenerate FWM-based parametric depletion and high-base optical data exchange.

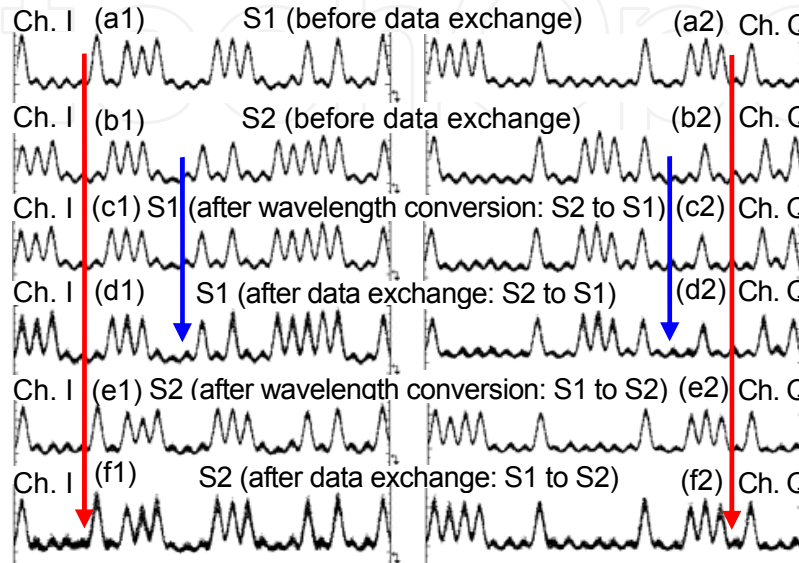


Figure 7. Measured temporal waveforms of demodulated channel I (Ch. I) and channel Q (Ch. Q) for high-base optical data exchange of 100-Gbit/s DQPSK signals. (a1)(a2) S1 is ON, P1 is OFF, and P2 is OFF. (b1)(b2) S2 is ON, P1 is OFF, and P2 is OFF. (c1)(c2) S2 to S1 wavelength conversion. S1 is OFF, S2 is ON, P1 is ON, and P2 is ON. (d1)(d2) S2 to S1 data exchange. S1 is ON, S2 is ON, P1 is ON, and P2 is ON. (e1)(e2) S1 to S2 wavelength conversion. S1 is ON, S2 is OFF, P1 is ON, and P2 is ON. (f1)(f2) S1 to S2 data exchange. S1 is ON, S2 is ON, P1 is ON, and P2 is ON.

Shown in Fig. 8 is the measured BER performance and balanced eyes for high-base optical data exchange of 100-Gbit/s DQPSK signals. One can see from Fig. 8 that for wavelength conversion with only S1 or S2 and two pumps present, the power penalty is assessed to be less than 1.2 dB at a BER of  $10^{-2}$ . In contrast, for data exchange with both two signals and two pumps present, the power penalty is measured to be less than 5 dB at a BER of  $10^{-2}$ . It is expected that the extra power penalty of the high-base data exchange compared to the wavelength conversion could be due to the beating effect between the newly converted signal and the original residual signal.

We further investigate the tolerance of pump misalignment and the dynamic range of input signal power for the 100-Gbit/s RZ-DQPSK data exchange. Shown in Fig. 9 is the measured relative power penalty as a function of the pump misalignment. One can clearly see that the performance degradation of wavelength conversion and data exchange becomes severe when the pump misalignment is larger than  $\pi/2$  ps. Actually, under relatively large pump phase misalignment, the residual phase due to incomplete pump phase cancellation is transferred to the phase noise added to the wavelength converted signal and data exchanged signal, resulting in the degradation of operation performance. Under different pump phase misalignments, the measured typical balanced eyes of demodulated signals after data exchange are also shown in

Figure 11. Concept and principle of simultaneous multichannel, high-base data exchange of DQPSK signals. Shown in Fig. 9 is the measured relative power penalty as a function of the pump misalignment. One can clearly see that the performance degradation of wavelength conversion and data exchange becomes severe when the pump misalignment is larger than  $\pi/2$  ps. Actually, under relatively large pump phase misalignment, the residual phase due to incomplete pump phase cancellation is transferred to the phase noise added to the wavelength converted signal and data exchanged signal, resulting in the degradation of operation performance. Under different pump phase misalignments, the measured typical balanced eyes of demodulated signals after data exchange are also shown in

wavelength conversion with only S1 or S2 and two pumps present, the power penalty is assessed to be less than 1.2 dB at a BER of  $10^{-9}$ . In contrast, for data exchange with both two signals and two pumps present, the power penalty is measured to be less than 5 dB at a BER of  $10^{-9}$ . It is expected that the extra power penalty of the high-base data exchange compared to the wavelength conversion could be due to the beating effect between the newly converted signal and the original residual signal.

36

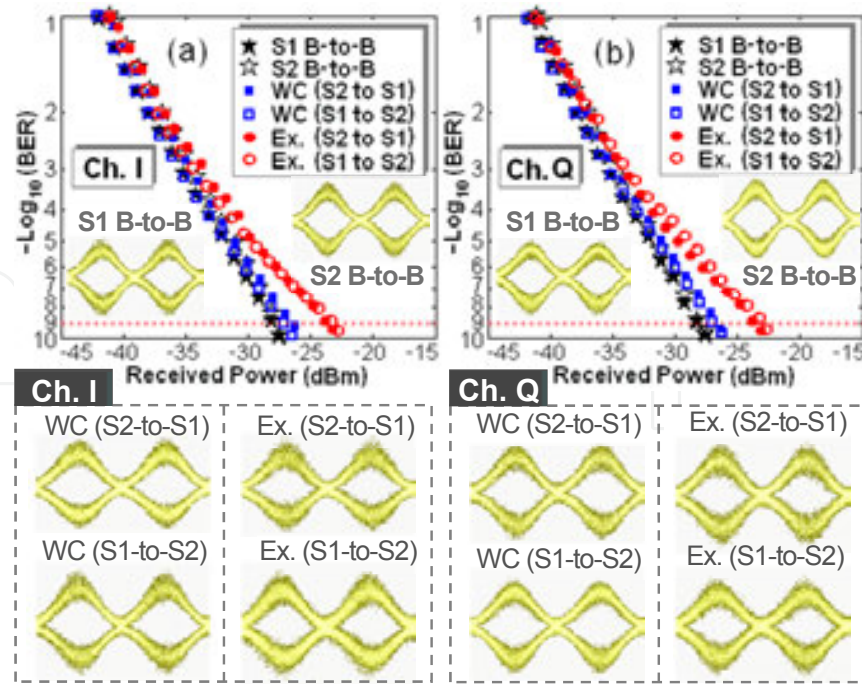


Fig. 8. BER curves and balanced eyes for high-base data exchange of 100-Gbit/s DQPSK signals. (a) Ch. I. (b) Ch. Q.

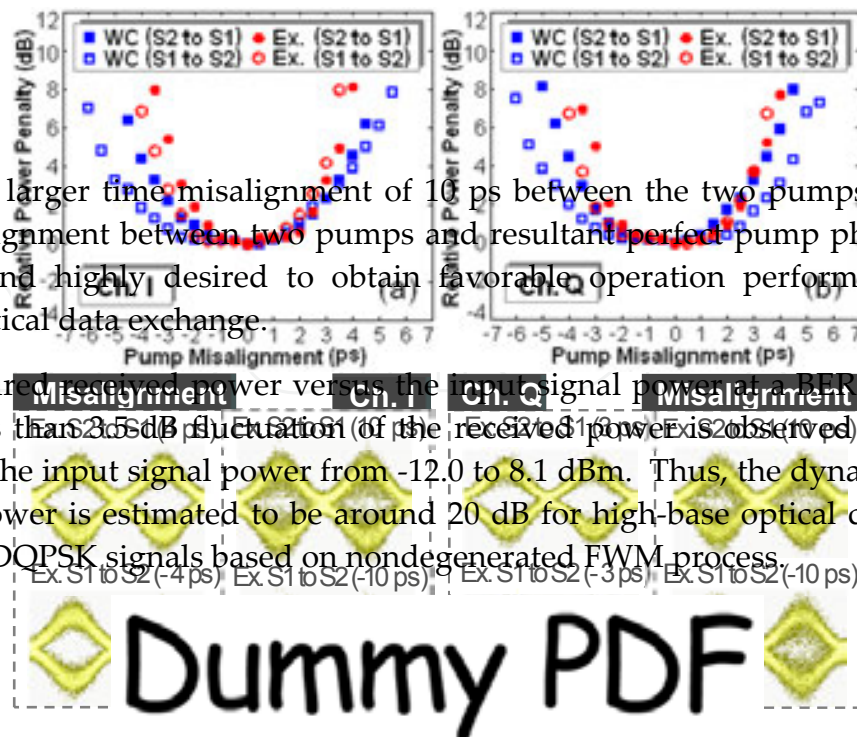
the insets of Fig. 9. By comparing the balanced eyes shown in Fig. 8 with perfectly aligned two pumps, one can observe the performance degradation with added noise under pump phase misalignment of 3 ps and 4 ps. Especially, one can observe almost completely closed eyes of demodulated signals after data exchange under an even larger time misalignment of 10 ps between the two pumps. Consequently, precise time alignment between two pumps and resultant perfect pump phase cancellation is important and highly desired to obtain favorable operation performance for phase-transparent optical data exchange.

The measured received power versus the input signal power at a BER of  $10^{-9}$  is shown in Fig. 10. Less than 3.5-dB fluctuation of the received power is observed at a BER of  $10^{-9}$  when varying the input signal power from -12.0 to 8.1 dBm. Thus, the dynamic range of the input signal power is estimated to be around 20 dB for high-base optical data exchange of 100-Gbit/s RZ-DQPSK signals based on nondegenerated FWM process.

We then propose and demonstrate a simple alternative method to perform high-base data exchange between multichannel DQPSK signals using bidirectional degenerate FWM in a single HNLF accompanied by optical filtering. The concept and operation principle of multichannel, high-base optical data exchange is illustrated in Fig. 11. Four-channel DQPSK signals (S1-S4) and a single CW pump are used. Degenerate FWM process is employed. Note that four-channel DQPSK signals (S1-S4) are symmetrical about the CW pump. For multichannel data exchange, one would expect to see simultaneous data information swapping between S1 and S4, S2 and S3. Generally speaking, for data exchange operation with two signals present, it is impossible to separate the newly converted signals from the original signals by unidirectional degenerate FWM process, so it is difficult to realize optical data



The measured received power versus the input signal power at a BER of  $10^{-9}$  is shown in Fig. 10. Less than 3.5-dB fluctuation of the received power is observed at a BER of  $10^{-9}$  when varying the input signal power from -12.0 to 8.1 dBm. Thus, the dynamic range of the input signal power is estimated to be around 20 dB for high-base optical data exchange of 100-Gbit/s RZ-DQPSK signals based on nondegenerated FWM process.



under an even larger time misalignment of 10 ps between the two pumps. Consequently, precise time alignment between two pumps and resultant perfect pump phase cancellation is important and highly desired to obtain favorable operation performance for phase-transparent optical data exchange.

The measured received power versus the input signal power at a BER of  $10^{-9}$  is shown in Fig. 10. Less than 3.5-dB fluctuation of the received power is observed at a BER of  $10^{-9}$  when varying the input signal power from -12.0 to 8.1 dBm. Thus, the dynamic range of the input signal power is estimated to be around 20 dB for high-base optical data exchange of 100-Gbit/s RZ-DQPSK signals based on nondegenerated FWM process.

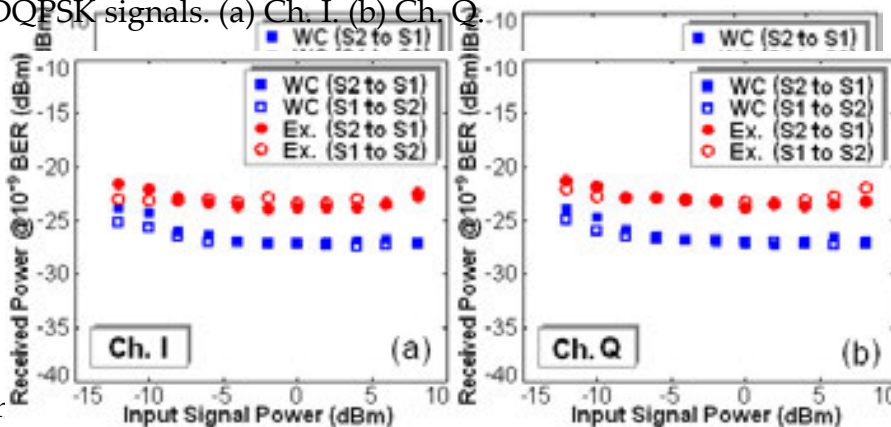


Figure 9. Impact of pump phase misalignment on the performance of high-base data exchange of 100-Gbit/s DQPSK signals. (a) Ch. I, (b) Ch. Q. Figure 10. Dynamic range of input signal power for high-base data exchange of 100-Gbit/s DQPSK signals. (a) Ch. I, (b) Ch. Q.

We then propose and demonstrate a simple alternative method to perform high-base exchange function based on unidirectional degenerate FWM in a single HNLF. We propose a data exchange between multichannel DQPSK signals using bidirectional degenerate FWM in a single HNLF accompanied by optical filtering. The concept and operation principle of multichannel, high-base optical data exchange is illustrated in Fig. 11, taking four-channel optical data exchange as an example, there are four-channel DQPSK signals ( $S_1$ - $S_4$ ) at the input. 1) With optical filtering,  $S_1$  and  $S_2$  are selected and fed into the HNLF together with the CW pump from the left side. When propagating along the HNLF,  $S_4$  and  $S_3$  are generated by the degenerate FWM wavelength conversion process. After the generation of  $S_4$  and  $S_3$ , the original  $S_1$ ,  $S_2$  and CW pump are suppressed, while the newly converted  $S_4$  and  $S_3$  are selected with two signals present, it is impossible to separate the newly converted signals from the original signals by unidirectional degenerate FWM process, so it is difficult to realize optical data exchange function based on unidirectional degenerate FWM in a single HNLF. We propose a possible solution by exploiting bidirectional degenerate FWM process in a single HNLF together with optical filtering. As illustrated in Fig. 11, taking four-channel optical data exchange as an example, there are four-channel DQPSK signals ( $S_1$ - $S_4$ ) at the input. 1)



Figure 6. (a) Concept of high-base optical data exchange of DQPSK modulation signals. (b)(c) Principle of nondegenerate FWM-based parametric depletion and high-base optical data exchange.

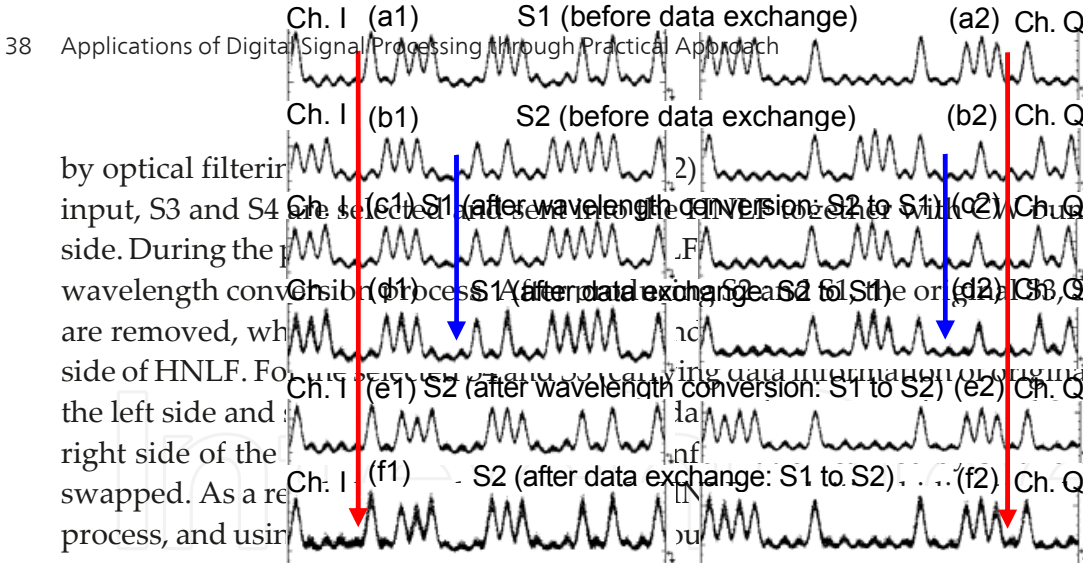


Figure 7. Measured temporal waveforms of demodulated channel I (Ch. I) and channel Q (Ch. Q) for high-base optical data exchange of 100-Gbit/s DQPSK signals after optical data exchange. Remarkably, since the degenerate FWM process has distinct phase-configuration property, for DQPSK signals the in-phase (Ch. I) and quadrature (Ch. Q) components are also swapped after the optical data exchange operation. (a1)(a2) S1 is ON, P1 is OFF, and P2 is OFF. (b1)(b2) S2 is ON, P1 is OFF, and P2 is OFF. (c1)(c2) S2 to S1 wavelength conversion. S1 is OFF, S2 is ON, P1 is ON, and P2 is ON. (d1)(d2) S2 to S1 data exchange. S1 is ON, S2 is ON, P1 is ON, and P2 is ON. (e1)(e2) S1 to S2 wavelength conversion. S1 is ON, S2 is OFF, P1 is ON, and P2 is ON. (f1)(f2) S1 to S2 data exchange. S1 is ON, S2 is ON, P1 is ON, and P2 is ON.

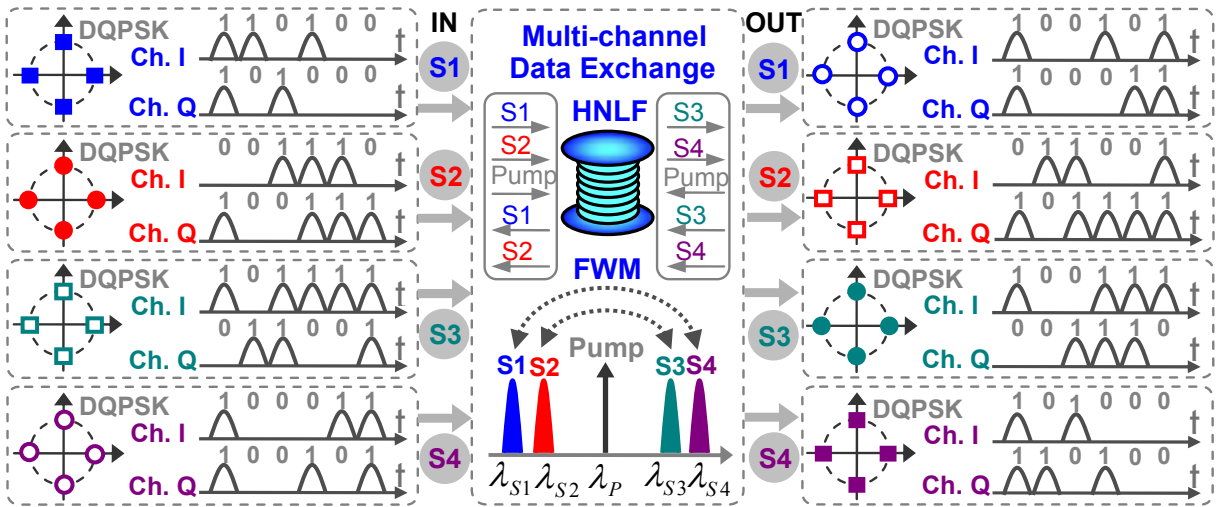


Figure 11. Concept and principle of simultaneous multichannel, high-base data exchange of DQPSK signals. **Figure 11.** Concept and principle of simultaneous multichannel, high-base data exchange of DQPSK signals.

In the experiment, the bidirectional degenerate FWM in a single HNLF is enabled by a fiber loop mirror configuration, which consists of an HNLF with a length of 460 m, two optical band-pass filters, and optical fiber couplers. The typical parameters of the HNLF are as follows: ZDW:  $\sim 1556$  nm; nonlinear coefficient:  $20 \text{ W}^{-1} \cdot \text{km}^{-1}$ ; dispersion slope (S):  $\sim 0.026 \text{ ps/nm}^2/\text{km}$ . Compared to the nondegenerate FWM-based data exchange with two pumps, single pump with its wavelength ( $1554.94$  nm) close to the ZDW of HNLF is employed in the bidirectional degenerate FWM-based multichannel, high-base data exchange. ITU-grid-compatible four-channel 100-Gbit/s RZ-DQPSK signals (S1:  $1546.12$  nm, S2:  $1547.72$  nm, S3:  $1562.23$  nm, S4:  $1563.86$  nm) are employed for multichannel, high-base data exchange.

Shown in Fig. 12(a) is the measured spectrum of input four-channel, 100-Gbit/s RZ-DQPSK signals. S1(S2) and S4(S3) are symmetrical about the CW pump. The measured spectrum after

four-channel optical data exchange with the CW pump ON is shown in Fig. 12(b) (solid blue line). For reference, the measured spectrum of residual signals with the CW pump OFF is also shown in Fig. 12(b) (dashed red line). It is expected that the residual signals are caused by the Rayleigh scattering in the HNLF. From Fig. 12(b), one can measure the extinction ratio of the newly exchanged signals to the residual signals to be 18.4 dB for S1, 19.5 dB for S2, 17 dB for S3, and 17 dB for S4, respectively.

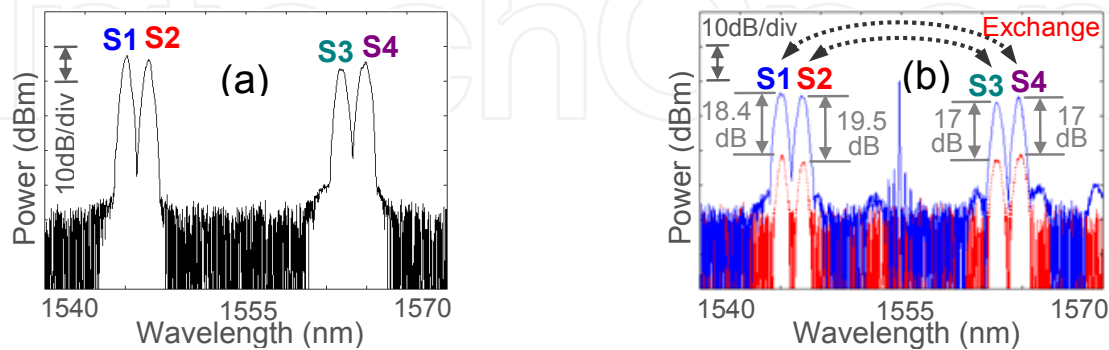


Figure 12. Spectra for four-channel, high-base data exchange of DQPSK signals. (a) Input four-channel, 100-Gbit/s RZ-DQPSK signals. (b) Spectra measured in the absence (dashed curve: Rayleigh scattering)/presence (solid curve: after data exchange) of CW pump.

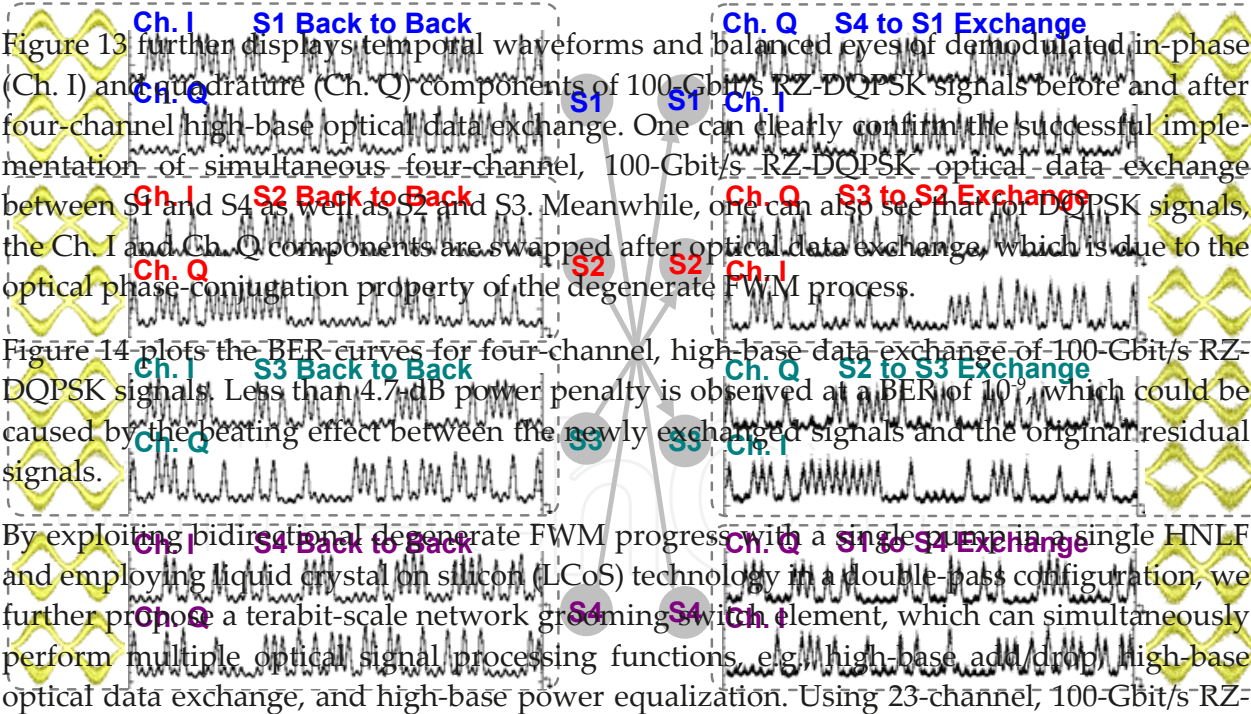


Figure 13. Temporal waveforms and balanced eyes of demodulated in-phase (Ch. I) and quadrature (Ch. Q) components for four-channel high-base data exchange of 100-Gbit/s RZ-DQPSK signals.

By exploiting bidirectional degenerate FWM progress with a single pump in a single HNLF and employing liquid crystal on silicon (LCoS) technology in a double-pass configuration, we further propose a terabit-scale network grooming switch element, which can simultaneously perform multiple optical signal processing functions, e.g. high-base add/drop, high-base optical data exchange, and high-base power equalization. Using 23-channel, 100-Gbit/s RZ-DQPSK signals and balanced eyes of demodulated in-phase (Ch. I) and quadrature (Ch. Q) components for four-channel high-base data exchange of 100-Gbit/s RZ-DQPSK signals.

Shown in Fig. 15 is the concept and operation principle of the proposed high-base, multifunctional grooming switch element that could be used at the network nodes. When multiple

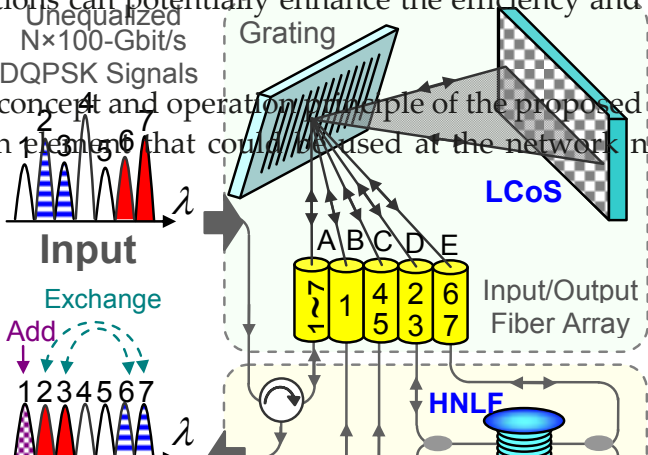




Fig. 12. Spectra for four-channel, high-base data exchange of DQPSK signals. (a) Input four-channel, 100-Gbit/s RZ-DQPSK signals. (b) Spectra measured in the absence (dashed curve: Rayleigh scattering)/presence (solid curve) of data exchange. (c) CW pump.

Figure 13 further displays temporal waveforms and balanced eyes of demodulated in-phase (Ch. I) and quadrature (Ch. Q) components of 100-Gbit/s RZ-DQPSK signals before and after four-channel high-base optical data exchange. One can clearly confirm the successful implementation of simultaneous four-channel, 100-Gbit/s RZ-DQPSK optical data exchange between S1 and S4 as well as S2 and S3. Meanwhile, one can also see that for DQPSK signals, the Ch. I and Ch. Q components are swapped after optical data exchange, which is due to the optical phase-conjugation property of the degenerate FWM process.

Dummy PDF

Fig. 13. Waveforms and balanced eyes of demodulated in-phase (Ch. I) and quadrature (Ch. Q) components for four-channel, high-base data exchange of 100-Gbit/s DQPSK signals.

Figure 14 plots the BER curves for four-channel, high-base data exchange of 100-Gbit/s RZ-DQPSK signals. Less than 4.7-dB power penalty is observed at a BER of  $10^{-9}$ , which could be caused by the data exchange between the exchanged signals and the original residual signals.

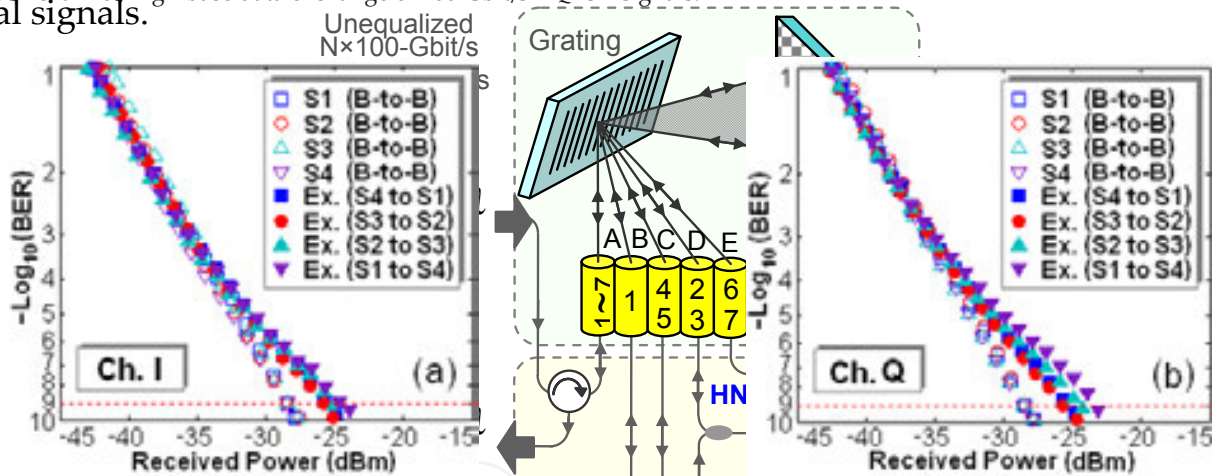


Fig. 14. Measured BER curves for simultaneous four-channel, high-base data exchange of 100-Gbit/s DQPSK signals.

By exploiting bidirectional degenerate FWM progress with a single pump in a single HNLF, and employing liquid crystal on silicon (LCoS) technology in a double-pass domain, in order to reduce the network latency and enhance the network efficiency. The typical configuration we further propose a terabit-scale network grooming switch element, which can simultaneously perform multiple optical signal processing functions, e.g., high-base add/drop, high-base optical data exchange, and high-base power equalization. Using 23-channel, 100-Gbit/s RZ-DQPSK signals, we demonstrate reconfigurable 2.3-Tbit/s network grooming switch operation in the experiment. Remarkably, simultaneous implementation of all these high-base optical signal processing functions can potentially enhance the efficiency and flexibility of network management.

7-channel WDM signals. A wavelength selective switch (WSS) using a two-dimensional (2D) array of LCoS pixels is employed in the setup. The operation principle of the LCoS-based WSS is as follows. By changing the voltages loaded to the LCoS, one can adjust the phase retardance of each pixel of LCoS. The 2D LCoS array includes two axes with one horizontal wavelength axis and the other vertical displacement axis. The input 7-channel 100-Gbit/s DQPSK signals with unequalized power levels are sent to the port A of the input/output fiber array through a circulator. A diffraction grating collecting the input signals from port A then disperses different wavelength channels to different horizontal positions of the LCoS. Along the vertical direction, many pixels (~400 pixels) are covered due to the divergence of the light. The manipulation mechanism relies on the control of the LCoS. Since the phase shift of each pixel of LCoS can be adjusted by varying its applied voltage, it is possible to flexibly manipulate the phase front of the light through the control of the 2D array of LCoS pixels. By appropriately adjusting the independent pixel voltage, the propagation direction of different wavelength channels can be flexibly controlled, i.e., different wavelength channels can be delivered to different spatial positions at the output ports (e.g., S1 sent to port B, S4 and S5 sent to port C, S2 and S3 sent to port D, S6 and S7 sent to port E). Meanwhile, the power levels of different wavelength channels delivered to the desired fiber array ports (port B, port C, port D, port E) can be also adjusted. After separating and delivering different wavelength channels to different output fiber array ports together with flexible power control, various grooming optical signal processing functions can be carried out on these output fiber array ports: 1) high-base optical data exchange between port D and port E; 2) high-base wavelength add and drop at port B; 3) high-base power equalization of all wavelength channels. For the high-base optical data exchange between port D and port E, simultaneous multichannel, high-base optical data exchange between S2 and S7 and between S3 and S6 can be implemented by exploiting bidirectional degenerate FWM through a single HNLF. When compared to the similar optical data exchange scheme using degenerate FWM and employing optical band-pass filters to select desired wavelength channels, here the channel separation and selection are accomplished by LCoS. When compared to the optical data exchange approach using parametric depletion effect of nondegenerate FWM process with two pumps, here only single pump is employed in the setup. In particular, the simultaneous multichannel optical data exchange operation is switchable when employing the programmable LCoS. For the high-base wavelength add and drop, the S1 DQPSK signal is dropped at port B and a new S1 with updated data information is also added to port B through a circulator. For the high-base power equalization, the flexible attenuation control for all WDM channels is available by programming LCoS. Besides optical data exchange (S2 and S7, S3 and S6) and add/drop (S1) operations on the channels of interest, other channels (S4 and S5) without undergoing these operations should be kept and delivered back. A fiber loop structure could be employed at the port C. Remarkably, after multiple grooming optical signal processing operations, it is preferred that all the signals are sent back to the same input/output fiber array port A, which not only imports unequalized multiple WDM signals but also exports all the signals after the grooming switching. Such function can be implemented simply by running the LCoS device in a double-pass configuration assisted by use of some optical circulators. As shown in Fig. 15, if we consider the dashed boxes as a grooming switch unit based on HNLF and LCoS, it is actually a multifunctional, high-base



grooming optical signal processing element with great reconfigurability. Simultaneous reconfigurable high-base add/drop, high-base optical data exchange, and high-base power equalization are implemented by exploiting bidirectional degenerate FWM in a single HNLF and double-pass programmable LCoS technology.

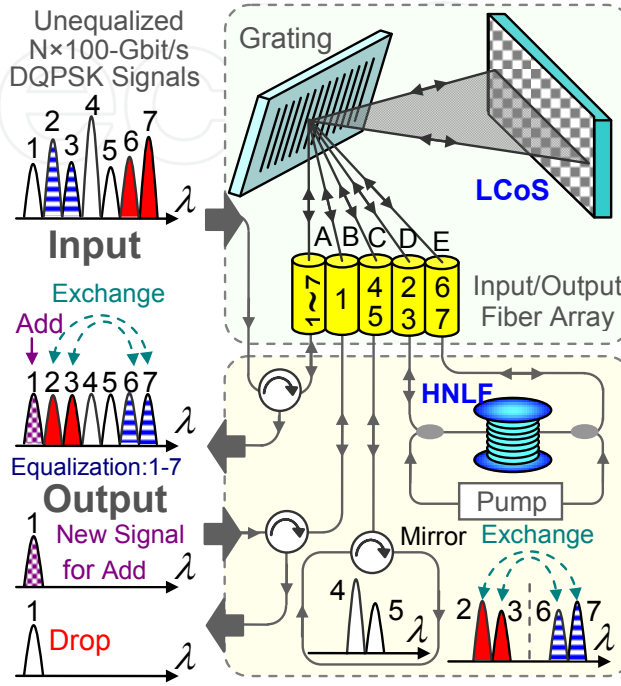


**Figure 15.** Concept and principle of LCoS+HNLF-based multifunctional, high-base grooming switch (add/drop, data exchange, power equalization).

Similar operation principle is adopted for reconfigurable 2.3-Tbit/s network grooming switch with 23x100-Gbit/s RZ-DQPSK channels. In the experiment, ITU-grid-compatible 23 wavelength channels (from S1: 1531.12 nm to S23: 1566.31 nm) each carrying 100-Gbit/s RZ-DQPSK modulation signal with a channel spacing of 200 GHz are utilized. A 520-m piece of HNLF with a ZDW of ~1555 nm and a nonlinear coefficient ( $\gamma$ ) of 20 W<sup>-1</sup>·km<sup>-1</sup> is employed. The single pump wavelength is set to be 1555.75 nm for bidirectional degenerate FWM.

Figure 16 shows the measured optical spectrum and balanced eyes for input unequalized 23 wavelength channels each carrying a 100-Gbit/s RZ-DQPSK signal. The observed power fluctuation of all 23 wavelength channels is assessed to be around 9.1 dB. The insets of Fig. 16 depict measured typical balanced eyes for the demodulated in-phase (Ch. I) and quadrature (Ch. Q) components of 100-Gbit/s RZ-DQPSK signals.

We first perform 2.3-Tbit/s grooming switch with single-channel, high-base add/drop and two-channel high-base optical data exchange. The measured optical spectrum together with typical balanced eyes for 100-Gbit/s RZ-DQPSK signals after the multifunctional, high-base grooming switch is shown in Fig. 17. Three high-base grooming optical signal processing functions are implemented as follows: 1) high-base optical data exchange between S12 and S21; 2) high-base

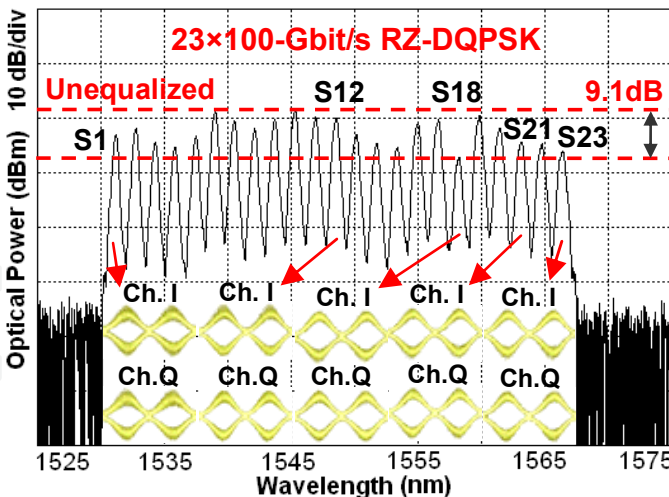
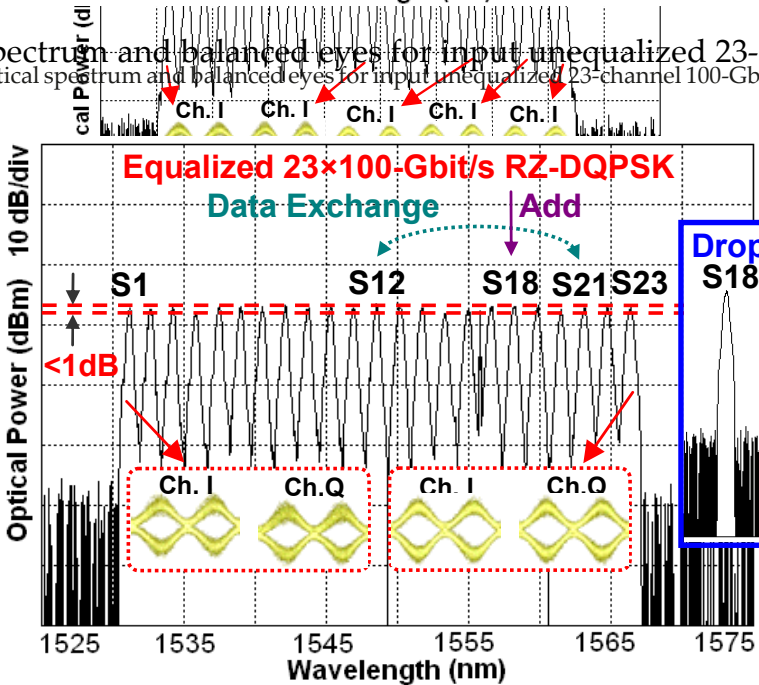


Figure 16. Measured optical spectrum and balanced eyes for input unequalized 23-channel 100-Gbit/s RZ-DQPSK signals.

dropping of the o  
3) high-base pow  
fluctuation: <1 dB  
the multichannel,

Figure 16. Measured optical signals.

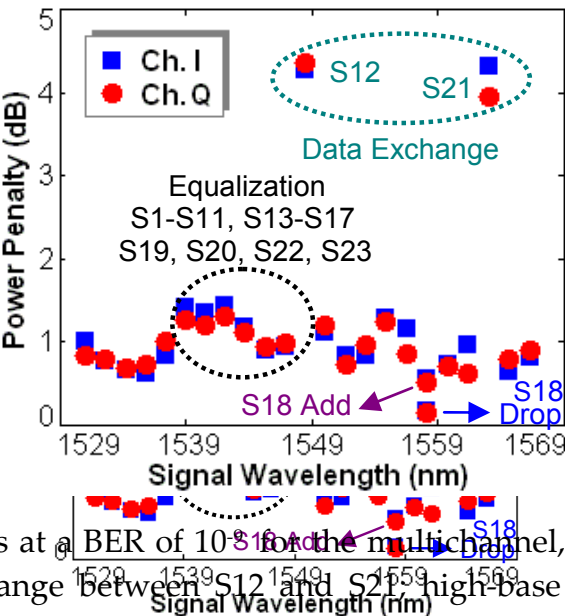


data information;  
< signals (power  
own in Fig. 18 for  
el 100-Gbit/s RZ-DQPSK

Figure 17. Measured optical spectrum and balanced eyes for 100-Gbit/s RZ-DQPSK signals after multifunctional high-base grooming switch (high-base optical data exchange between S1 and S21; high-base add/drop for S18; high-base power equalization for all 23 wavelength channels S1-S23).

Figure 17. Measured optical spectrum and balanced eyes for 100-Gbit/s RZ-DQPSK signals after multifunctional high-base grooming switch (high-base optical data exchange between S1 and S21; high-base add/drop for S18; high-base power equalization for all 23 wavelength channels S1-S23).

Due to the programmable multifunctional grooming switch, simultaneous multichannel channels of interest sent to



PSK signals after multifunctional, S21, high-base add/drop for S18; high-base power equalization for all 23 wavelength channels S1-S23).

Figure 18. Measured power penalties at a BER of  $10^{-3}$  for the multichannel, multifunctional high-base grooming switch (high-base optical data exchange between S1 and S21; high-base add/drop for S18; high-base power equalization for all 23 wavelength channels S1-S23).

Figure 17. Measured optical spectrum and balanced eyes for 100-Gbit/s RZ-DQPSK signals after multifunctional, high-base grooming switch (high-base optical data exchange between S12 and S21; high-base add/drop for S18; high-base power equalization for all 23 wavelength channels S1-S23).

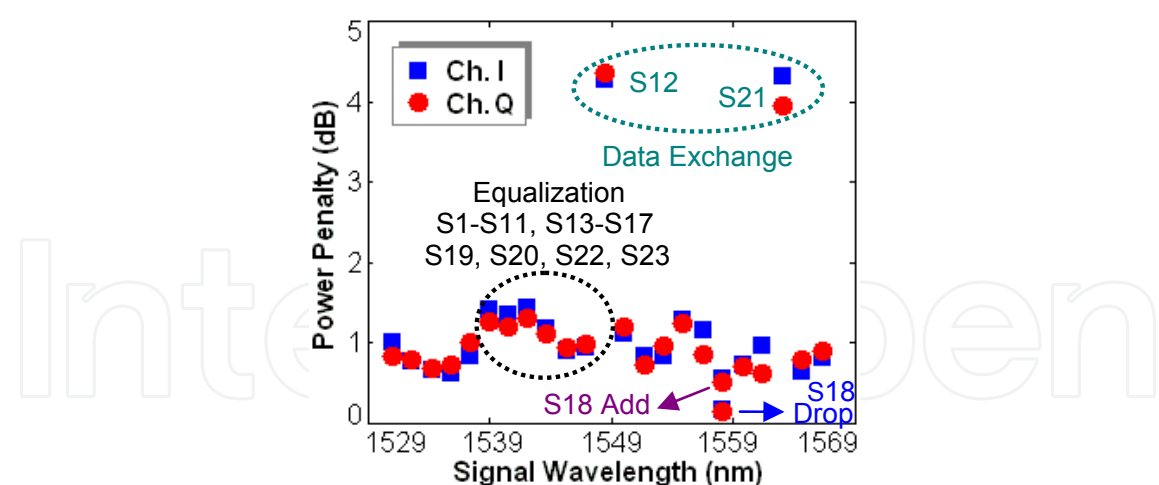
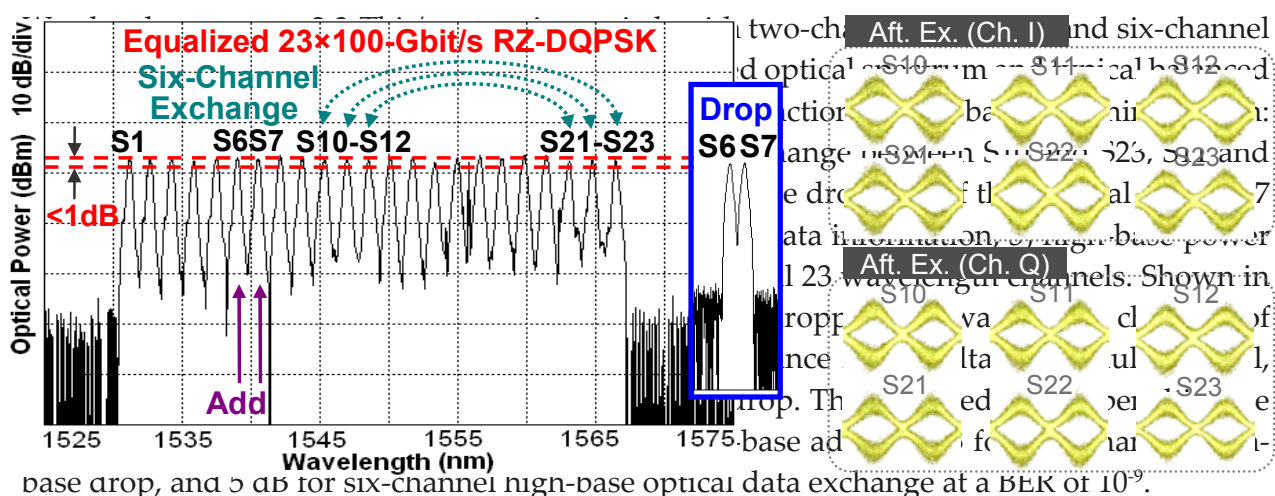


Figure 18. Measured power penalties at a BER of  $10^{-9}$  for the multichannel, multifunctional high-base grooming switch (high-base optical data exchange between S12 and S21; high-base add/drop for S18; high-base power equalization for all 23 wavelength channels S1-S23).



In addition to high-base data exchange based on degenerate/nondegenerate FWM in HNLFs, we also propose and simulate ultrahigh-speed high-base data exchange using nondegenerate FWM in a silicon-organic hybrid slot waveguide. The working principle is also based on the parametric depletion effect of nondegenerate FWM as in an HNLF. The designed silicon-organic hybrid slot waveguide offers tight light confinement, enhanced nonlinearity, and negligible TPA and free-carrier absorption (FCA). Using nonlinear coupled-mode equations under the slowly varying envelope approximation and taking full consideration of group-velocity mismatching (GVM), group-velocity dispersion (GVD), TPA, FCA, and free-carrier dispersion (FCD), the proposed silicon-organic hybrid slot waveguide based high-base data exchange is simulated. In the following simulations, two 640 Gbaud  $2^{13}-1$  pseudorandom binary sequence (PRBS) 16-QAM/64-QAM signals ( $\lambda_{SA}$ : 1542 nm,  $\lambda_{SB}$ : 1544 nm) and two pumps ( $\lambda_{P1}$ : 1548 nm,  $\lambda_{P2}$ : 1550 nm) are sent into a 17-mm-long silicon-organic hybrid slot waveguide, in which 16-QAM/64-QAM data exchange is realized based on the nondegenerate FWM process. Note that the high-speed 640 Gbaud 16-QAM/64-QAM signal could be optical time-



Figure 18. Measured power penalties at a BER of  $10^{-9}$  for the multichannel, multifunctional high-base grooming switch (high-base optical data exchange between S12 and S21; high-base add/drop for S18; high-base power equalization for all 23 wavelength channels S1-S23).

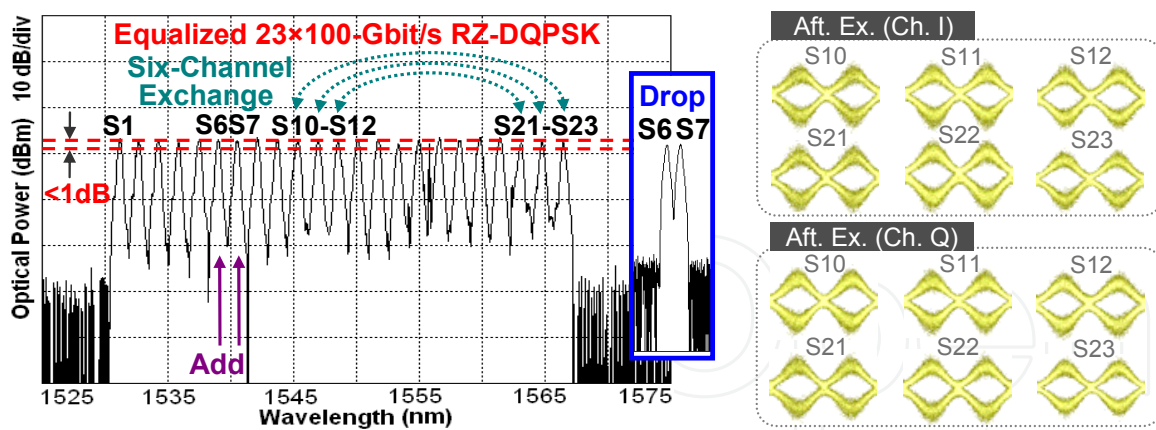


Fig. 19. Measured optical spectrum and balanced eyes for 100-Gbit/s RZ-DQPSK signals after multichannel, multifunctional high-base grooming switch (simultaneous six-channel, high-base high-base grooming switch (simultaneous six-channel, high-base optical data exchange between S10 and S23, S11 and S22, S12 and S21; simultaneous two-channel, high-base add/drop for S6 and S7; high-base power equalization for all 23 wavelength channels S1-S23).

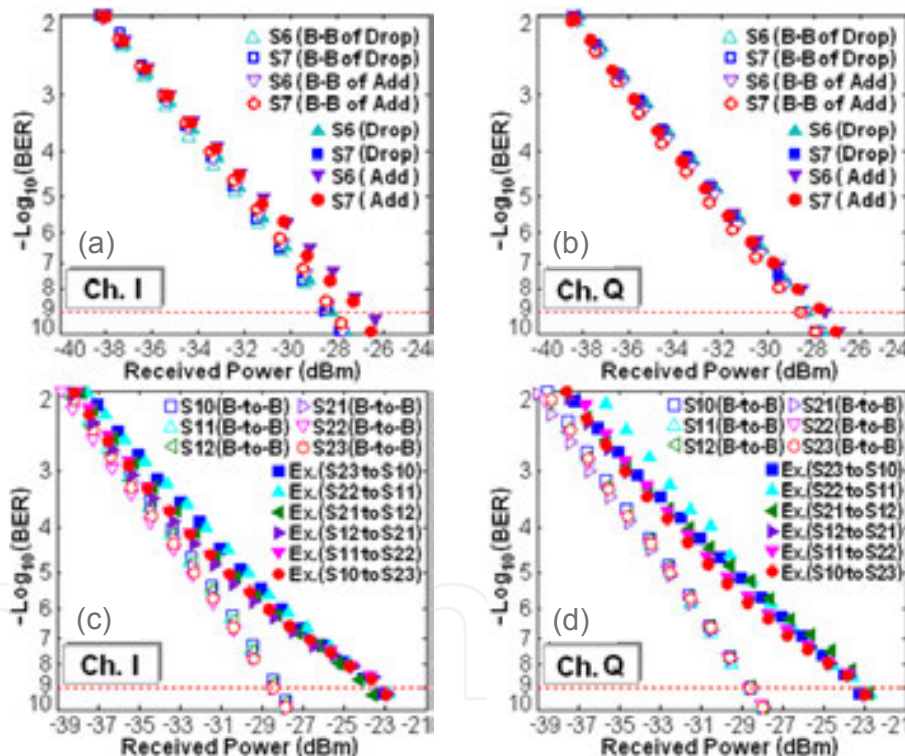


Fig. 20. Measured BER performance for (a)(b) simultaneous two-channel, high-base add/drop (S6 and S7) and (c)(d) simultaneous six-channel, high-base optical data exchange between S10 and S23, S11 and S22, S12 and S21.

division multiplexed (OTDM) signal from 64 low-speed, 10 Gbaud tributaries in practical applications.

In addition to high-base data exchange based on degenerate/nondegenerate FWM in HNLFs, we also propose and simulate ultrahigh-speed high-base data exchange using nondegenerate FWM in a silicon-organic hybrid slot waveguide. The working principle is also based on the parametric depletion effect of nondegenerate FWM as in an HNLF. The designed silicon-organic hybrid slot waveguide offers tight light confinement, enhanced nonlinearity, and negligible TPA and free-carrier absorption (FCA). Using nonlinear coupled-mode equations under the slowly varying envelope approximation and taking full consideration of group-velocity mismatching (GVM), group-velocity dispersion (GVD), TPA, FCA, and free-carrier dispersion (FCD), the proposed silicon-organic hybrid slot waveguide based high-base data exchange is simulated. In the following simulations, two 640 Gbaud  $2^{13}-1$  pseudorandom binary sequence (PRBS) 16-QAM/64-QAM signals ( $\lambda_{SA}$ : 1542 nm,  $\lambda_{SB}$ :



realization of the proposed high-base optical data exchange of 16-QAM signals by comparing the 10 symbol sequences for two signals (SA, SB) before optical data exchange (Bef. Ex.) and after optical data exchange (Aft. Ex.). Figure 22 shows simulated constellations for high-base optical data exchange of 16-QAM signals. For a signal-to-noise ratio (SNR) of 10 dB the error vector magnitude (EVM) is also assessed in Fig. 22. The simulated EVM and BER performance versus SNR for high-base optical data exchange of 640 Gbaud (2.56 Tbit/s) 16-QAM signals is shown in Fig. 23(a) and (b). For reference we also plot in Fig. 23(b) the theoretical 16-QAM BER curve. By comparing the simulated BER curves of two signals before and after optical data exchange, one can see negligible SNR penalty induced by the high-base optical data exchange operation at a BER of  $2 \times 10^{-3}$ , which is the enhanced forward error correction (EFEC) threshold.

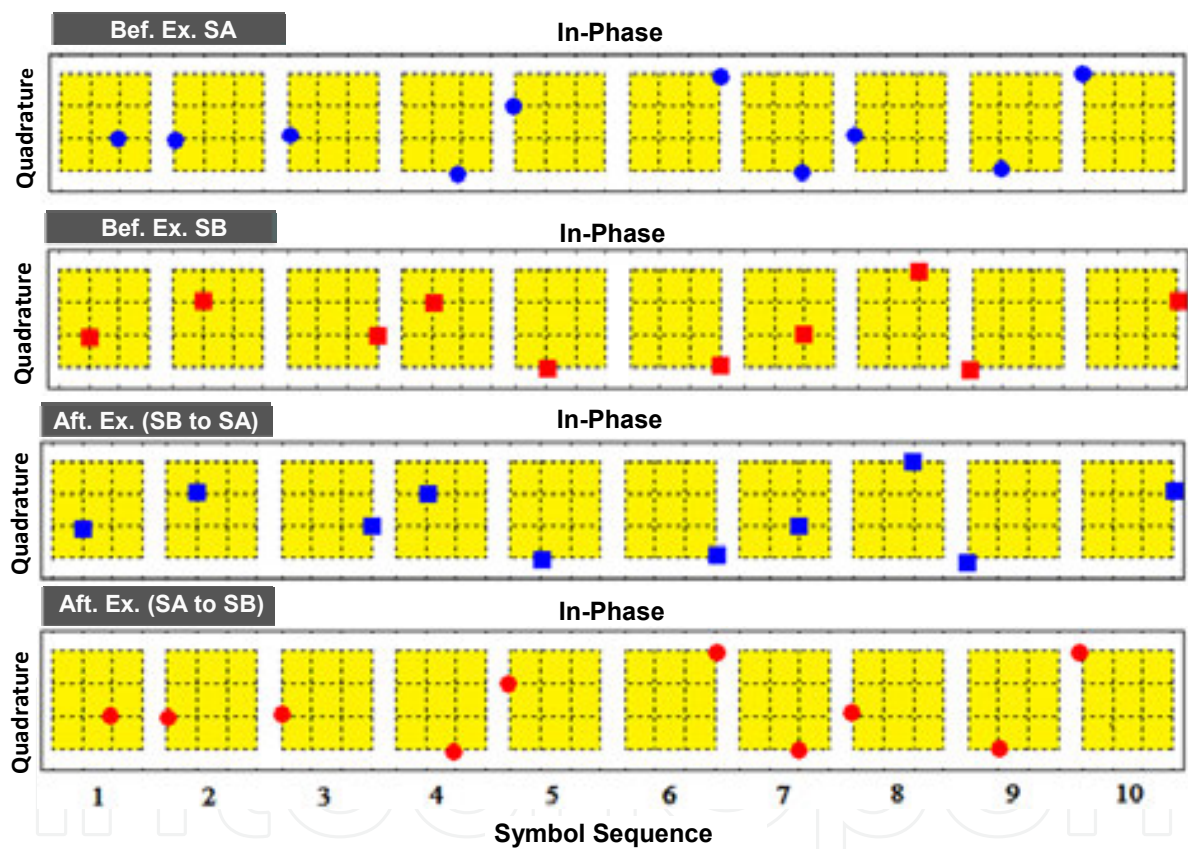


Fig. 21. Simulated symbol sequences for high-base optical data exchange of 640 Gbaud (2.56 Tbit/s) 16-QAM signals.

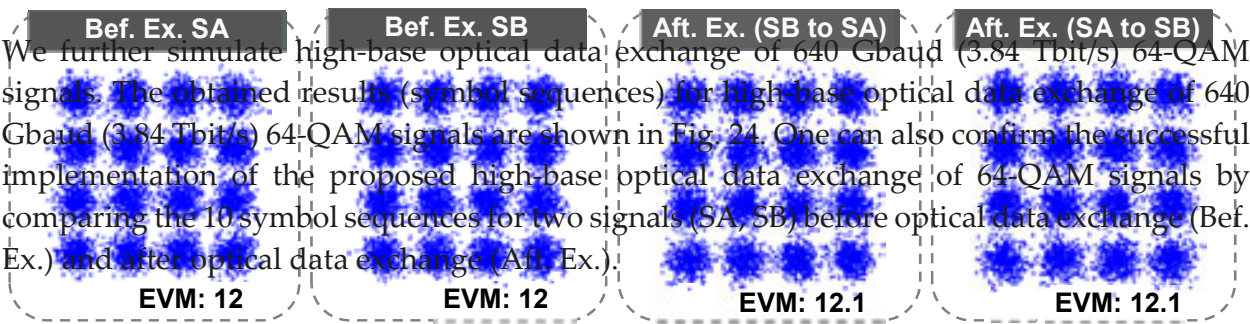


Fig. 22. Simulated constellations of (a)(b) input and (c)(d) output signals for high-base optical data exchange of 640 Gbaud (2.56 Tbit/s) 16-QAM signals.

Figure 19. Measured optical spectrum and balanced eyes for 100-Gbit/s RZ-DQPSK signals after multichannel, multifunctional high-base grooming switch (simultaneous six-channel, high-base optical data exchange between S10 and S23, S11 and S22, S12 and S21; simultaneous two-channel, high-base add/drop for S6 and S7; high-base power equalization for all 23 wavelength channels S1-S23).

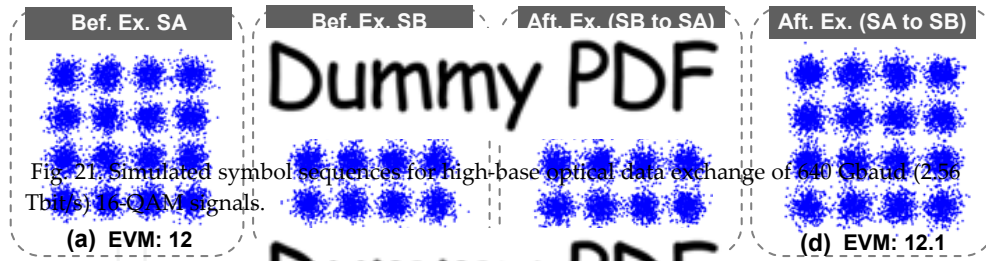


Figure 21. Simulated symbol sequences for high-base optical data exchange of 640 Gbaud (2.56 Tbit/s) 16-QAM signals.

Figure 22. Simulated constellations for high-base optical data exchange of 640 Gbaud (2.56 Tbit/s) 16-QAM signals.

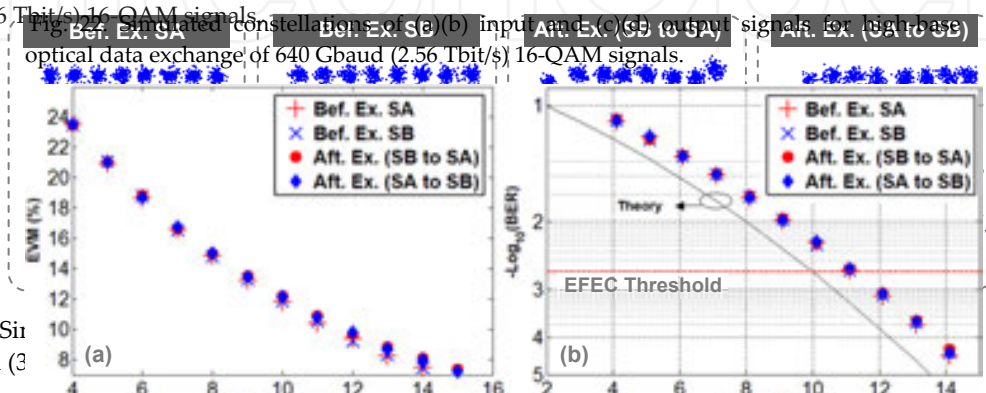


Figure 23. Simulated (a) EVM and (b) BER versus SNR for high-base optical data exchange of 640 Gbaud (2.56 Tbit/s) 16-QAM signals.

Figure 24. Simulated symbol sequences for high-base optical data exchange of 640 Gbaud (3.84 Tbit/s) 64-QAM signals.

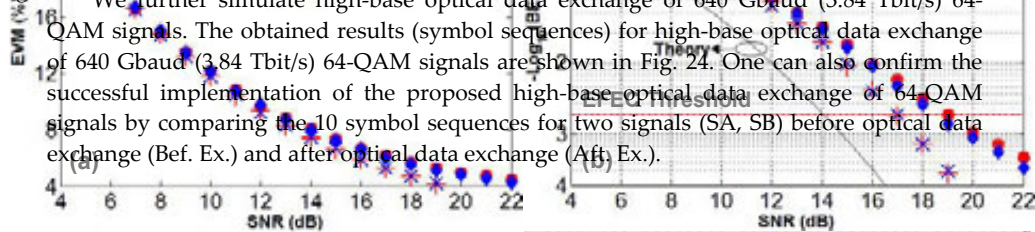


Figure 26. Simulated (a) EVM and (b) BER versus SNR for high-base optical data exchange of 640 Gbaud (3.84 Tbit/s) 64-QAM signals.

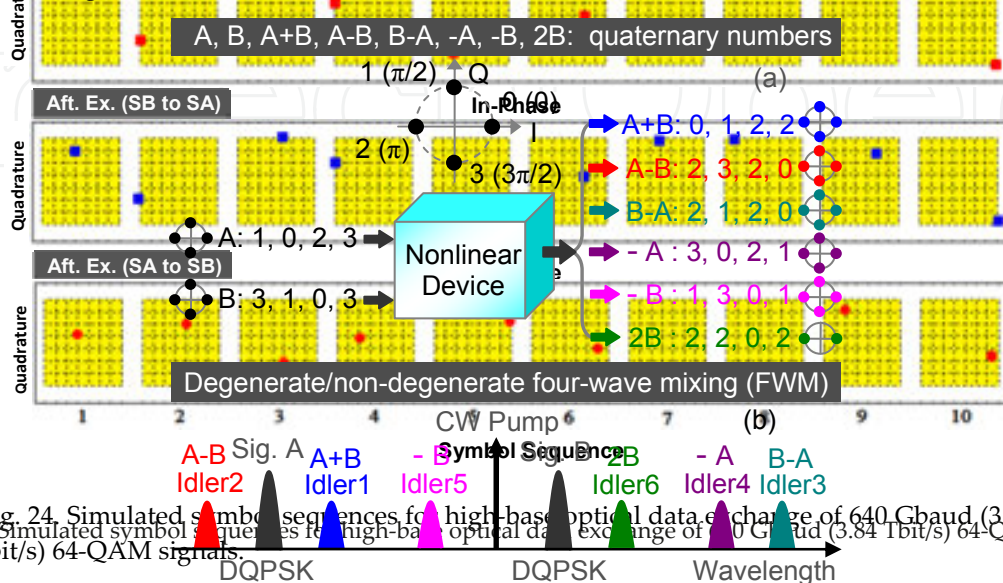


Figure 24. Simulated symbol sequences for high-base optical data exchange of 640 Gbaud (3.84 Tbit/s) 64-QAM signals.

Figure 25 shows simulated constellations for high-base optical data exchange of 64-QAM signals. For an SNR of 14 dB the EVM is also evaluated in Figure 25. The simulated EVM and BER performance versus SNR for high-base optical data exchange of 640 Gbaud (2.56 Tbit/s) 64-QAM signals is shown in Fig. 26(a) and (b). For reference we also plot in Fig. 26(b) the theoretical 64-QAM BER curve. By comparing the simulated BER curves of two signals before and after optical data exchange, one can see that the SNR penalty induced by the high-base optical data exchange operation is assessed to be less than 2 dB at a BER of  $2 \times 10^{-3}$  which is the EFEC threshold.



signalization for all 23 wavelength channels (S1-S23) + he'sim + BER

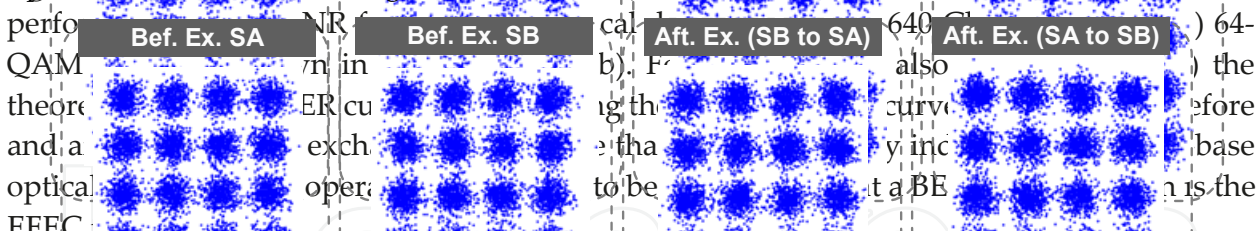


Figure 22. Simulated eye diagrams for 640 Gbaud (2.56 Tb/s) 16-QAM signals (a) EVM: 12 (b) EVM: 12 (c) EVM: 12.1 (d) EVM: 12.1

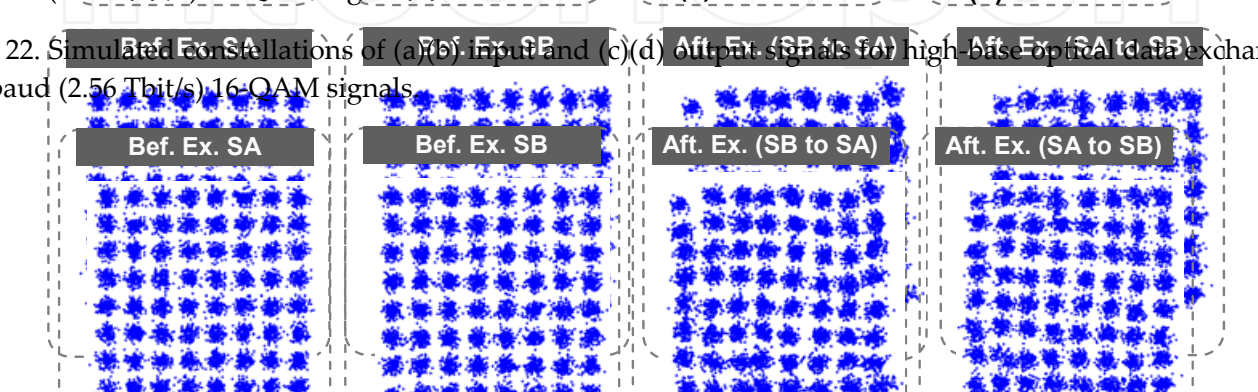


Figure 25. Simulated constellations of (a) (b) (c) (d) output signals for high-base optical data exchange of 640 Gbaud (3.84 Tbit/s) 64-QAM signals. (a) EVM: 7.5 (b) EVM: 7.5 (c) EVM: 8.0 (d) EVM: 8.1

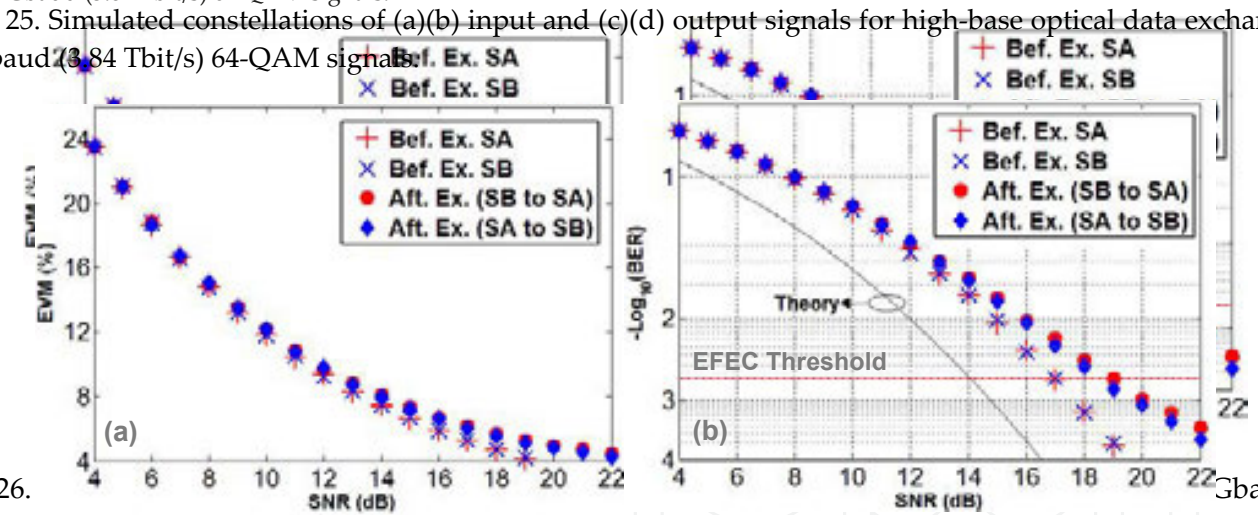
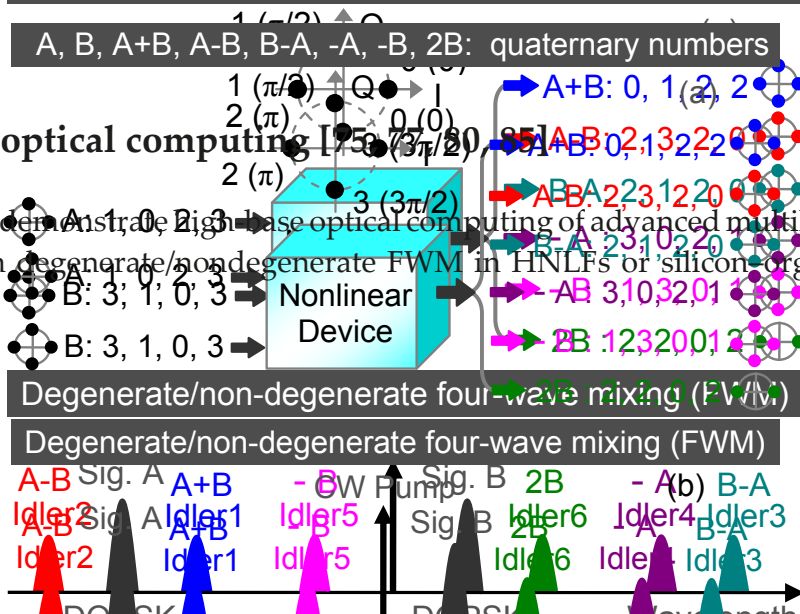


Figure 26. Simulated (a) EVM and (b) BER versus SNR for high-base optical data exchange of 640 Gbaud (3.84 Tbit/s) 64-QAM signals.

#### 4. High-base optical computing

We propose and demonstrate a high-speed optical computing of advanced multilevel modulation signals based on degenerate/nondegenerate FWM in HNLFs or silicon-organic hybrid slot waveguides.



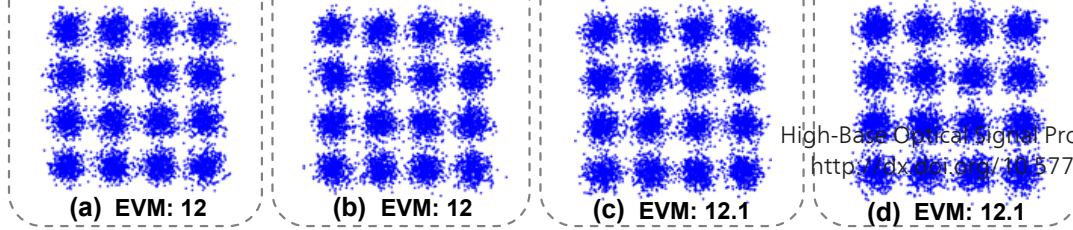


Figure 22. Simulated constellations of (a) input and (b) input and (c) output signals for high-base optical data exchange of 640 Gbaud (3.84 Tbit/s) 16-QAM signals.

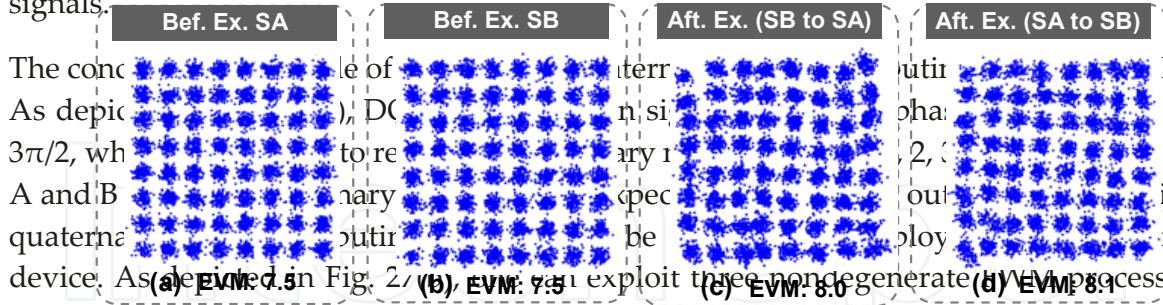


Figure 25. Simulated constellations of (a) input and (b) input and (c) output signals for high-base optical data exchange of 640 Gbaud (3.84 Tbit/s) 64-QAM signals.

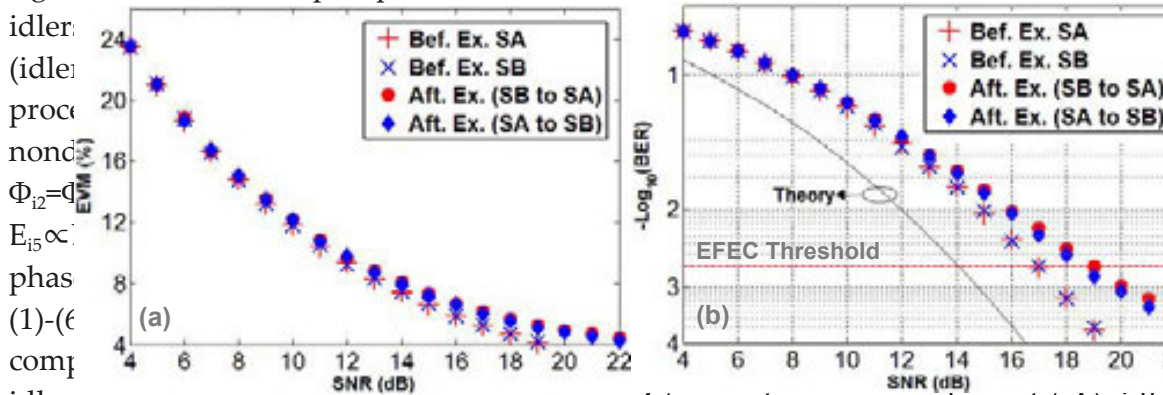


Figure 26. Simulated (a) EVM and (b) BER versus SNR for high-base optical data exchange of 640 Gbaud (3.84 Tbit/s) 64-QAM signals.

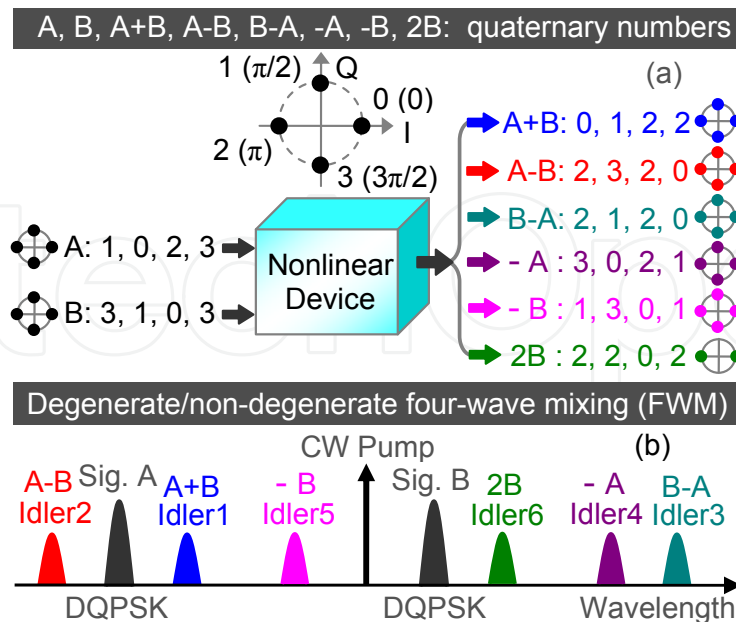


Figure 27. (a) Concept and (b) principle of two-input high-base optical computing (quaternary addition/subtraction/complement/doubling) using a single nonlinear device and DQPSK signals.



Shown in Fig. 28 are measured spectra. One CW pump (1553.2 nm) and two 100-Gbit/s  $2^7$ -1 RZ-DQPSK signals (A: 1546.6 nm, B: 1555.5 nm) are fed into a 460-m-long HNLF. The ZDW, dispersion slope ( $S$ ) and nonlinear coefficient ( $\gamma$ ) of the HNLF are  $\sim 1556$  nm,  $\sim 0.026$  ps/nm<sup>2</sup>/km, and  $20$  W<sup>-1</sup> km<sup>-1</sup>, respectively. The employed HNLF has low and flat dispersion, which benefits simultaneous multiple FWM processes. As a consequence, it is possible to simultaneously generate six idlers (idler 1: 1544.3 nm, idler 2: 1548.9 nm, idler 3: 1562.2 nm, idler 4: 1559.9 nm, idler 5: 1550.9 nm, idler 6: 1557.7 nm) corresponding to simultaneous addition ( $A+B$ ), subtraction ( $A-B$ ,  $B-A$ ), complement ( $-A$ ,  $-B$ ), and doubling ( $2B$ ) of quaternary numbers ( $A$ ,  $B$ ).

Figure 27. (a) Concept and (b) principle of two-input high-base optical computing (quaternary addition/subtraction/complement/doubling) using a single nonlinear device and DQPSK signals.

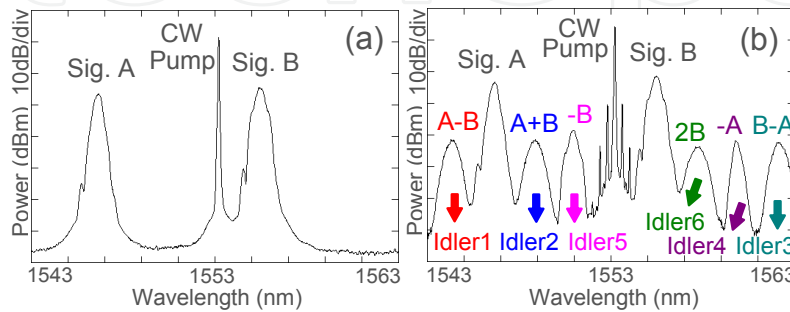


Figure 28. Measured spectra (a) before HNLF and (b) after HNLF for 50-Gbaud two-input quaternary optical computing (addition, subtraction, complement, doubling).

In order to confirm the quaternary optical computing (addition, subtraction, complement, doubling), the waveforms and balanced eyes of the demodulated in-phase (Ch. I) and quadrature (Ch. Q) components of two 100-Gbit/s RZ-DQPSK signals and six converted idlers by multiple FWM processes are recorded. A 50-GHz delay-line interferometer (DLI) is used to demodulate 100-Gbit/s RZ-DQPSK. A relative phase shift is introduced between the two arms of the 50-GHz DLI. Remarkably, quaternary numbers can be represented by the combination of Ch. I and Ch. Q (i.e., 00: '0', 01: '1', 11: '2', 10: '3'). By exploiting multiple degenerate and nondegenerate FWM processes, one can clearly see from Figs. 29 and 30 that simultaneous 50-Gbaud quaternary optical computing of addition ( $A+B$ ), dual-directional subtraction ( $A-B$ ,  $B-A$ ), complement ( $-A$ ,  $-B$ ), and doubling ( $2B$ ) are successfully implemented with 100-Gbit/s DQPSK signals.

The BER performance of the quaternary optical computing is characterized as shown in Fig. 31. The measured power penalty at a BER of  $10^{-9}$  is less than 4 dB for addition ( $A+B$ ), 3 dB for subtraction ( $A-B$ ,  $B-A$ ), 2 dB for complement ( $-A$ ,  $-B$ ), and 3.1 dB for doubling ( $2B$ ), respectively. Remarkably, one can see that the quaternary addition, subtraction, and doubling show relatively large power penalties compared to the quaternary complement. Such interesting phenomenon can be briefly explained as follows. According to the relationships of electrical fields, the distortions of input signals are transferred into converted idlers (i.e., computing results). Actually, the degradations of quaternary addition/subtraction, complement, and doubling are respectively induced by the accumulated distortions from signal A and signal B, distortion from single signal B, and twice distortions from signal B. Additionally, the BER curves of two-output signals from the HNLF are also plotted in Fig. 31(c) and (d) for reference.

Figure 33. Concept and principle of three-input ( $A$ ,  $B$ ,  $C$ ) optical quaternary addition and subtraction ( $A+B-C$ ,  $A+C-B$ ,  $B+C-A$ ,  $A+B+C$ ) using nondegenerate FWM and DQPSK signals.

One can clearly see that the two signals suffer negligible performance degradations during high-base arithmetical operations.

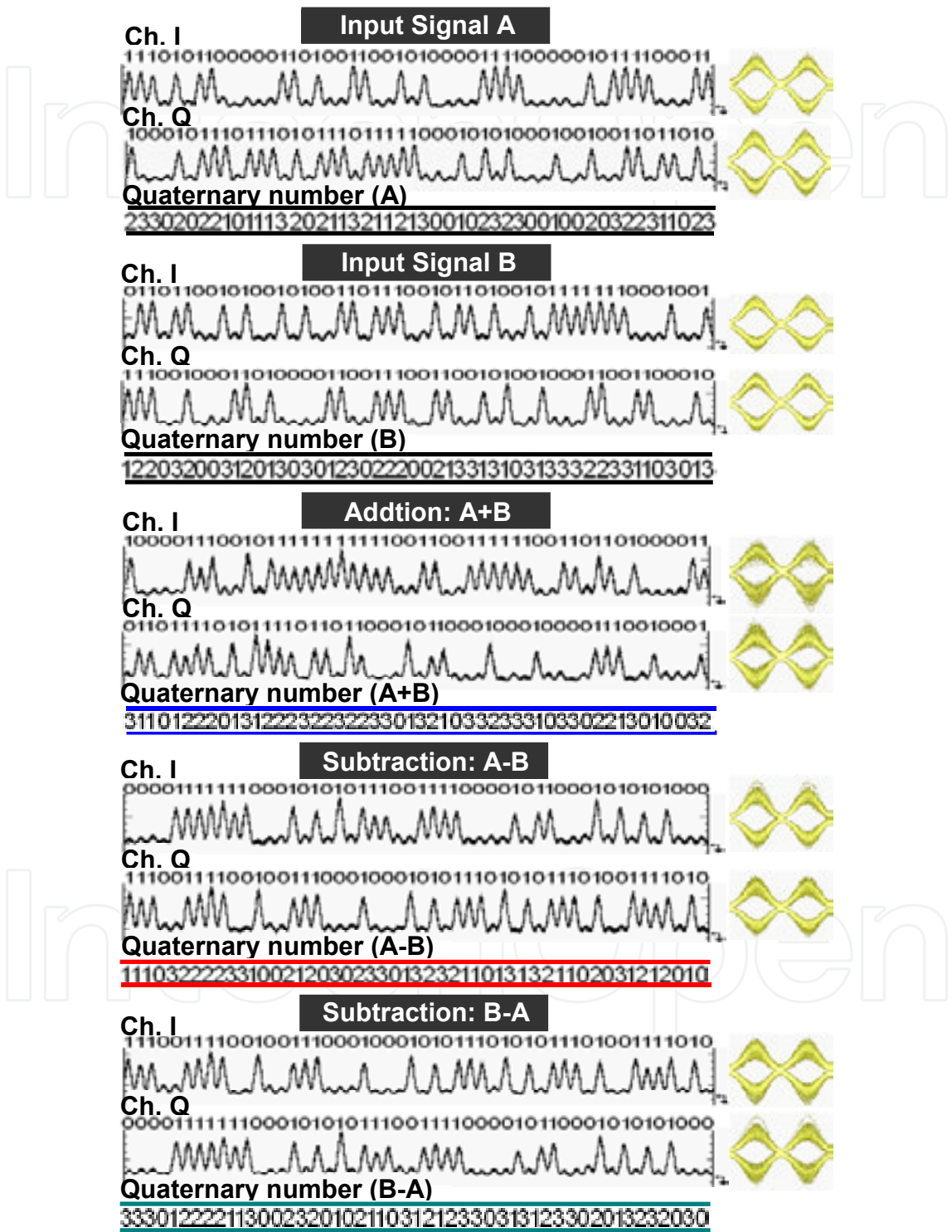


Fig. 29. Demodulated waveforms and balanced eyes for 50-Gbaud two-input quaternary addition and dual-directional subtraction using 100-Gbit/s DQPSK signals.

Shown in Fig. 32 are measured constellations for input/output signals and output computing results. An optical complex spectrum analyzer (APEX AP2440A) is employed in the experiment. One can clearly see from Fig. 32 that the quaternary addition ( $A+B$ ), quaternary subtraction ( $A-B$ ,  $B-A$ ), and quaternary complement ( $-A$ ,  $-B$ ) have four-phase levels ( $0$ ,  $\pi/2$ ,  $\pi$ ,  $3\pi/2$ ) while the quaternary doubling ( $2B$ ) has two-phase levels ( $0$ ,  $\pi$ ).

Shown in Fig. 32 are measured constellations for input/output signals and output computing results. An optical complex spectrum analyzer (APEX AP2440A) is employed in the experiment. One can clearly see from Fig. 32 that the quaternary addition ( $A+B$ ), quaternary subtraction ( $A-B$ ,  $B-A$ ), and quaternary complement ( $-A$ ,  $-B$ ) have four-phase levels ( $0$ ,  $\pi/2$ ,  $\pi$ ,  $3\pi/2$ ) while the quaternary doubling ( $2B$ ) has two-phase levels ( $0$ ,  $\pi$ ).

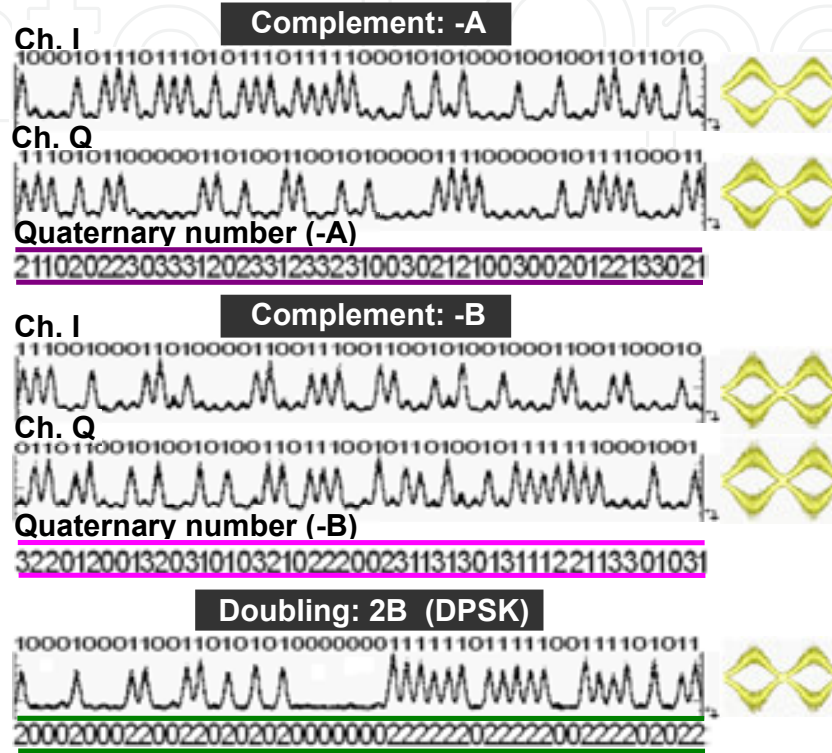


Fig. 30. Demodulated waveforms and balanced eyes for 50-Gbaud quaternary complement and doubling using 100-Gbit/s DQPSK signals.

We then demonstrate high-speed three-input high-base optical computing (addition and subtraction) of quaternary numbers using multiple nondegenerate FWM processes in a single HNLF and DQPSK signals. Figure 33 illustrates the concept and operation principle.

Shown in Fig. 34 are measured spectra for 50-Gbaud three-input quaternary optical computing (addition, subtraction). Figure 34(a) depicts the spectrum for degenerate FWM, which enables the conversion from  $C$  to  $-C$  (i.e., quaternary complement). In the experiment, the wavelengths of CW pump, input signal  $C$  (Sig. C) and converted signal ( $-Sig. C$ ) are 1552.0, 1548.7, and 1555.5 nm, respectively. Figure 34(b) shows the typical spectrum for three-input quaternary optical computing, i.e., quaternary hybrid addition and subtraction ( $A+B-C$ ,  $A+C-B$ ,  $B+C-A$ ). In the experiment, the wavelengths of three input 100-Gbit/s RZ-DQPSK signals ( $A$ ,  $B$ ,  $C$ ) are 1546.6 (Sig. A), 1553.2 (Sig. B), and 1555.5 nm (Sig. C), respectively. It is clearly shown that three converted idlers, i.e., idler 1 at 1544.3 nm, idler 2 at 1548.9 nm, and idler 3 at 1562.2 nm, are generated by three nondegenerate FWM processes. Actually, idler 1, idler 2, and idler 3 correspond to  $A+B-C$ ,  $A+C-B$ , and  $B+C-A$ , respectively. Figure 34(c) displays the spectrum for



Fig. 30. Demodulated waveforms and balanced eyes for 50-Gbaud quaternary complement and doubling using 100-Gbit/s DQPSK signals. High-Base Optical Signal Processing 53  
http://dx.doi.org/10.5772/61504

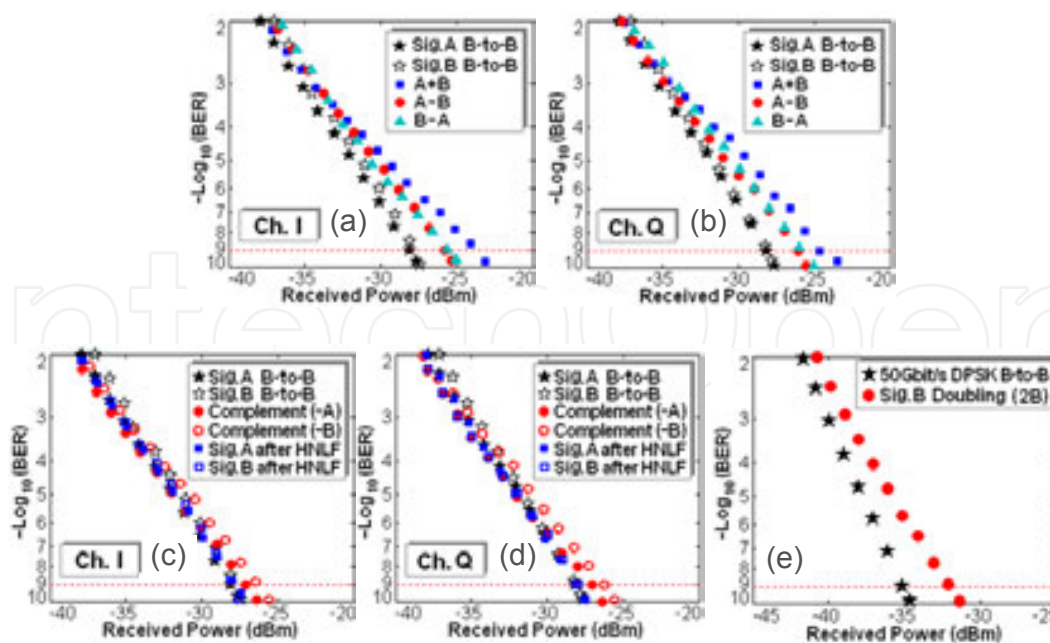


Fig. 31. Measured BER curves for input/output signals (A, B), quaternary addition (A+B), dual-directional subtraction (A-B, B-A), complement (-A, -B), and doubling (2B).

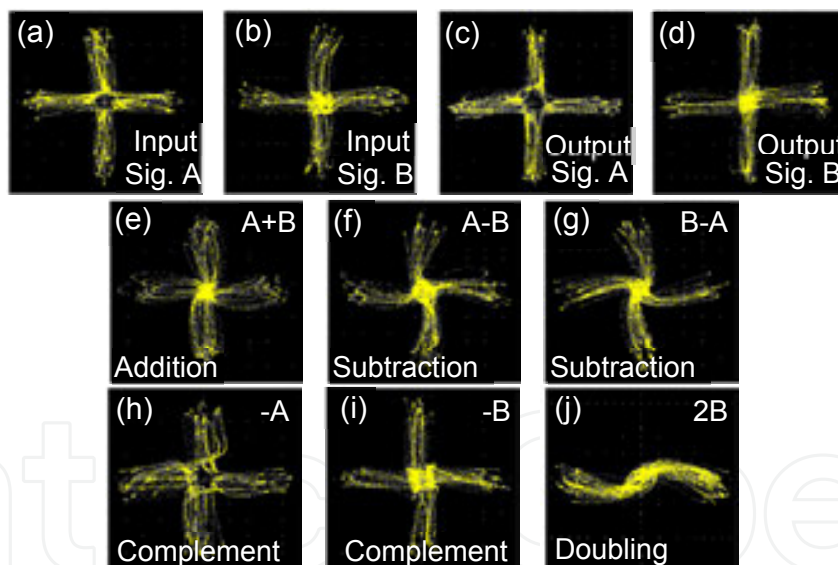
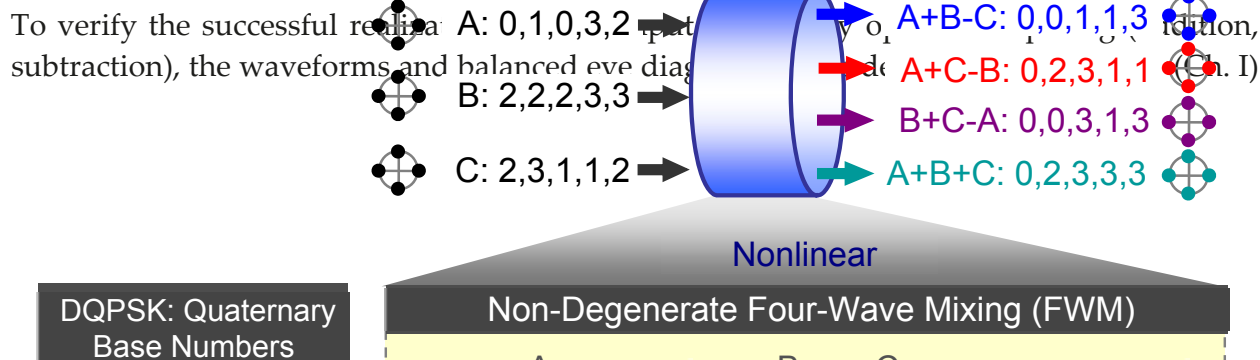


Fig. 32. Measured constellations for 50-Gbaud two-input quaternary optical computing (addition, dual-directional subtraction, complement, doubling) with 100-Gbit/s DQPSK signals.

three-input quaternary addition of A+B+C. In the experiment, the converted signal (-Sig. C) by degenerate FWM shown in Fig. 34(a) is selected and used as the input signal shown in Fig. 34(b), i.e., -Sig. C is employed instead of Sig. C as shown in Fig. 34(c). After the nondegenerate FWM process, the converted idler 1 carrying quaternary addition result of A+B+C is obtained.



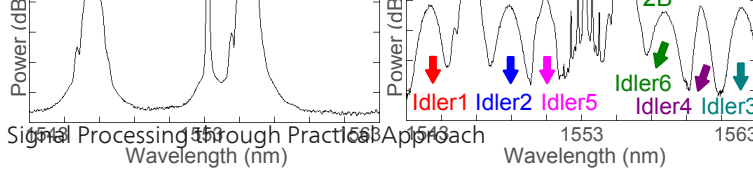


Figure 28. Measured spectra (a) before HNLf and (b) after HNLf for 50-Gbaud two-input quaternary optical computing (addition, subtraction, complement, doubling).

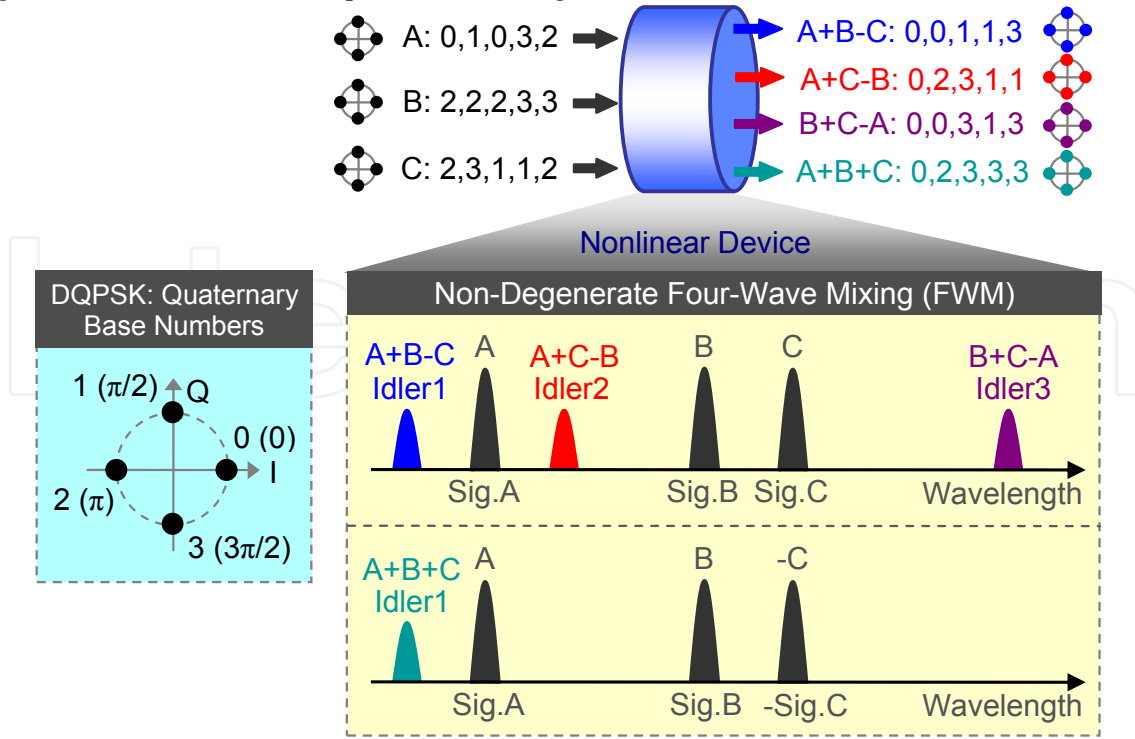


Figure 33. Concept and principle of three-input (A, B, C) optical quaternary addition and subtraction (A+B-C, A+C-B, B+C-A, A+B+C) using nondegenerate FWM and DQPSK signals.

and quadrature (Ch. Q) components of three-input 100-Gbit/s RZ-DQPSK signals and three-output converted idlers by nondegenerate FWM processes are recorded. Figure 35 depicts the measured sequences of input signals and converted idlers. It is clearly shown that the degenerate FWM process enables 50-Gbaud conversion from C to  $-C$  (i.e., quaternary complement) and three nondegenerate FWM processes perform three-input quaternary optical computing, i.e., hybrid quaternary addition and subtraction (A+B-C, A+C-B, B+C-A, A+B+C).

We measure the BER curves as shown in Fig. 36 for 50-Gbaud three-input quaternary optical computing (A+B-C, A+C-B, B+C-A). It is shown from Figs. 36(a) and (b) that the power penalties at a BER of  $10^{-9}$  of three-input quaternary optical computing (A+B-C, A+C-B, B+C-A) are measured to be less than 6 dB. Shown in Fig. 37 are the measured BER curves for 50-Gbaud conversion from C to  $-C$  (i.e., quaternary complement) and 50-Gbaud three-input quaternary addition (A+B+C). The observed power penalty is negligible for the conversion from C to  $-C$ . For the quaternary addition of A+B+C, the power penalty at a BER of  $10^{-9}$  is assessed to be less than 6 dB. Similar to two-input quaternary optical computing, it is believed that the performance degradations of three-input quaternary optical computing (i.e., quaternary hybrid addition and subtraction of A+B-C, A+C-B, B+C-A, and A+B+C) are mainly caused by accumulated distortions originated from three-input signals (A, B, C or  $-C$ ). Such phenomenon can be explained according to the electrical field and linear optical phase relationships of nondegenerate FWM processes. Shown in Fig. 36(c)(d) and Fig. 37(a)(b) are measured BER curves for three output signals (A, B, C or  $-C$ ) from HNLf after three-input quaternary optical

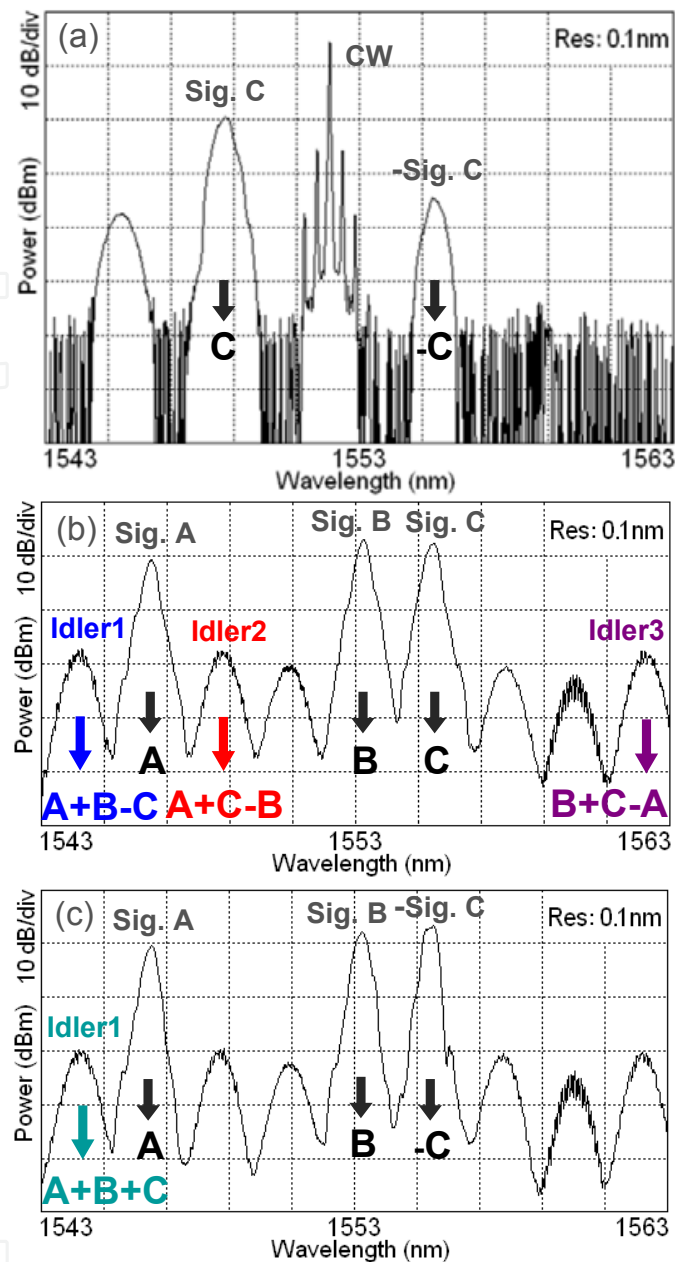


Figure 34. Measured spectra for 50-Gbaud three-input quaternary optical computing (addition, subtraction). (a) Degenerate FWM process (C to +C conversion); (b) three-input quaternary hybrid addition and subtraction (idler 1:  $A+B-C$ , idler 2:  $A+C-B$ , idler 3:  $B+C-A$ ) by degenerate FWM process; (c) three-input quaternary addition (idler:  $A+B+C$ ) by degenerate FWM process.

computing. For the three signals during the three-input quaternary optical computing operations, no significant performance degradations are observed in the experiment.

We also measure the constellation diagrams for three-input/output 100-Gbit/s RZ-DQPSK signals (A, B, C/-C) and six converted idlers corresponding to quaternary hybrid addition and subtraction of  $A+B-C$ ,  $A+C-B$ ,  $B+C-A$ , and  $A+B+C$ . An optical complex spectrum analyzer (APEX AP2440A) is employed in the experiment. From Fig. 38 one can clearly observe four-



phase levels (i.e.,  $0$ ,  $\pi/2$ ,  $\pi$ ,  $3\pi/2$ ) of all input/output signal and output idlers. These four-phase levels can represent quaternary base numbers.

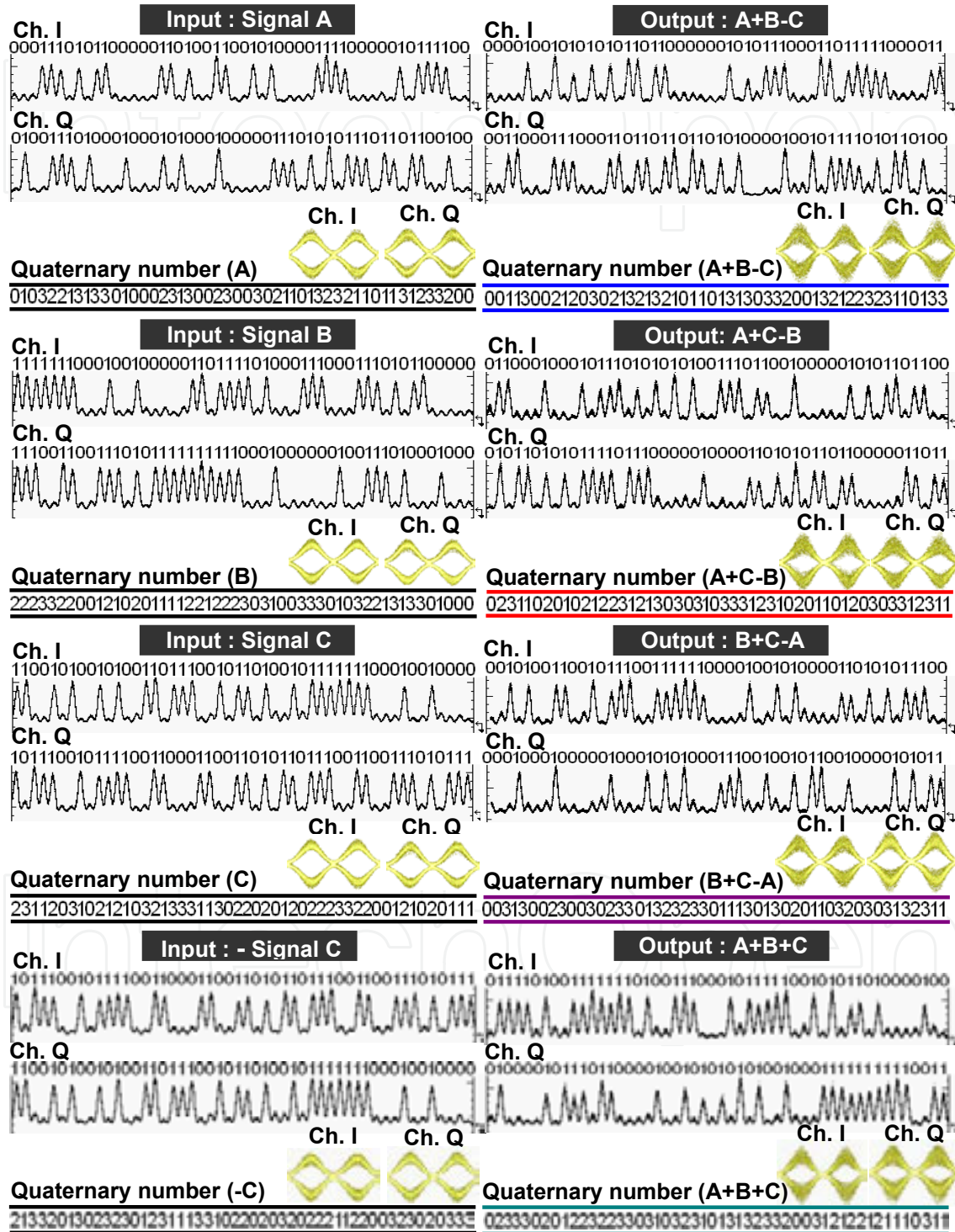


Figure 35. Demodulated temporal waveforms and balanced eye diagrams for 50-Gbaud three-input (A, B, C) quaternary addition and subtraction (A+B-C, A+C-B, B+C-A, A+B+C) for 50-Gbaud three-input (A, B, C) quaternary addition and subtraction (A+B-C, A+C-B, B+C-A, A+B+C).

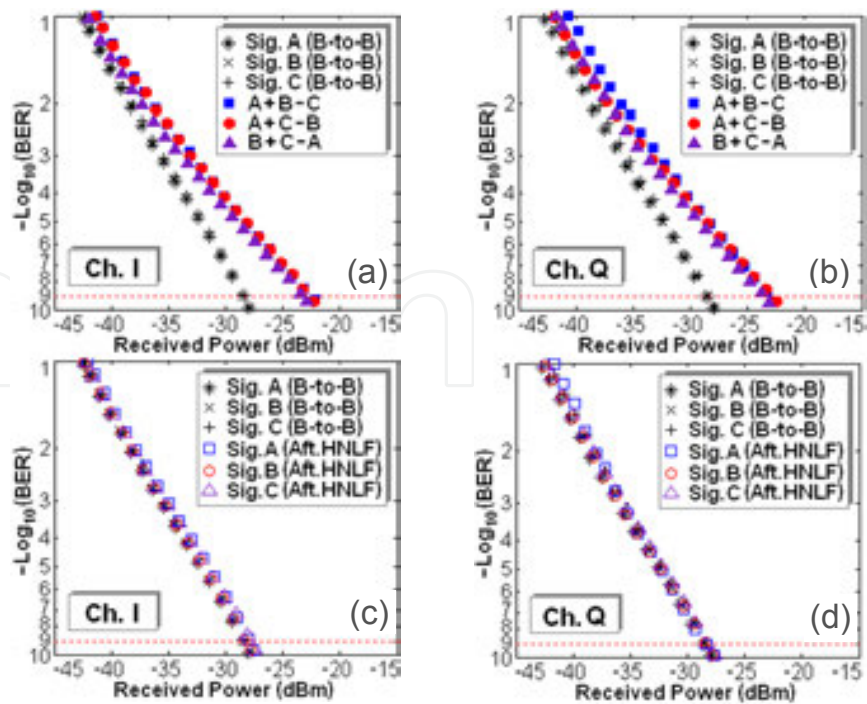


Figure 36. Measured BER curves for 50-Gbaud three-input quaternary optical computing. (a)(b) Hybrid addition and subtraction of A+B-C, A+C-B, and B+C-A. (c)(d) Output signals (Sig. A, Sig. B, Sig. C) from HNLF. (a)(c) Ch. I. (b)(d) Ch. Q. B-to-B: back-to-back.

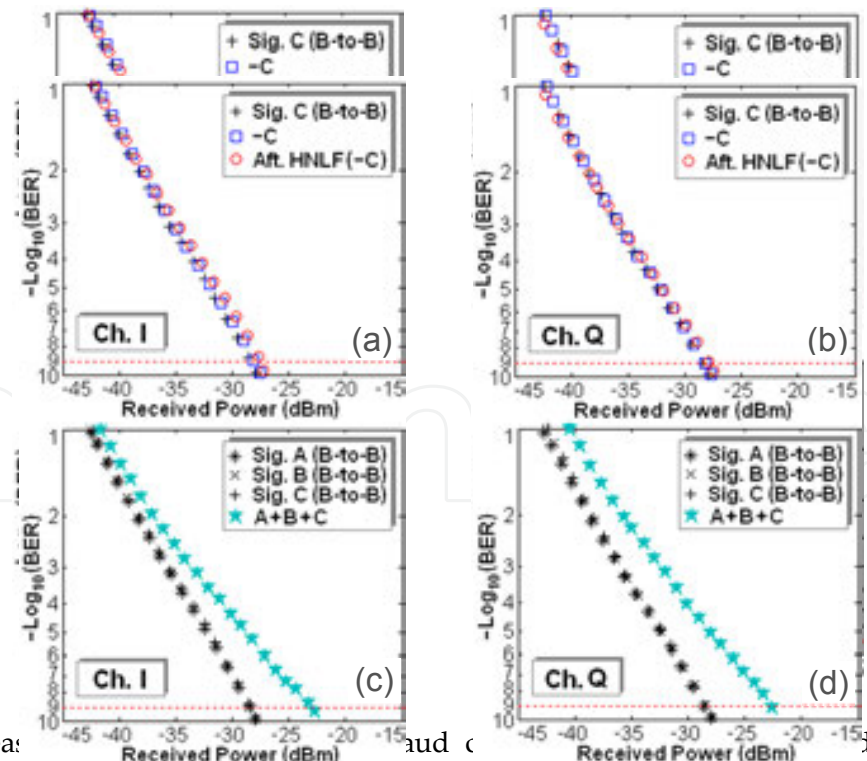
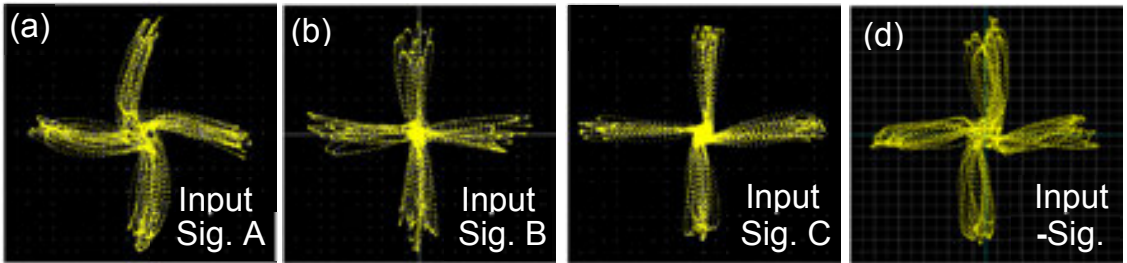


Figure 37. Measured BER curves for 50-Gbaud conversion from C to -C and three-input quaternary addition of A+B+C. (a)(b) Conversion from C to -C. (c)(d) A+B+C. (a)(c) Ch. I. (b)(d) Ch. Q. B-to-B: back-to-back.



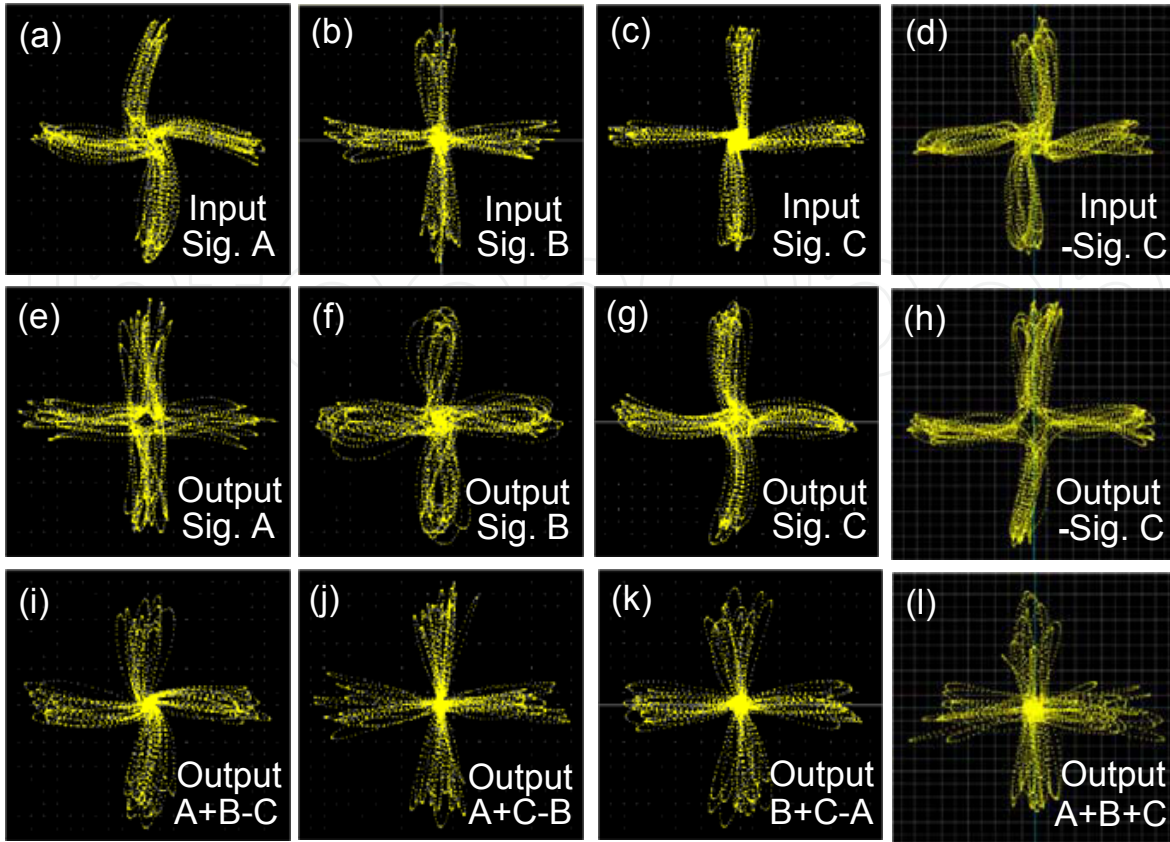


Figure 38. Measured constellation diagrams for 50-Gbaud three-input quaternary addition and subtraction.  
**Figure 38.** Measured constellation diagrams for 50-Gbaud three-input quaternary addition and subtraction.

In addition to two-/three-input high-base optical computing based on degenerate/nondegenerate FWM in HNLFs, we also propose and simulate three-input high-base optical computing (hexadecimal addition and subtraction) in a single silicon–organic hybrid slot waveguide based on nondegenerate FWM processes.

Shown in Fig. 39(a) is the schematic 3D structure of the proposed silicon–organic hybrid slot waveguide. It has a sandwich structure formed by a low-refractive-index PTS [polymer poly (bis para-toluene sulfonate) of 2, 4-hexadiyne-1,6 diol] layer inserted between two high-refractive-index silicon layers. The cladding of the structure is air. The substrate is silicon dioxide. In the designed silicon–organic hybrid slot waveguide, the waveguide width is  $W=250$  nm, the upper silicon height is  $H_u=180$  nm, the lower silicon height is  $H_l=180$  nm, and the slot height is  $H_s=25$  nm. We plot in Fig. 39(b)–(d) the quasi-TM mode distribution together with its normalized power density along  $x$  and  $y$  directions. It is clearly shown that the mode is highly confined in the nanoscale nonlinear organic slot region (i.e., tight light confinement). As a consequence, high nonlinearity and instantaneous Kerr response are achievable without impairments by TPA and FCA. Using finite-element method, we assess the effective mode area and nonlinearity to be  $7.7 \times 10^{-14} \text{ m}^2$  and  $5500 \text{ w}^{-1}\text{m}^{-1}$ , which can potentially facilitate efficient high-base optical signal processing (e.g., hexadecimal addition/subtraction). Figure 40 illustrates the operation principle which is similar to that in HNLFs. Instead of using DQPSK



for quaternary optical computing, here 16PSK signals are used to achieve hexadecimal optical computing.

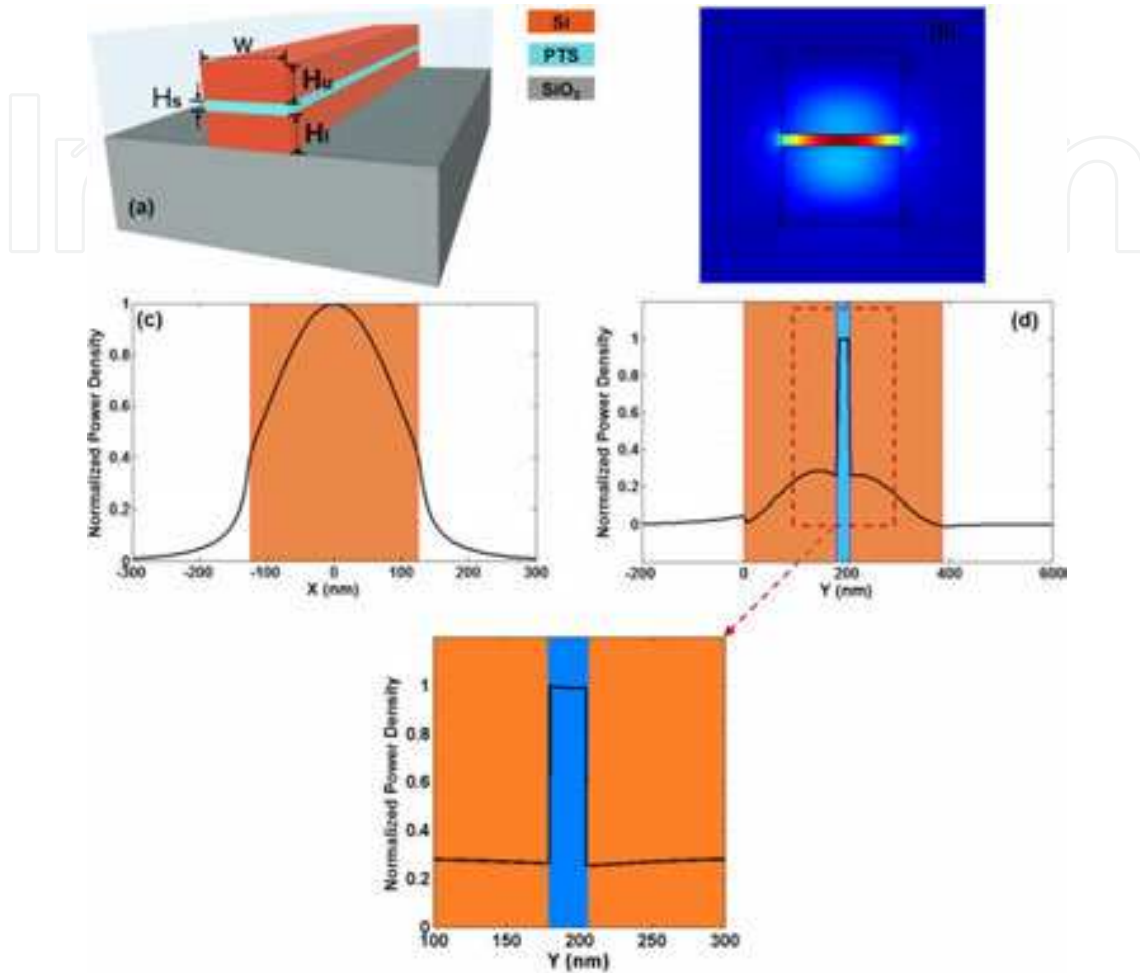


**Figure 39.** (a) 3D structure, (b) mode distribution, (c)(d) normalized power density along x and y directions of a silicon-organic hybrid slot waveguide.

In the following simulations, three 40-Gbaud  $2^{13}-1$  PRBS 16-PSK signals ( $\lambda_A$ : 1546 nm,  $\lambda_B$ : 1552 nm,  $\lambda_C$ : 1550 nm) are adopted. A 1-mm-long silicon-organic hybrid slot waveguide is employed. Figure 41 shows simulation results for three-input 40-Gbaud (160-Gbit/s) hexadecimal addition/subtraction. Twenty-symbol sequences are plotted in Fig. 41, which confirms the successful implementation of three-input hexadecimal addition/subtraction ( $A+B-C$ ,  $A+C-B$ ,  $B+C-A$ ,  $A+B+C$ ,  $A-B-C$ ,  $B-A-C$ ). The constellations are also shown in Fig. 42 with assessed EVM under an OSNR of 28 dB for input signals. The observed degradation of EVM for hexadecimal addition/subtraction can be ascribed to the accumulated noise from input 16-PSK signals and impairments from nonlinear interactions inside the silicon-organic hybrid slot waveguide. We further investigate the EVM of input signals and output idlers against the OSNR of input signals as shown in Fig. 43(a) and (b). The EVM penalties are assessed to be less than 4.5 for hexadecimal addition/subtraction under an OSNR of 28 dB.

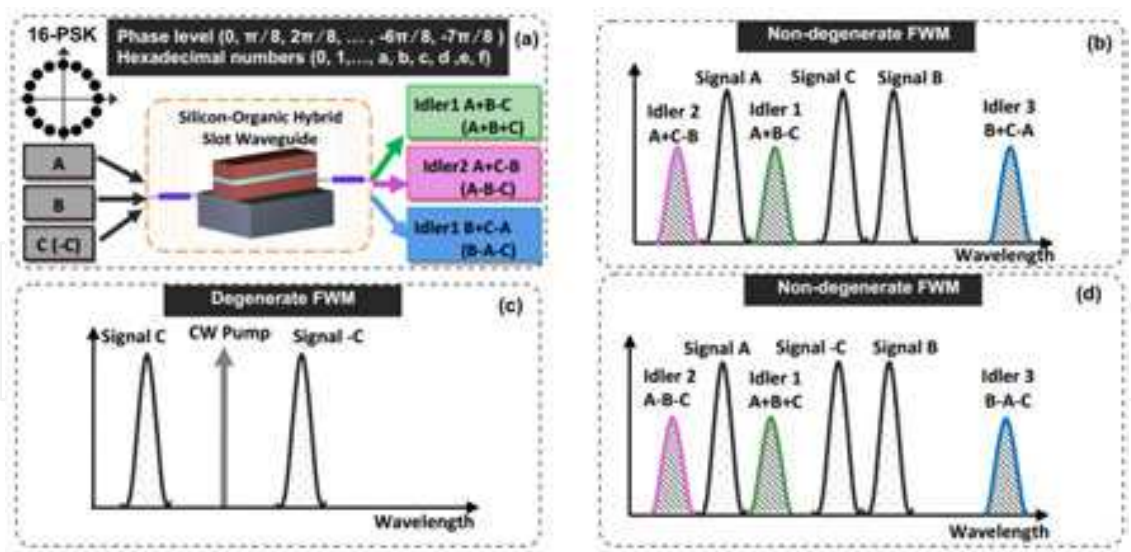


Figure 40. (a) Concept and (b)(c)(d) operation principle of three-input hexadecimal addition/subtraction.

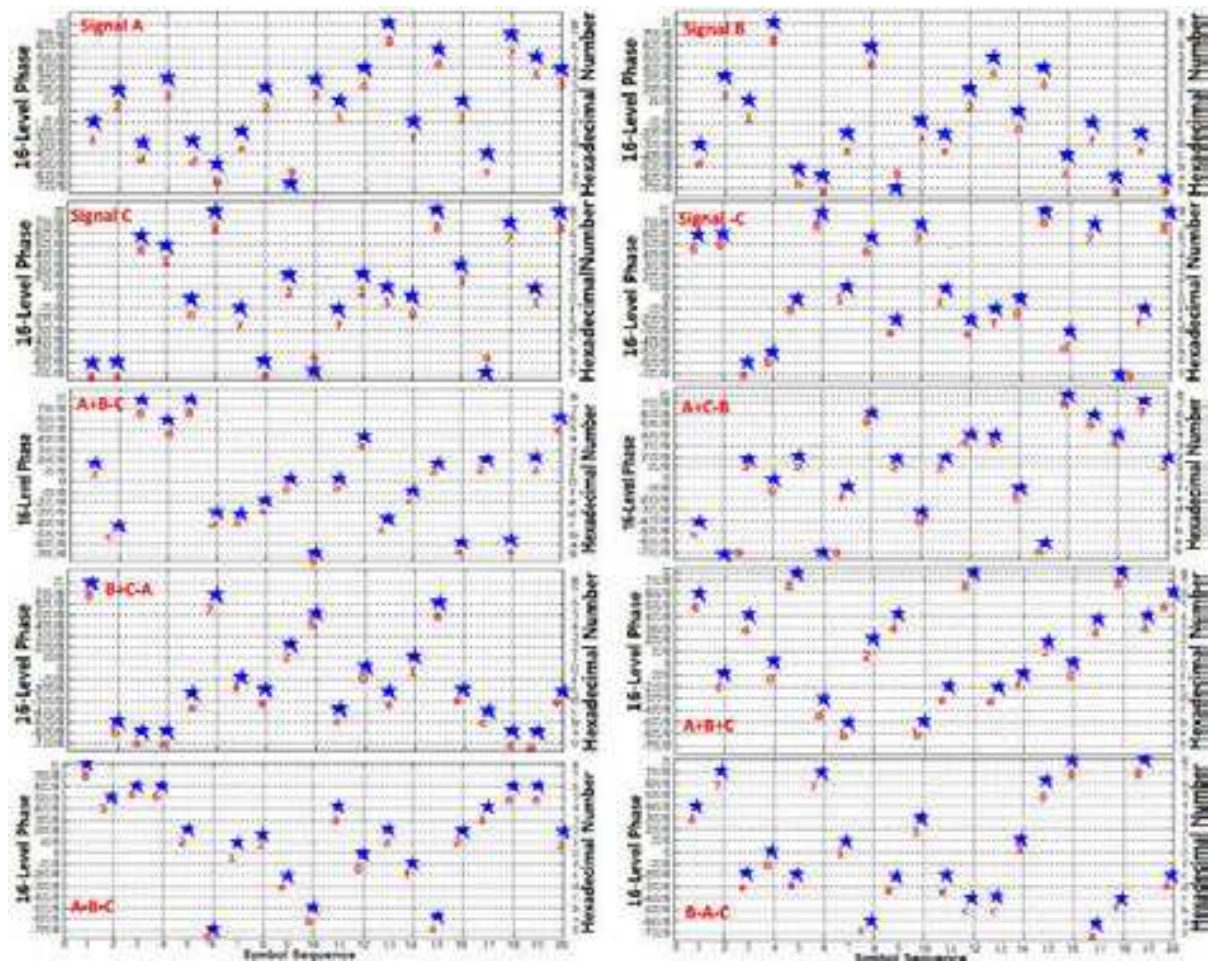
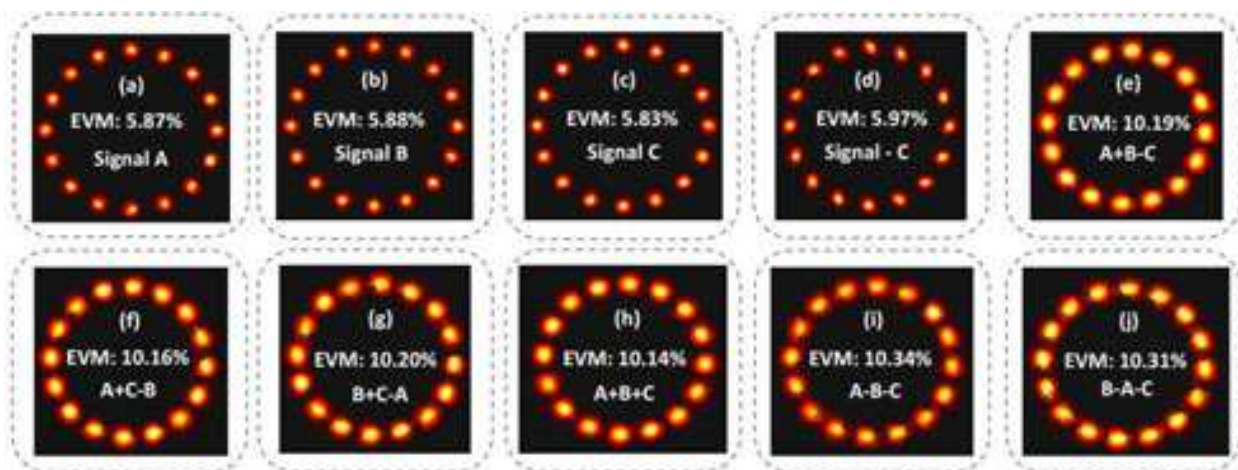
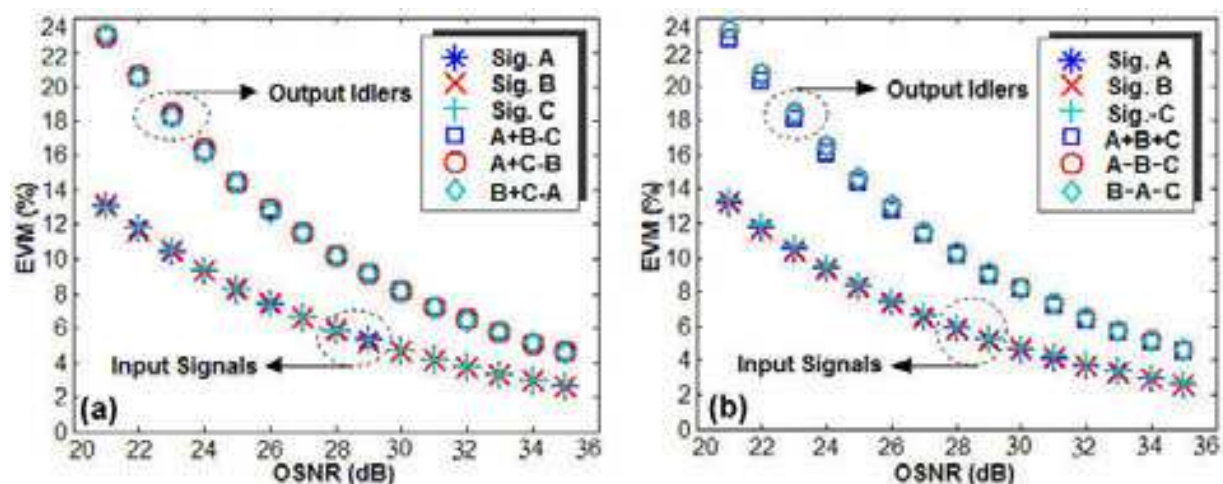


Figure 41. Simulated symbol sequence for three-input 40-Gbaud (160-Gbit/s) hexadecimal addition/subtraction using silicon-organic hybrid slot waveguide.





**Figure 42.** Simulated constellations for three-input 40-Gbaud (160-Gbit/s) hexadecimal addition/subtraction using silicon-organic hybrid slot waveguide.



**Figure 43.** Simulated EVM vs. OSNR for 40-Gbaud (160-Gbit/s) hexadecimal addition/subtraction using silicon-organic hybrid slot waveguide.

## 5. High-base coding/decoding [79]

We propose and demonstrate high-base optical coding/decoding of advanced multilevel modulation signals based on degenerate FWM in HNLFs.

Figure 44 illustrates the concept and principle of the proposed symbol-wise hexadecimal coding/decoding using degenerate FWM and 16-QAM signals. Symbol-wise hexadecimal coding/decoding can be regarded as the constellation manipulation in the I/Q plane. The pump, original signal, coded signal and decoded signal are denoted by  $K_i$ ,  $P_i$ ,  $C_i$ , and  $D_i$ , respectively. In the symbol-wise hexadecimal coding/decoding the pump can be CW or phase



modulated. Illustrated in Fig. 44(a1) and (b1) are the symbol-wise hexadecimal coding, in which a CW or phase-modulated pump (Ki) and a 16-QAM signal (Pi) are launched into a nonlinear device such as HNLF to take part in the nonlinear interaction such as degenerate FWM process. 16-QAM signal can represent a hexadecimal number. When propagating along the HNLF, the degenerate FWM process generates a coded signal (Ci). Note that the electrical field ( $E_{Ci}$ ) of the coded signal (Ci) satisfies the relationship of  $E_{Ci} \propto E_{Ki}^2 \cdot E_{Pi}^*$ . From the electrical fields a linear phase relationship of  $\Phi_{Ci} = 2\Phi_{Ki} - \Phi_{Pi}$  is achieved, i.e., twice the pump phase modulation ( $2\Phi_{Ki}$ ) and the conjugated phase of the original signal ( $-\Phi_{Pi}$ ) contribute together to the phase of the coded signal. Consequently, the coding algorithm simultaneously relies on the pump phase modulation and degenerate-FWM-induced phase conjugation. For the CW pump-assisted symbol-wise hexadecimal coding as shown in Fig. 44(a1), all constellation points in the I/Q plane are moved to their symmetrical positions with respect to the I-axis because of the phase conjugation property of degenerate FWM. Actually, hexadecimal code conversion from one number to another is achieved simply by conjugated degenerate FWM process. For the symbol-wise hexadecimal coding exploiting a phase-modulated pump, i.e.  $(0, \pi/4)$  phase modulation, as illustrated in Fig. 44(b1), all constellation points are mapped symmetrically with respect to the I-axis. Meanwhile, the pump phase modulation also introduces additional symbol-varying coding. When the constellation point of 16-QAM in one symbol meets the  $\pi/4$  pump phase modulation, it will rotate in a counter-clockwise direction by  $\pi/2$ . As a result, the coding algorithm becomes  $\Phi_{Ci} = 2\Phi_{Ki} - \Phi_{Pi}$  which determines the rule of hexadecimal coding.

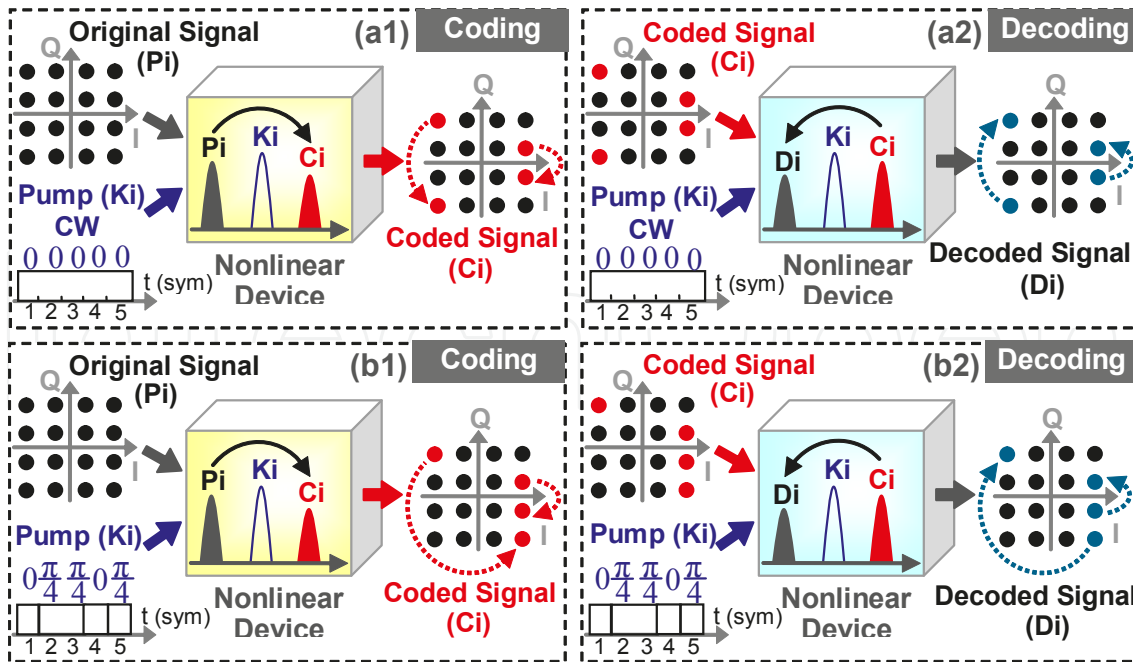


**Figure 44.** Concept and operation principle of variable symbol-wise hexadecimal coding/decoding by use of optical nonlinearity and 16-QAM. (a1)(a2) Symbol-wise hexadecimal coding/decoding assisted by CW pump; (b1)(b2) symbol-wise hexadecimal coding/decoding assisted by  $(0, \pi/4)$  phase-modulated pump; (a1)(b1) Coding; (a2)(b2) Decoding.

Figure 44(a2) and (b2) illustrate the symbol-wise hexadecimal decoding. The pump (Ki) and the coded signal (Ci) are fed into another nonlinear device such as HNLF to participate in the nonlinear interaction such as degenerate FWM process which generates the decoded signal (Di). It is noted that the electrical field of the decoded signal (Di) satisfies the relationship of  $E_{Di} \propto E_{Ki}^2 \cdot E_{Ci}^* \propto E_{Ki}^2 \cdot E_{Ki}^{*2} \cdot E_{Pi} = |E_{Ki}|^4 \cdot E_{Pi} \propto E_{Pi}$ . Thus, the phase of the decoded signal (Di) meets the relationship of  $\Phi_{Di} = 2\Phi_{Ki} - \Phi_{Ci} = 2\Phi_{Ki} - (2\Phi_{Ki} - \Phi_{Pi}) = \Phi_{Pi}$ . As a consequence, the decoded signal (Di) recovers the original signal (Pi) after the decoding process. The decoding algorithm is determined by  $\Phi_{Di} = 2\Phi_{Ki} - \Phi_{Ci} = 2\Phi_{Ki} - (2\Phi_{Ki} - \Phi_{Pi}) = \Phi_{Pi}$ . Remarkably, the decoding algorithm corresponds to the constellation manipulation in the complex plane. The concept and principle shown in Fig. 44 indicate that the constellation of a 16-QAM signal can be manipulated by employing optical nonlinearity, which enables the symbol-wise hexadecimal coding/decoding. Moreover, exploiting a CW or (0,  $\pi/4$ ) phase-modulated pump can facilitate optical variable symbol-wise hexadecimal coding/decoding assisted by optical nonlinearity.

Shown in Fig. 45 is the experimental setup for the proposed optical symbol-wise hexadecimal coding/decoding. A 10-Gbaud (40-Gbit/s) 16-QAM signal is prepared via the vector addition of two copies of QPSK signal using an I/Q QPSK modulator, polarization controllers (PCs), a tunable differential group delay (DGD) element, and a polarizer (Pol.). A 10-Gbit/s phase-modulated pump with (0,  $\pi/4$ ) binary phase modulation, which is synchronized with the 10-Gbaud 16-QAM signal, is provided by employing a phase modulator (PM) driven by PRBS patterns. Note that the PM is not utilized for the CW pump-assisted hexadecimal coding/decoding. For the hexadecimal coding process, the 16-QAM signal (Pi) and the CW/phase-modulated pump (Ki) are launched into a 460-m piece of HNLF. The ZDW, dispersion slope (S) and nonlinear coefficient ( $\gamma$ ) of the HNLF employed in the experiment are  $\sim 1556$  nm,  $\sim 0.026$  ps/nm<sup>2</sup>/km, and  $20 \text{ W}^{-1}\text{km}^{-1}$ , respectively. When the 16-QAM signal (Pi) and the CW/phase-modulated pump (Ki) propagate along the HNLF, a coded signal (Ci) is generated by degenerate FWM process. The coded signal (Ci) takes the result of hexadecimal coding. For the hexadecimal decoding process, the coded signal (Ci) and the CW/phase-modulated pump (Ki) are fed into another 520-m piece of HNLF which has a ZDW of  $\sim 1555$  nm, S of  $\sim 0.026$  ps/nm<sup>2</sup>/km, and  $\gamma$  of  $20 \text{ W}^{-1}\text{km}^{-1}$ . When the coded signal (Ci) and the CW/phase-modulated pump transmit through the HNLF, a decoded signal (Di) is obtained by degenerate FWM process. The decoded signal (Di) recovers the original signal corresponding to hexadecimal decoding. In the experimental setup, BPFs at the output of HNLFs are employed to suppress unwanted frequency components and pick up coded/decoded signals. For coherent detection of 16-QAM signals, an optical modulation analyzer (Agilent N4391A) and a digital phosphor oscilloscope (Tektronix DPO72004) with a 50-Gs/s sample rate and a 20-GHz electrical bandwidth are employed in the experiment.

The measured spectra for optical variable symbol-wise hexadecimal coding/decoding are shown in Fig. 46. Both, CW pump and (0,  $\pi/4$ ) phase-modulated pump are employed in the experiment. The original signal (Pi), pump (Ki), coded signal (Ci), and decoded signal (Di) have wavelengths of 1557.0, 1555.6, 1554.2, and 1557.0 nm, respectively. We set the power of the original signal for coding and the coded signal for decoding to be around 10.8 dBm. For

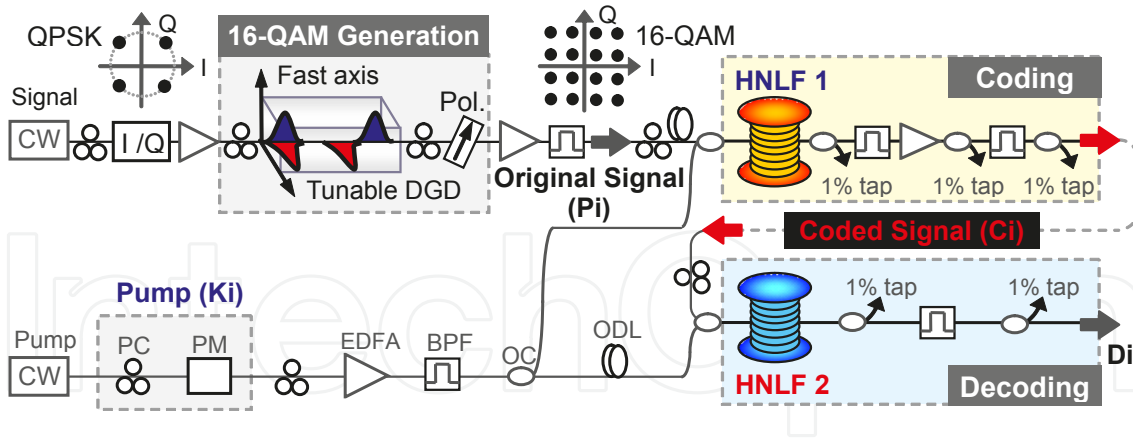


**Figure 45.** Experimental setup for high-base coding/decoding. Degenerate FWM in HNLF, 16-QAM signal and CW/phase-modulated pumps are employed to enable symbol-wise hexadecimal coding/decoding. QPSK: quadrature phase-shift keying; QAM: quadrature amplitude modulation; HNLF: highly nonlinear fiber; CW: continuous-wave; PC: polarization controller; EDFA: erbium-doped fiber amplifier; DGD: differential group delay; Pol.: polarizer; BPF: band-pass filter; ODL: tunable optical delay line; PM: phase modulator; OC: optical coupler.

the symbol-wise hexadecimal coding/decoding using a CW pump, the power of CW pump is  $\sim 12.8$  dBm. The conversion efficiency is assessed to be about  $-15.4$  dB for the symbol-wise hexadecimal coding while  $-14.9$  dB for the symbol-wise hexadecimal decoding. For the symbol-wise hexadecimal coding/decoding using a  $(0, \pi/4)$  phase-modulated pump, the power of the  $(0, \pi/4)$  phase-modulated pump is  $\sim 9.8$  dBm. The symbol-wise hexadecimal coding has a conversion efficiency of about  $-20.9$  dB, while the symbol-wise hexadecimal decoding shows a conversion efficiency of around  $-19.1$  dB.

Figure 47 depicts observed constellation diagrams and in-phase (I) and quadrature (Q) components for optical variable symbol-wise hexadecimal coding/decoding. Figure 47(a) shows the 10-Gbaud 16-QAM signal corresponding to the back-to-back (B-B) case. The EVM is measured to be 5.5%rms. The 16 constellation points can be clearly seen in the complex I/Q plane. Note that hexadecimal numbers can be represented by these 16 constellation points. For the symbol-wise hexadecimal coding/decoding using a CW pump, the phase-conjugated degenerate FWM process determines the coding and decoding algorithms to be  $(\Phi_{Ci} = -\Phi_{Pi})$  and  $(-(-\Phi_{Pi}) = \Phi_{Pi})$ , respectively. The constellations in the complex I/Q plane are manipulated following the coding and decoding algorithms. Figure 47(b) and (c) show the constellation diagrams of coded signal with an EVM of 6.3%rms and decoded signal with an EVM of 6.4%rms, respectively. For the symbol-wise hexadecimal coding/decoding using a phase-modulated pump, a  $(0, \pi/4)$  pump phase modulation with an EVM of 5.0%rms is employed in the experiment, as shown in Fig. 47(d). The constellation diagrams of the coded signal with an EVM of 7.8%rms and decoded signal with an EVM of 6.4%rms are shown in Fig. 47(e) and (f). The constellation manipulation in the complex I/Q plane follows the coding algorithm  $(\Phi_{Ci} = 2\Phi_{Ki} - \Phi_{Pi})$  for the symbol-wise hexadecimal coding process and decoding algorithm  $(2\Phi_{Ki} - \Phi_{Ci} = 2\Phi_{Ki} - (2\Phi_{Ki} - \Phi_{Pi}) = \Phi_{Pi})$  for the symbol-wise hexadecimal decoding process. Remarkably, for phase-modulated pump-assisted symbol-wise hexadecimal coding/decoding, the pump phase modulation and phase conjugation of degenerate FWM contribute together to the coding and decoding algorithms.



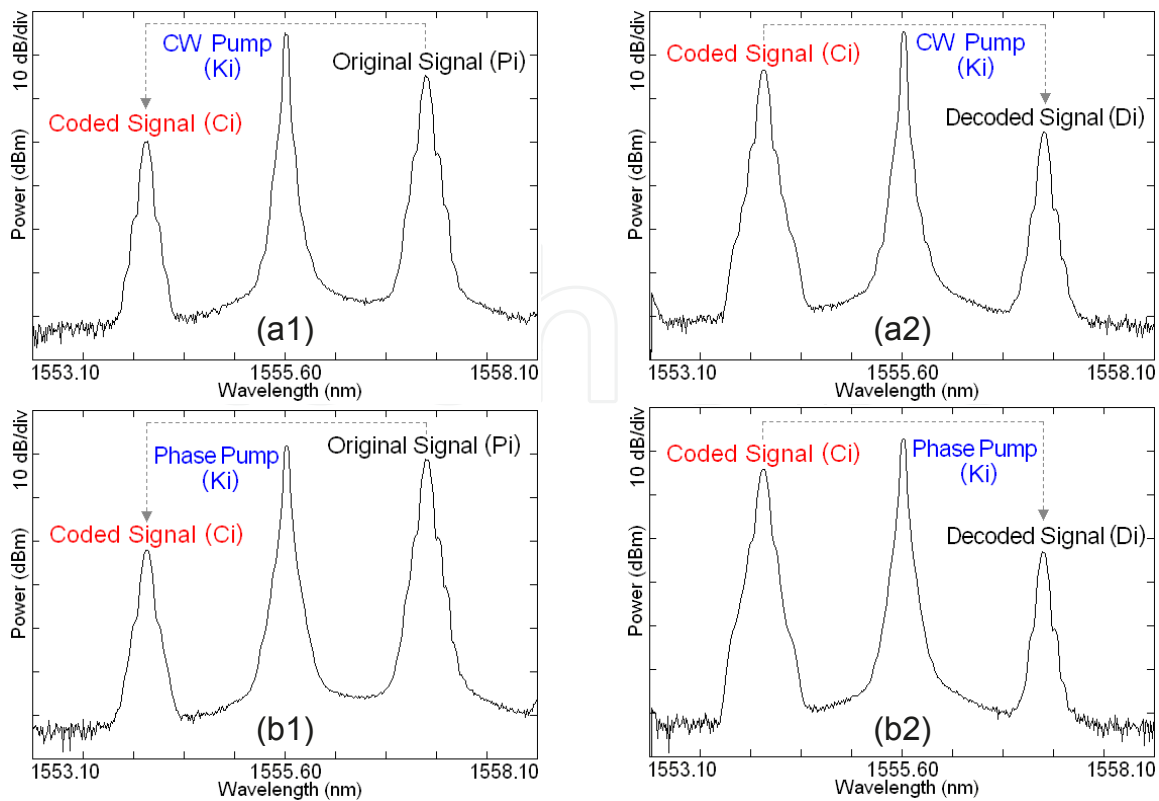


**Figure 46.** Measured spectra for high-base coding/decoding. Degenerate FWM in HNLF, 16-QAM signal and CW/phase-modulated pumps are employed to enable symbol-wise hexadecimal coding/decoding. (a1)(a2) Symbol-wise hexadecimal coding/decoding using a CW pump; (b1)(b2) symbol-wise hexadecimal coding/decoding using a  $(0, \pi/4)$  phase-modulated pump; (a1)(b1) symbol-wise hexadecimal coding; (a2)(b2) symbol-wise hexadecimal decoding.

To confirm the implementation of optical variable symbol-wise hexadecimal coding/decoding, the complex amplitudes (i.e., in-phase and quadrature components) of symbol sequence for different signals are recorded in the experiment. As shown in Fig. 48, for symbol-wise hexadecimal coding/decoding using a CW pump, by comparing the symbol sequence of coded signal and original signal, one can clearly see that all the constellation points in the complex I/Q plane are mapped to their symmetrical positions with respect to the I-axis. This constellation manipulation is determined by the coding algorithm of CW pump-assisted hexadecimal coding. Additionally, by comparing the symbol sequence of decoded signal and original signal one can confirm that the decoded signal recovers the original signal.

As shown in Fig. 49, for symbol-wise hexadecimal coding/decoding using a  $(0, \pi/4)$  phase-modulated pump, the corresponding coding algorithm manipulates the constellation points in the complex I/Q plane as follows. All the constellation points in the complex I/Q plane are first flipped to their symmetrical points with respect to the I-axis. Then, a counter-clockwise rotation of  $\pi/2$  is introduced to the constellation points, which meet the pump phase modulation of  $\pi/4$ . One can expect enhanced security for the symbol-wise hexadecimal coding using a phase-modulated pump owing to the added coding algorithm contribution from the pump. When compared to the symbol-wise hexadecimal coding using a CW pump, the phase-modulated pump-assisted symbol-wise hexadecimal coding is not so straightforward.

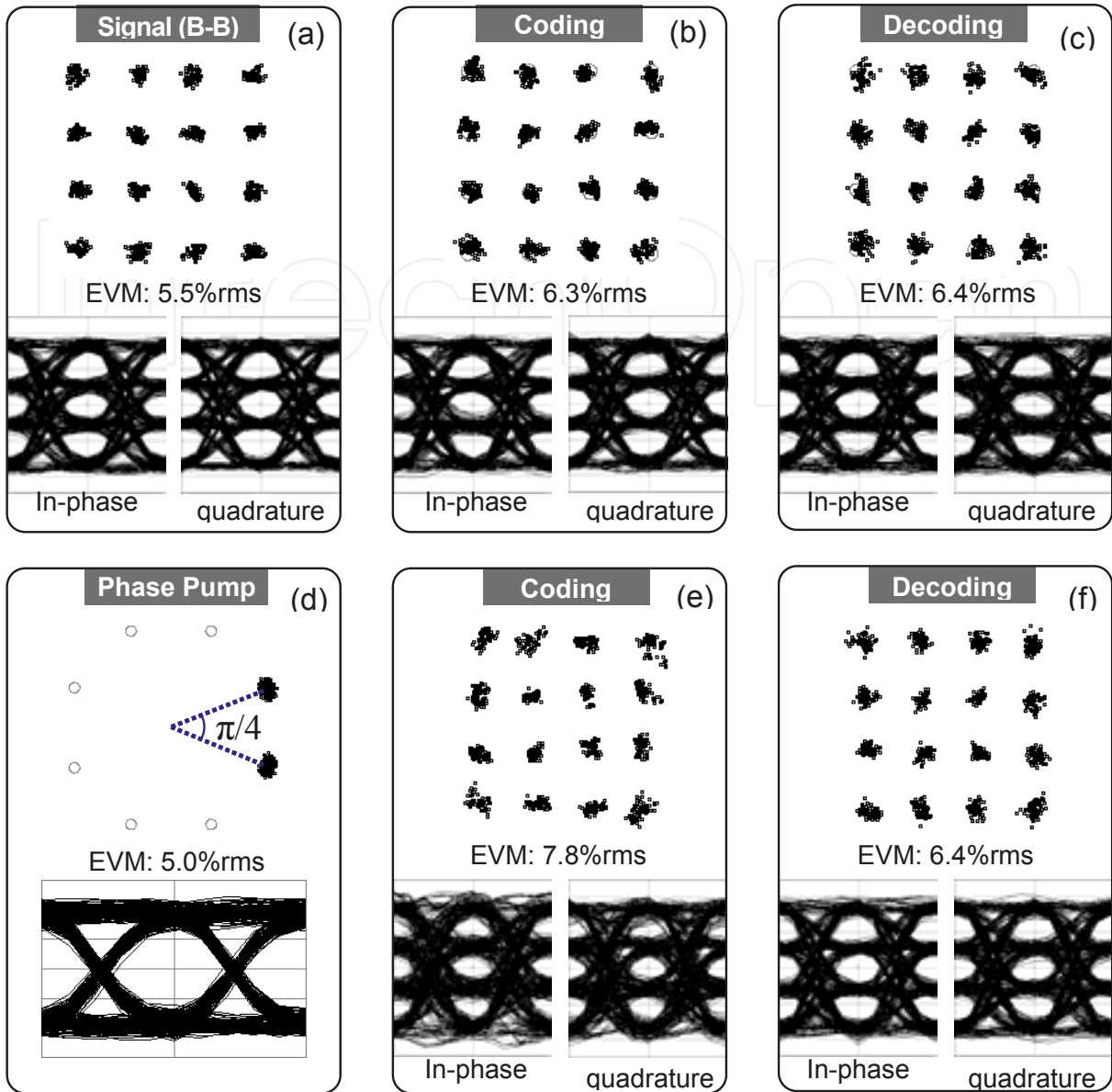


**Figure 47.** Measured constellation diagrams and in-phase (I) and quadrature (Q) components for high-base coding/decoding. Degenerate FWM in HNLF, 16-QAM signal, and CW/phase-modulated pumps are employed to enable symbol-wise hexadecimal coding/decoding. (a) Back-to-back (B-B) 16-QAM signal; (b) coded signal using a CW pump; (c) decoded signal using CW pump; (d)  $(0, \pi/4)$  phase-modulated pump; (e) coded signal using a  $(0, \pi/4)$  phase-modulated pump; (f) decoded signal using a  $(0, \pi/4)$  phase-modulated pump.

Nevertheless, the hexadecimal coding process is still verified from Fig. 49, i.e., the symbol sequence relationship of coded signal and original signal follows the coding algorithm of  $(0, \pi/4)$  phase-modulated pump-assisted symbol-wise hexadecimal coding. In addition, for the symbol-wise hexadecimal decoding process, the decoded signal recovers the information carried by the original signal. From the obtained results as shown in Figs. 48 and 49, one can clearly confirm the successful realization of 10-Gbaud optical variable symbol-wise hexadecimal coding/decoding by exploiting degenerate FWM in HNLF, 16-QAM signal, and CW/phase-modulated pumps.

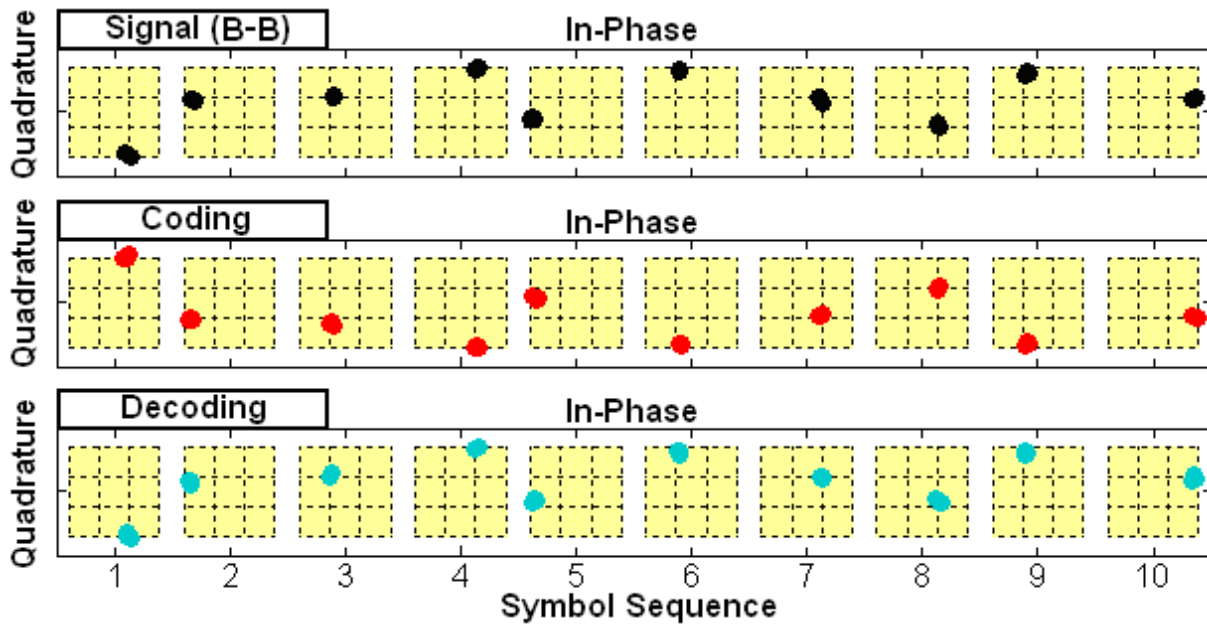


**Figure 48.** Measured complex amplitudes (i.e., in-phase and quadrature components) of symbol sequence for optical symbol-wise hexadecimal coding/decoding using a CW pump.

The BER performance is characterized for CW/phase-modulated pump-assisted optical variable symbol-wise hexadecimal coding/decoding. Shown in Fig. 50(a) are measured BER curves for the symbol-wise hexadecimal coding/decoding using a CW pump. OSNR penalty is used for performance evaluation defined by the ratio of the received OSNR of the coded signal to that of the back-to-back (B-B) signal. The measured OSNR penalty at a BER of  $2e-3$  is  $\sim 0.6$  dB for CW pump-assisted symbol-wise hexadecimal coding. The measured OSNR penalty at a BER of  $2e-3$  for CW pump-assisted symbol-wise hexadecimal decoding, i.e., the ratio of the received OSNR of the decoded signal to that of the B-B signal, is around 1.1 dB. Shown in Fig. 50(b) are measured BER curves for the symbol-wise hexadecimal coding/decoding using a  $(0, \pi/4)$  phase-modulated pump. From Fig. 50(b) one can see that the OSNR penalty at a BER of  $2e-3$  is measured to be  $\sim 1.2$  dB for symbol-wise hexadecimal coding process and  $\sim 0.9$  dB for symbol-wise hexadecimal decoding process, respectively.

We study the BER performance of symbol-wise hexadecimal coding/decoding as a function of the pump phase modulation depth. Figure 51(a) and (b) show measured results for symbol-wise hexadecimal coding and decoding, respectively. The OSNR is fixed around 20 dB. For the symbol-wise hexadecimal coding process as shown in Fig. 51(a), the coding operation performance is sensitive to the pump phase modulation depth. In contrast, for the symbol-wise hexadecimal decoding process as shown in Fig. 51(b), the decoding operation performance changes slightly. Such interesting phenomenon can be briefly explained as follows. For the symbol-wise hexadecimal coding process with the coding algorithm of  $\Phi_{Ci} = 2\Phi_{Ki} - \Phi_{Pi}$ , twice phase modulation of the pump is added to the coded signal. As a result, any change of the pump phase modulation depth and resultant offset from  $\pi/4$  pump phase modulation can cause the deviation of the constellation points of 16-QAM from their standard positions. Thus, the coding performance is degraded for symbol-wise hexadecimal coding process. To maintain



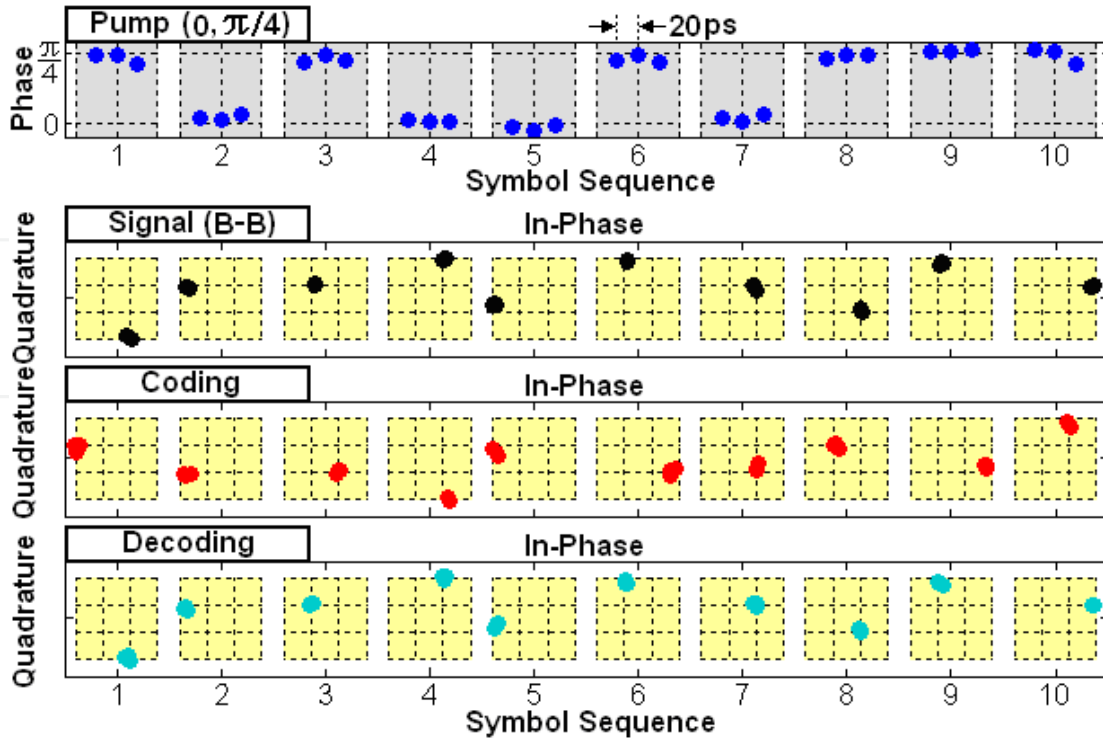


**Figure 49.** Measured complex amplitudes of symbol sequence for optical symbol-wise hexadecimal coding/decoding using a phase-modulated pump. A binary phase modulation of  $(0, \pi/4)$  is applied to the pump.

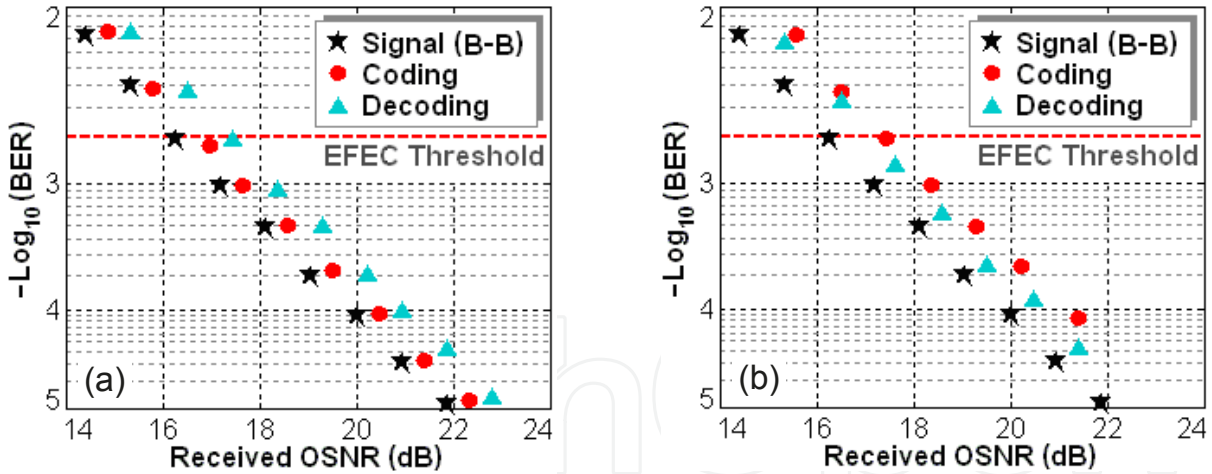
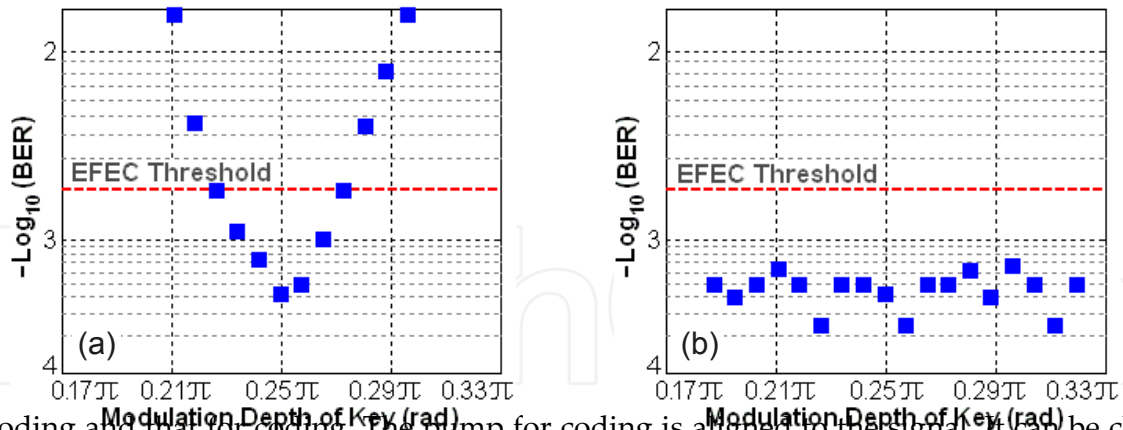


**Figure 50.** Measured BER curves for optical variable symbol-wise hexadecimal coding/decoding. (a) CW pump; (b)  $(0, \pi/4)$  phase-modulated pump.

the BER below  $2e-3$  (EFEC threshold), the tolerance of the pump phase modulation offset is assessed to be about  $0.023\pi$ , as shown in Fig. 51(a). For the symbol-wise hexadecimal decoding process with the decoding algorithm of  $2\Phi_{Ki} - \Phi_{Ci} = 2\Phi_{Ki} - (2\Phi_{Ki} - \Phi_{Pi}) = \Phi_{Pi}$  algorithms, it is easy to understand that the BER performance of the decoded signal is independent on the pump phase modulation, i.e., insensitive to the modulation depth of the pump as shown in Fig. 51(b).



decoding and that for coding. The pump for coding is aligned to the signal. It can be clearly seen that the performance of decoding process is dependent on the offset in the time domain between the pump for decoding and that for coding. To maintain the BER below  $2e-3$  (EFEC threshold), the tolerance of the relative pump offset to the symbol period is assessed to be about 20%.

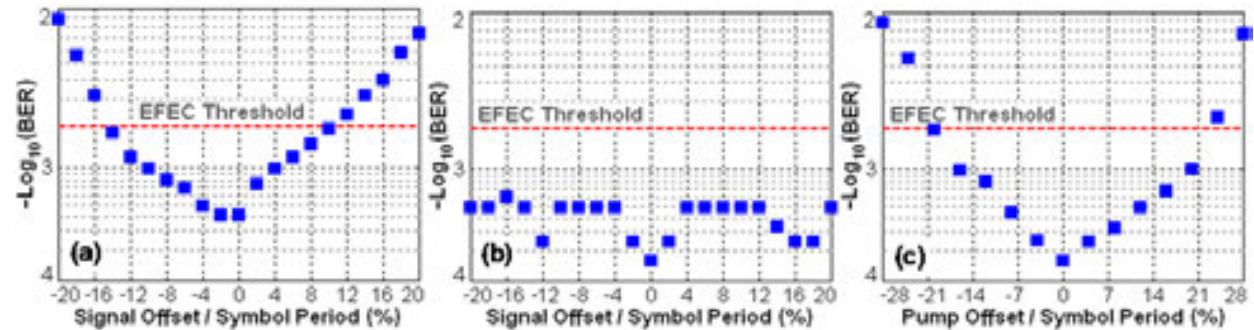


Fig. 52. Measured BER performance of symbol-wise hexadecimal coding/decoding versus signal/pump offset in the time domain. (a) Measured BER of coding as a function of the offset in the time domain between the signal and the pump for coding; (b) Measured BER of decoding as a function of the offset in the time domain between the signal and the pump for decoding; (c) Measured BER of decoding as a function of the offset in the time domain between the pump for coding and the pump for decoding. The pump for decoding is aligned to the pump for coding; (c) Measured BER of decoding as a function of the offset in the time domain between the pump for decoding and the pump for coding. The pump for coding is aligned to the signal.

We further evaluate the BER performance of symbol-wise hexadecimal coding/decoding versus the signal offset and pump offset in the time domain, as shown in Fig. 52. In the experiment, the OSNR is fixed around 20 dB. Figure 52(a) depicts the measured BER of symbol-wise hexadecimal coding as a function of the offset in the time domain between the signal and the pump for coding. Note that the pump for decoding is not involved. It is shown that the coding is sensitive to the signal offset from the pump. This is predictable according to the coding algorithm of  $C_i = 2\pi K_i \cdot \phi_i$ . To keep the BER below  $2e-3$  (EFEC threshold), the tolerance of the relative signal offset to the symbol period is measured to be about 10%. Figure 52(b) plots the measured BER of symbol-wise hexadecimal decoding as a function of the offset in the time domain between the signal and the pump for decoding. The pump for decoding is aligned to the pump for coding. One can clearly see that the BER performance is insensitive to the signal offset in the time domain. This is easy to understand based on the decoding algorithm of  $2\phi_i = \phi_{\text{sig}} - \phi_{\text{pump}} = (2\phi_{\text{sig}} - \phi_{\text{pump}}) = \phi_{\text{pi}}$ . Figure 52(c) shows measured BER of symbol-wise hexadecimal decoding as a function of the offset in the time domain between the pump for coding and the pump for decoding. The pump for decoding is aligned to the pump for coding. It is shown that the BER performance is insensitive to the pump offset in the time domain. This is predictable according to the decoding algorithm of  $2\phi_i = \phi_{\text{sig}} - \phi_{\text{pump}} = (2\phi_{\text{sig}} - \phi_{\text{pump}}) = \phi_{\text{pi}}$ .

## 6 Conclusion

In this chapter, we have reviewed recent research efforts toward high-base optical signal processing by adopting multilevel modulation signals and exploiting optical nonlinearities. 1) High-Base Wavelength Conversion. On-chip, high-base, all-optical wavelength conversion of multicarrier, multilevel modulation signals has been demonstrated using degenerate FWM in a silicon waveguide and OFDM m-QAM signals. Impressive operation performance of on-chip 3.2 Gbaud/s OFDM 16/32/64/128-QAM wavelength conversion has been achieved in the experiment.

2) High-Base Optical Data Exchange: Phase-transparent, high-base optical data exchange between two 100-Gbit/s DQPSK signals has been demonstrated using the parametric depletion effect of nondegenerate FWM in an HNLF. Simultaneous multichannel data exchange has been proposed and demonstrated using bidirectional degenerate FWM in a single HNLF. Moreover, a reconfigurable Tbit/s network switching element using double-pass LCoS technology accompanied by bidirectional degenerate FWM in a single HNLF has been proposed. 3) High-Base Optical Signal Processing: High-base optical signal processing has been demonstrated using the parametric depletion effect of nondegenerate FWM in an HNLF. Simultaneous multichannel data exchange has been proposed and demonstrated using bidirectional degenerate FWM in a single HNLF. Moreover, a reconfigurable Tbit/s network switching element using double-pass LCoS technology accompanied by bidirectional degenerate FWM in a single HNLF has been proposed.

hexadecimal decoding as a function of the offset in the time domain between the pump for decoding and that for coding. The pump for coding is aligned to the signal. It can be clearly seen that the performance of decoding process is dependent on the offset in the time domain between the pump for decoding and that for coding. To maintain the BER below  $2e-3$  (EFEC threshold), the tolerance of the relative pump offset to the symbol period is assessed to be about 20%.

## 6. Conclusion

In this chapter, we have reviewed recent research efforts toward high-base optical signal processing by adopting multilevel modulation signals and exploiting optical nonlinearities.

1. **High-Base Wavelength Conversion:** On-chip, high-base, all-optical wavelength conversion of multicarrier, multilevel modulation signals has been demonstrated using degenerate FWM in a silicon waveguide and OFDM m-QAM signals. Impressive operation performance of on-chip 3.2 Gbaud/s OFDM 16/32/64/128-QAM wavelength conversion has been achieved in the experiment.
2. **High-Base Optical Data Exchange:** Phase-transparent, high-base optical data exchange between two 100-Gbit/s DQPSK signals has been demonstrated using the parametric depletion effect of nondegenerate FWM in an HNLF. Simultaneous multichannel data exchange has been proposed and demonstrated using bidirectional degenerate FWM in a single HNLF. Moreover, a reconfigurable Tbit/s network switching element using double-pass LCoS technology accompanied by bidirectional degenerate FWM in a single HNLF has been proposed. 2.3-Tbit/s multifunctional grooming switch has been demonstrated in the experiment, performing simultaneous selective high-base add/drop, high-base switchable data exchange, and high-base power equalization, for ITU-grid-compatible 23-channel 100-Gbit/s RZ-DQPSK signals. Additionally, ultrahigh-speed high-base optical data exchange of 640 Gbaud (2.56 Tbit/s) 16-QAM and 640 Gbaud (3.84 Tbit/s) 64-QAM signals has been proposed and simulated by exploiting non-degenerate FWM in a silicon-organic hybrid slot waveguide.
3. **High-Base Optical Computing:** By adopting 100-Gbit/s two-input RZ-DQPSK signals (A, B) and exploiting three degenerate FWM processes and three nondegenerate FWM processes in an HNLF, simultaneous 50-Gbaud two-input quaternary addition ( $A+B$ ), dual-directional subtraction ( $A-B$ ,  $B-A$ ), complement ( $-A$ ,  $-B$ ), and doubling ( $2B$ ) have been demonstrated in the experiment. By employing 100-Gbit/s three-input RZ-DQPSK signals (A, B, C/-C) and three nondegenerate FWM processes in an HNLF, 50-Gbaud three-input quaternary hybrid addition and subtraction ( $A+B-C$ ,  $A+C-B$ ,  $B+C-A$ ,  $A+B+C$ ) have been demonstrated in the experiment. Furthermore, three-input (A, B, C) 40-Gbaud (160-Gbit/s) optical hexadecimal addition/subtraction ( $A+B-C$ ,  $A+C-B$ ,  $B+C-A$ ,  $A+B+C$ ,  $A-B-C$ ,  $B-A-C$ ) has also been proposed and simulated based on nondegenerate FWM in a silicon-organic hybrid slot waveguide.
4. **High-Base Optical Coding/Decoding:** By exploiting degenerate FWM in an HNLF and adopting 16-QAM signal, 10-Gbaud optical variable symbol-wise hexadecimal coding/



decoding assisted by a CW pump or a phase-modulated pump has been demonstrated in the experiment. The former takes the coding through the phase conjugation of degenerate FWM, and the latter offers enhanced coding via the combined contributions from the phase modulation of the pump and the phase-conjugated FWM.

Beyond high-base wavelength conversion, data exchange, optical computing, and optical coding/decoding based on degenerate/nondegenerate FWM in HNLFs or silicon waveguides, with future improvements, other different optical nonlinearities on various nonlinear optical device platforms would also be employed to flexibly manipulate the amplitude and phase information of advanced multilevel modulation signals, which might open diverse interesting applications in robust high-base optical signal processing.

## Acknowledgements

This work was supported by the National Natural Science Foundation of China (NSFC) under grants 61222502, 11574001, 11274131, and 61077051; the Program for New Century Excellent Talents in University (NCET-11-0182); the National Basic Research Program of China (973 Program) under grant 2014CB340004; the Wuhan Science and Technology Plan Project under grant 2014070404010201; the Fundamental Research Funds for the Central Universities (HUST) under grants 2012YQ008 and 2013ZZGH003. The authors thank the Center of Micro-Fabrication and Characterization (CMFC) of WNLO for the support in the manufacturing process of silicon waveguides. The authors also thank the facility support of the Center for Nanoscale Characterization and Devices of WNLO.

## Author details

Jian Wang<sup>1\*</sup> and Alan E. Willner<sup>2</sup>

\*Address all correspondence to: [jwang@hust.edu.cn](mailto:jwang@hust.edu.cn)

1 Wuhan National Laboratory for Optoelectronics, School of Optical and Electronic Information, Huazhong University of Science and Technology, Wuhan, Hubei, China

2 Department of Electrical Engineering, University of Southern California, Los Angeles, California, USA

## References

- [1] P. Kaminow, T. Li, and A. E. Willner, *Optical Fiber Telecommunications VIB Systems and Networks*, Sixth Edition (Elsevier, 2013).

- [2] P. P. Mitra and J. B. Stark, "Nonlinear limits to the information capacity of optical fibre communications," *Nature* 411, 1027–1030 (2001).
- [3] R. Essiambre, G. Kramer, P. J. Winzer, G. J. Foschini, and B. Goebel, "Capacity limits of optical fiber networks," *J. Lightwave Technol.* 28, 662–701 (2010).
- [4] D. J. Richardson, J. M. Fini, and L. E. Nelson, "Space-division multiplexing in optical fibres," *Nature Photon.* 7, 354–362 (2013).
- [5] P. J. Winzer, "Making spatial multiplexing a reality," *Nature Photon.* 8, 345–348 (2014).
- [6] M. Saruwatari, "All-optical signal processing for terabit/second optical transmission," *IEEE J. Sel. Top. Quantum Electron.* 6, 1363–1374 (2000).
- [7] A. E. Willner, S. Khaleghi, M. R. Chitgarha, and O. F. Yilmaz, "All-optical signal processing," *J. Lightwave Technol.* 32, 660–680 (2014).
- [8] D. Cotter, R. J. Manning, K. J. Blow, A. D. Ellis, A. E. Kelly, D. Nesses, I. D. Phillips, A. J. Poustie, and D. C. Rogers, "Nonlinear optics for high-speed digital information processing," *Science* 286, 1523–1528 (1999).
- [9] S. Watanabe and F. Futami, "All-optical signal processing using highly nonlinear optical fibers," *IEICE Trans. Electron.* E84-B, 1179–1189 (2001).
- [10] S. Radic and C. J. McKinstrie, "Optical amplification and signal processing in highly nonlinear optical fiber," *IEICE Trans. Electron.* E88-C, 859–869 (2005).
- [11] M. D. Pelusi, V. G. Ta'eed, L. B. Fu, E. Mägi, M. R. E. Lamont, S. Madden, D.-Y. Choi, D. A. P. Bulla, B. Luther-Davies, and B. J. Eggleton, "Applications of highly-nonlinear chalcogenide glass devices tailored for high-speed all-optical signal processing," *IEEE J. Sel. Top. Quantum Electron.* 14, 529–539 (2008).
- [12] M. D. Pelusi, F. Luan, E. Magi, M. R. E. Lamont, D. J. Moss, B. J. Eggleton, J. S. Sanghera, L. B. Shaw, and I. D. Aggarwal, "High bit rate all-optical signal processing in fiber photonic wire," *Opt. Express.* 16, 11506–11512 (2008).
- [13] C. Langrock, S. Kumar, J. E. McGeehan, A. E. Willner, and M. M. Fejer, "All-optical signal processing using  $\chi^{(2)}$  nonlinearities in guided-wave devices," *J. Lightwave Technol.* 24, 2579–2592 (2006).
- [14] R. Salem, M. A. Foster, A. C. Turner, D. F. Geraghty, M. Lipson, and A. L. Gaeta, "Signal regeneration using low-power four-wave mixing on silicon chip," *Nature Photon.* 2, 35–38 (2008).
- [15] C. Koos, P. Vorreau, T. Vallaitis, P. Dumon, W. Bogaerts, R. Baets, B. Esembeson, I. Biaggio, T. Michinobu, F. Diederich, W. Freude, and J. Leuthold, "All-optical high-speed signal processing with silicon-organic hybrid slot waveguides," *Nature Photon.* 3, 216–219 (2009).

- [16] K. Nozaki, T. Tanabe, A. Shinya, S. Matsuo, T. Sato, H. Taniyama, and M. Notomi, "Sub-femtojoule all-optical switching using a photonic-crystal nanocavity," *Nature Photon.* 4, 477–483 (2010).
- [17] J. Leuthold, C. Koos, and W. Freude, "Nonlinear silicon photonics," *Nature Photon.* 4, 535–544 (2010).
- [18] A. E. Willner, O. F. Yilmaz, J. Wang, X. X. Wu, A. Bogoni, L. Zhang, and S. R. Nuccio, "Optically efficient nonlinear signal processing," *IEEE J. Sel. Top. Quantum Electron.* 17, 320–332 (2011).
- [19] L. K. Oxenløwe, H. Ji, M. Galili, M. Pu, H. Hu, H. C. H. Mulvad, K. Yvind, J. M. Hvam, A. T. Clausen, and P. Jeppesen, "Silicon photonics for signal processing of Tbit/s serial data signals," *IEEE J. Sel. Top. Quantum Electron.* 18, 996–1005 (2011).
- [20] B. J. Eggleton, T. D. Vo, R. Pant, J. Schr, M. D. Pelusi, D. Yong Choi, S. J. Madden, and B. Luther-Davies, "Photonic chip based ultrafast optical processing based on high nonlinearity dispersion engineered chalcogenide waveguides," *Laser Photon. Rev.* 6, 97–114 (2012).
- [21] S. J. B. Yoo, "Wavelength conversion technologies for WDM network applications," *J. Lightwave Technol.* 14, 955–966 (1999).
- [22] H. Hu, H. Ji, M. Galili, M. Pu, C. Peucheret, H. C. H. Mulvad, K. Yvind, J. M. Hvam, P. Jeppesen, and L. K. Oxenløwe, "Ultra-high-speed wavelength conversion in a silicon photonic chip," *Opt. Express.* 19, 19886–19894 (2011).
- [23] C.-S. Bres, N. Alic, E. Myslivets, and S. Radic, "Scalable multicasting in one-pump parametric amplifier," *J. Lightwave Technol.* 27, 356–363 (2009).
- [24] X. Wu, A. Bogoni, O. F. Yilmaz, S. R. Nuccio, J. Wang, and A. E. Willner, "8-fold 40–320 Gbit/s phase-coherent multiplexing and 320–40 Gbit/s demultiplexing using highly nonlinear fibers," *Opt. Lett.* 35, 1896–1898 (2010).
- [25] A. Biberman, B. G. Lee, A. C. Turner-Foster, M. A. Foster, M. Lipson, A. L. Gaeta, and K. Bergman, "Wavelength multicasting in silicon photonic nanowires," *Opt. Express* 18, 18047–18055 (2010).
- [26] O. F. Yilmaz, J. Wang, S. Khaleghi, X. Wang, S. R. Nuccio, X. Wu, and A. E. Willner, "Preconversion phase modulation of input differential phase-shift-keying signals for wavelength conversion and multicasting applications using phase-modulated pumps," *Opt. Lett.* 36, 731–733 (2011).
- [27] K. Uesaka, K. K.-Y. Wong, M. E. Marhic, and L. G. Kazovsky, "Wavelength exchange in a highly nonlinear dispersion-shifted fiber: Theory and experiments," *IEEE J. Sel. Top. Quantum Electron.* 8, 560–568 (2002).



- [28] R. W. L. Fung, Henry K. Y. Cheung, and K. K. Y. Wong, "Widely tunable wavelength exchange in anomalous-dispersion regime," *IEEE Photon. Technol. Lett.* 19, 1846–1848 (2007).
- [29] J. Wang and Q. Sun, "Theoretical analysis of power swapping in quadratic nonlinear medium," *Appl. Phys. Lett.* 96, 081108 (2010).
- [30] J. Wang, S. R. Nuccio, X. Wu, O. F. Yilmaz, L. Zhang, I. Fazal, J. Y. Yang, Y. Yue, and A. E. Willner, "40 Gbit/s optical data exchange between wavelength-division-multiplexed channels using a periodically poled lithium niobate waveguide," *Opt. Lett.* 35, 1067–1069 (2010).
- [31] J. Wang, Z. Bakhtiari, S. R. Nuccio, O. F. Yilmaz, X. Wu, and A. E. Willner, "Phase-transparent optical data exchange of 40 Gbit/s differential phase-shift keying signals," *Opt. Lett.* 35, 2979–2981 (2010).
- [32] C. Schubert, C. Schmidt, S. Ferber, R. Ludwig, and H. G. Weber, "Error free all-optical add-drop multiplexing at 160 Gbit/s," *Electron. Lett.* 39, 1074–1076 (2003).
- [33] H. Ji, M. Pu, H. Hu, M. Galili, L. Oxenløwe, K. Yvind, J. M. Hvam, and P. Jeppesen, "Optical waveform sampling and error-free demultiplexing of 1.28 Tb/s serial data in a nanoengineered silicon waveguide," *J. Lightwave Technol.* 29, 426–431 (2011).
- [34] A. Bogoni, X. Wu, S. R. Nuccio, J. Wang, Z. Bakhtiari, and A. E. Willner, "Photonic 640-Gb/s reconfigurable OTDM add-drop multiplexer based on pump depletion in a single PPLN waveguide," *IEEE J. Sel. Top. Quantum Electron.* 18, 709–716 (2012).
- [35] J. Wang, H. Fu, D. Geng, and A. E. Willner, "Single-PPLN-assisted wavelength-time-selective switching dropping swapping for 100-GHz-spaced WDM signals," *Opt. Express.* 21, 3756–3774 (2013).
- [36] J. Wang, J. Q. Sun, and Q. Z. Sun, "Single-PPLN-based simultaneous half-adder, half-subtractor, and OR logic gate: proposal and simulation," *Opt. Express.* 15, 1690–1699 (2007).
- [37] J. Wang, J. Q. Sun, X. L. Zhang, D. X. Huang, and M. M. Fejer, "Ultrafast all-optical three-input boolean XOR operation for differential phase-shift keying signals using periodically poled lithium niobate," *Opt. Lett.* 33, 1419–1421 (2008).
- [38] A. Bogoni, X. Wu, I. Fazal, and A. E. Willner, "160 Gb/s time domain channel extraction/insertion and all-optical logic operations exploiting a single PPLN waveguide," *J. Lightwave Technol.* 27, 4221–4227 (2009).
- [39] A. Bogoni, X. Wu, I. Fazal, and A. E. Willner, "320 Gbit/s photonic processing based on sum/difference frequency generation and pump depletion in a single PPLN waveguide," *Opt. Lett.* 34, 1825–1827 (2009).
- [40] A. Bogoni, X. Wu, Z. Bakhtiari, S. Nuccio, and A. E. Willner, "640 Gbit/s photonic logic gates," *Opt. Lett.* 35, 3955–3957 (2010).

- [41] J. Wang, J. Sun, Q. Sun, D. Wang, M. Zhou, X. Zhang, D. Huang, M. M. Fejer, "All-optical format conversion using a periodically poled lithium niobate waveguide and a reflective semiconductor optical amplifier," *Appl. Phys. Lett.* 91, 051107 (2007).
- [42] J. Wang, J. Sun, X. Zhang, D. Huang, and M. M. Fejer, "All-optical format conversions using periodically poled lithium niobate waveguides," *IEEE J. Quantum Electron.* 45, 195–205 (2009).
- [43] J. Wang, J. Sun, X. Zhang, D. Huang, and M. M. Fejer, "Optical phase erasure and its application to format conversion through cascaded second-order processes in periodically poled lithium niobate," *Opt. Lett.* 33, 1804–1806 (2008).
- [44] J. Wang, Q. Z. Sun, and J. Q. Sun, "All-optical 40 Gbit/s CSRZ-DPSK logic XOR gate and format conversion using four-wave mixing," *Opt. Express.* 17, 12555–12563 (2009).
- [45] M. S. Rasras, I. Kang, M. Dinu, J. Jaques, N. Dutta, A. Piccirilli, M. A. Cappuzzo, E. Y. Chen, L. T. Gomez, A. Wong-Foy, S. Cabot, G. S. Johnson, L. Buhl, and S. S. Patel, "A programmable 8-bit optical correlator filter for optical bit pattern recognition," *IEEE Photon. Technol. Lett.* 20, 694–696 (2008).
- [46] K. Croussore and G. Li, "Phase and amplitude regeneration of differential phase-shift keyed signals using phase-sensitive amplification," *IEEE J. Sel. Top. Quantum Electron.* 14, 648–658 (2008).
- [47] R. Slavík, F. Parmigiani, J. Kakande, C. Lundström, M. Sjödin, P. A. Andrekson, R. Weerasuriya, S. Sygletos, A. D. Ellis, L. Gruner-Nielsen, D. Jakobsen, S. Herstrøm, R. Phelan, J. O’Gorman, A. Bogris, D. Syvridis, S. Dasgupta, P. Petropoulos, and D. J. Richardson, "Alloptical phase and amplitude regenerator for next-generation telecommunications systems," *Nature Photon.* 4, 690–695 (2010).
- [48] Z. Tong, C. Lundström, P. A. Andrekson, C. J. McKinstrie, M. Karlsson, D. J. Blessing, E. Tipsuwannakul, B. J. Puttnam, H. Toda, and L. Gruner-Nielsen, "Towards ultrasensitive optical links enabled by low-noise phase-sensitive amplifiers," *Nature Photon.* 5, 430–436 (2011).
- [49] O. F. Yilmaz, S. R. Nuccio, X. Wu, and A. E. Willner, "40-Gb/s optical packet buffer using conversion/dispersion-based delays," *J. Lightwave Technol.* 28, 616–623 (2010).
- [50] S. R. Nuccio, O. F. Yilmaz, X. Wu, and A. E. Willner, "Fine tuning of conversion/dispersion based optical delays with a 1 pm tunable laser using cascaded acousto-optic mixing," *Opt. Lett.* 35, 523–525 (2010).
- [51] S. R. Nuccio, O. F. Yilmaz, X. Wang, H. Huang, J. Wang, X. Wu, and A. E. Willner, "Higher-order dispersion compensation to enable a 3.6  $\mu$ s wavelength-maintaining delay of a 100 Gb/s DQPSK signal," *Opt. Lett.* 35, 2985–2987 (2010).

- [52] Y. Dai, Y. Okawachi, A. C. Turner-Foster, M. Lipson, A. L. Gaeta, and C. Xu, "Ultra-long continuously tunable parametric delays via a cascading discrete stage," *Opt. Express*. 18, 333–339 (2010).
- [53] N. Alic, E. Myslivets, S. Moro, B. P.-P. Kuo, R. M. Jopson, C. J. McKinstrie, and S. Radic, "Microsecond parametric optical delays," *J. Lightwave Technol.* 28, 448–455 (2010).
- [54] P. J. Winzer and R. Essiambre, "Advanced optical modulation formats," *Proc. IEEE*. 94, 952–985 (2006).
- [55] P. J. Winzer and R. Essiambre, "Advanced modulation formats for high-capacity optical transport networks," *J. Lightwave Technol.* 24, 4711–4728 (2006).
- [56] P. J. Winzer, "Modulation and multiplexing in optical communication systems," *IEEE LEOS Newsletter*. 23, 4–10 (2009).
- [57] P. J. Winzer, "High-spectral-efficiency optical modulation formats," *J. Lightwave Technol.* 30, 3824–3835 (2012).
- [58] X. Zhou and J. Yu, "Multi-level, multi-dimensional coding for high-speed and high spectral-efficiency optical transmission," *J. Lightwave Technol.* 27, 3641–3653 (2009).
- [59] X. Zhou, "Digital signal processing for coherent multi-level modulation formats," *Chin. Opt. Lett.* 8, 863–870 (2010).
- [60] J. Yu and X. Zhou, "Multilevel modulations and digital coherent detection," *Opt. Fiber Technol.* 15, 197–208 (2009).
- [61] J. Yu and X. Zhou, "Ultra-high-capacity DWDM transmission system for 100 G and beyond," *IEEE Commun. Mag.* 48, S56–S64 (2010).
- [62] J. Yu, "Beyond 100G Ethernet," *IEEE Commun. Mag.* 48, 26–30 (2010).
- [63] S. J. Savory, "Digital coherent optical receivers: algorithms and subsystems," *IEEE J. Sel. Top. Quantum Electron.* 16, 1164–1179 (2010).
- [64] P. J. Winzer, G. Raybon, H. Song, A. Adamiecki, S. Corteselli, A. H. Gnauck, D. A. Fishman, C. R. Doerr, S. Chandrasekhar, L. L. Buhl, T. J. Xia, G. Wellbrock, W. Lee, B. Basch, T. Kawanishi, K. Higuma, and Y. Painchaud, "100-Gb/s DQPSK transmission: from laboratory experiments to field trials," *J. Lightwave Technol.* 26, 3388–3402 (2008).
- [65] X. Zhou, J. Yu, D. Qian, T. Wang, G. Zhang, and P. D. Magill, "High-spectral-efficiency 114-Gb/s transmission using polmux-RZ-8PSK modulation format and single-ended digital coherent detection technique," *J. Lightwave Technol.* 27, 146–152 (2009).
- [66] P. J. Winzer, A. H. Gnauck, C. R. Doerr, M. Magarini, and L. L. Buhl, "Spectrally efficient long-haul optical networking using 112-Gb/s polarization-multiplexed 16-QAM," *J. Lightwave Technol.* 28, 547–556 (2010).



- [67] A. H. Gnauck, P. J. Winzer, S. Chandrasekhar, X. Liu, B. Zhu, and D. W. Peckham, "Spectrally efficient long-haul WDM transmission using 224-Gb/s polarization-multiplexed 16-QAM," *J. Lightwave Technol.* 29, 373–377 (2011).
- [68] X. Liu, S. Chandrasekhar, X. Chen, P. J. Winzer, Y. Pan, T. F. Taunay, B. Zhu, M. Fish-teyn, M. F. Yan, J. M. Fini, E.M. Monberg, and F.V. Dimarcello, "1.12-Tb/s 32-QAM-OFDM superchannel with 8.6-b/s/Hz intrachannel spectral efficiency and space-division multiplexed transmission with 60-b/s/Hz aggregate spectral efficiency," *Opt. Express.* 19, B958–B964 (2011).
- [69] D. Qian, M.-F. Huang, E. Ip, Y.-K. Huang, Y. Shao, J. Hu, and T. Wang, "High capacity/spectral efficiency 101.7-Tb/s WDM transmission using PDM-128QAM-OFDM over 165-km SSMF within C- and L-bands," *J. Lightwave Technol.* 30, 1540–1548 (2012).
- [70] G.-W. Lu and T. Miyazaki, "Optical phase erasure based on FWM in HNLF enabling format conversion from 320-Gb/s RZ-DQPSK to 160-Gb/s RZ-DPSK," *Opt. Express.* 17(16), 13346–13353 (2009).
- [71] J. Wang, S. R. Nuccio, H. Huang, X. Wang, J.-Y. Yang, and A. E. Willner, "Optical data exchange of 100-Gbit/s DQPSK signals," *Opt. Express.* 18, 23740–23745 (2010).
- [72] G.-W. Lu, E. Tipsuwannakul, T. Miyazaki, C. Lundström, M. Karlsson, P. A. Andrek-son, "Format conversion of optical multilevel signals using FWM-based optical phase erasure," *J. Lightwave Technol.* 29(16), 2460–2466 (2011).
- [73] J. Wang, H. Huang, X. Wang, J.-Y. Yang, and A. E. Willner, "Multi-channel 100-Gbit/s DQPSK data exchange using bidirectional degenerate four-wave mixing," *Opt. Express.* 19, 3332–3338 (2011).
- [74] J. Wang, H. Huang, X. Wang, J.-Y. Yang, and A. E. Willner, "Reconfigurable 2.3-Tbit/s DQPSK simultaneous add/drop, data exchange and equalization using double-pass LCoS and bidirectional HNLF," *Opt. Express.* 19, 18246–18252 (2011).
- [75] J. Wang, J.-Y. Yang, X. Wu, O. F. Yilmaz, S. R. Nuccio, and A. E. Willner, "40-Gbaud/s (120-Gbit/s) octal and 10-Gbaud/s (40-Gbit/s) hexadecimal simultaneous addition and subtraction using 8PSK/16PSK and highly nonlinear fiber," in *Proc. Opt. Fiber Commun. Conf., Mar.* 2011, pp. 1–3.
- [76] E. Lazzeri, A. Malacarne, G. Serafino, and A. Bogoni, "Optical XOR for error detection and coding of QPSK I and Q components in PPLN waveguide," *IEEE Photon. Technol. Lett.* 24, 2258–2261 (2012).
- [77] J. Wang, S. R. Nuccio, J.-Y. Yang, X. X. Wu, A. Bogoni, and A. E. Willner, "High-speed addition/subtraction/complement/doubling of quaternary numbers using optical nonlinearities and DQPSK signals," *Opt. Lett.* 37, 1139–1141 (2012).
- [78] A. Malacarne, E. Lazzeri, V. Vercesi, M. Scaffardi, and A. Bogoni, "Colorless all-optical sum and subtraction of phases for phase-shift keying signals based on a periodically poled lithium niobate waveguide," *Opt. Lett.* 37, 3831–3833 (2012).

- [79] J. Wang, J.-Y. Yang, X. X. Wu, and A. E. Willner, "Optical hexadecimal coding/decoding using 16-QAM signal and FWM in HNLFs," *J. Lightwave Technol.* 30, 2890–2900 (2012).
- [80] J. Wang, J.-Y. Yang, H. Huang, and A. E. Willner, "Three-input optical addition and subtraction of quaternary base numbers," *Opt. Express.* 21, 488–499 (2013).
- [81] A. Bogris, "All-optical demultiplexing of 16-QAM signals into QPSK tributaries using four-level optical phase quantizers," *Opt. Lett.* 39, 1775–1778 (2014).
- [82] T. Umeki, O. Tadanaga, M. Asobe, Y. Miyamoto, and H. Takenouchi, "First demonstration of high-order QAM signal amplification in PPLN-based phase sensitive amplifier," *Opt. Express.* 22, 2473–2482 (2014).
- [83] C. Li, C. C. Gui, X. Xiao, Q. Yang, S. Yu, and J. Wang, "On-chip all-optical wavelength conversion of multicarrier, multilevel modulation (OFDM m-QAM) signals using a silicon waveguide," *Opt. Lett.* 39, 4583–4586 (2014).
- [84] R. Adams, M. Spasojevic, M. Chagnon, M. Malekiha, J. Li, D. V. Plant, and L. R. Chen, "Wavelength conversion of 28 GBaud 16-QAM signals based on four-wave mixing in a silicon nanowire," *Opt. Express.* 22, 4083–4090 (2014).
- [85] C. C. Gui and J. Wang, "Silicon-organic hybrid slot waveguide based three-input multicasted optical hexadecimal addition/subtraction," *Sci. Rep.* 4, 7491 (2014).
- [86] C. C. Gui and J. Wang, "Optical data exchange of m-QAM signals using a silicon-organic hybrid slot waveguide: proposal and simulation," *Opt. Express.* 22, 24796–24807 (2014).